

Syracuse University

SURFACE

Dissertations - ALL

SURFACE

December 2018

STRUCTURALLY SUPPORTED CELL-LADEN SCAFFOLDS FOR BONE TISSUE REGENERATION

Stephen William Sawyer
Syracuse University

Follow this and additional works at: <https://surface.syr.edu/etd>



Part of the [Engineering Commons](#)

Recommended Citation

Sawyer, Stephen William, "STRUCTURALLY SUPPORTED CELL-LADEN SCAFFOLDS FOR BONE TISSUE REGENERATION" (2018). *Dissertations - ALL*. 978.

<https://surface.syr.edu/etd/978>

This Dissertation is brought to you for free and open access by the SURFACE at SURFACE. It has been accepted for inclusion in Dissertations - ALL by an authorized administrator of SURFACE. For more information, please contact surface@syr.edu.

ABSTRACT

Due to challenges associated with current clinical techniques used to treat bone defects, there has been an increased focus on finding a tissue engineered solution. However, while great progress in this field has been achieved, researchers have yet to suitably combine the proper biological and structural environments needed to serve as a complete bone tissue substitute that is comparable to modern clinical solutions.

To achieve the goal of creating a model bone tissue substitute which could eventually serve as a viable therapy for bone trauma, be it caused by congenital medical conditions, age related diseases or high impact forces, three areas of the engineered construct architecture and composition were identified and studied in a successive fashion. First, a soft, biocompatible matrix within which cells could be encapsulated was studied, followed by an investigation on how to combine the soft matrix with a 3D printed structural frame. Finally, user-defined perfusable vasculature was added to the soft matrix in order to create a model bone tissue engineering construct capable of possible *in vivo* implantation.

In Chapter 2 of this work, osteoblast-like human osteosarcoma cells (Saos-2) were encapsulated within gelatin methacrylate (GelMA) hydrogels and the effect of the hydrogel density on cellular morphology and mineralization was investigated. It was found that the less dense hydrogels allowed for increased cell viability and spreading, while the denser gels appeared to encourage more mineral deposition on the construct periphery.

Building upon Chapter 2, Chapter 3 focused on the 3D printing of polycaprolactone (PCL) and composite PCL cages which could be combined with the soft GelMA matrices used for cellular encapsulation. It was found that while PCL and PCL composite cages could be reproducibly printed via a Makerbot 3D printer, the structural strengths did not surpass those of standard polylactic acid (PLA) thermoplastic cages. Furthermore, it was demonstrated that the cell-laden GelMA hydrogels containing encapsulated Soas-2 cells could be incorporated with the 3D printed structures for potential bone tissue engineering applications.

In Chapter 4, a simpler version of the cages produced in Chapter 3 were combined with sacrificial 3D printed polyvinyl alcohol (PVA) pipes and the dense cell-laden hydrogels investigated in Chapter 2 to create structurally supported, cell-laden hydrogel constructs. It was found that encapsulated cells could be stimulated to deposit mineral in the centers of the constructs via direct perfusion. However, in a larger version of the construct containing multiple pipes, mineralization was impeded due to diffusion issues caused by individual channel mineralization.

Finally, in Chapter 5 future strategies to improve upon the structurally supported cell-laden hydrogels are discussed which would solve the issues found in Chapter 4. Additionally, potential *in vivo* applications for this system are explored.

**STRUCTURALLY SUPPORTED CELL-LADEN
SCAFFOLDS FOR BONE TISSUE REGENERATION**

By

STEPHEN WILLIAM SAWYER

B.S., Virginia Military Institute, 2005

M.B.A., University of South Carolina, 2009

DISSERTATION

Submitted in partial fulfillment of the requirements for the degree of Doctor of Philosophy in
Bioengineering.

Syracuse University

December 2018

Copyright © Stephen William Sawyer 2018

All Rights Reserved

For G.T.S.

ACKNOWLEDGEMENTS

First and foremost, I would like to thank my advisor, Dr. Pranav Soman, for his support and guidance over the past 5 years. When I entered the Bioengineering PhD program at Syracuse University I had little research experience, and as a new faculty Dr. Soman took a great risk in selecting me to be his first student. I will always appreciate the patience and leadership demonstrated by Dr. Soman as he helped to mold me into a better researcher over the course of this program. I would also like to thank Dr. Soman for allowing me the opportunity to be involved in the publication of six different manuscripts over the course of my tenure in his lab.

I would next like to thank Dr. James Henderson and Dr. Cristina Marchetti for originally putting their faith in me by allowing me to enter the Syracuse Bioengineering PhD program with an IGERT fellowship. Like Dr. Soman, their ability to look past my lack of research experience and grant me the opportunity to succeed at Syracuse will never be forgotten. I would also like to extend an extra thank you to Dr. Henderson for agreeing to be a secondary advisor and mentor throughout this journey. His guidance and insight have been extremely important to me during this entire process.

I would next like to extend a special appreciation to both Dr. Megan Oest and Dr. Jason Horton. Not only did Dr. Oest and Dr. Horton allow me unfettered access to their labs at SUNY Upstate Medical University, but they provided key guidance and expertise which has allowed me to succeed over the course of my PhD career.

Next, I would like to thank Dr. Dacheng Ren for not only serving on my committee, but for also being one of the original professors who put their faith in me prior to acceptance to Syracuse University. Additionally, I would like to thank Dr. Teng Zhang who agreed on very short notice to serve as the chair of my defense committee. I am deeply thankful for his willingness to take time out of his schedule to serve as my committee chair.

I would also like to acknowledge all of the students, both past in present, in Dr. Soman's lab, Dr. Henderson's lab, Dr. Oest's lab, and Dr. Horton's lab. Be it through material synthesis, data analysis, or basic laboratory practices, the wonderful and skilled students who I have worked alongside all of these years will not be forgotten as I move forward with my career and I thank you all.

Throughout the course of this PhD, I was fortunate to be involved in the publication of six manuscripts, three of which serve as individual chapters in this work. Chapter 2, "Behavior of Encapsulated Saos-2 cells within Gelatin Methacrylate Hydrogels," was my first manuscript published and would not have been possible without the contributions of Dr. Bryan Margulies and Dr. Megan Oest. Dr. Margulies initially taught me cell culture and was instrumental in the initial stages of experimental development while Dr. Oest was pivotal in the writing and editing of the manuscript.

Chapter 3 of this work, "Developing 3D Scaffolds in the Field of Tissue Engineering to Treat Complex Bone Defects," was a collaboration between myself and Lucas D. Albrecht, an outstanding master's student in the Soman lab who I had the pleasure of working with. With the aid of Alex B. Filip, an undergraduate in the Soman lab, Lucas drove the hybrid spool development

and mechanical testing. Without the hard work from Lucas, the manuscript would not have been possible.

Chapter 4, “Perfusion Directed 3D Mineral Formation within Cell-Laden Hydrogels,” was the final paper published prior to my defense and served as the capstone to my work at Syracuse. As was the case with the other manuscripts, this paper was possible due to the combined effort of numerous students and professors. First and foremost, Shivkumar Shridhar, a previous student in Dr. Soman’s lab, was solely responsible for the COMSOL modeling and was a key reason for the article’s acceptance into Biofabrication. Kairui Zhang, a PhD student in the Soman lab, aided in the perfusion of constructs and made my work much more manageable towards the end of my studies. Furthermore, Lucas and Alex were critically important in the initial project design, printed all 3D constructs, and spearheaded the creation of the bioreactors in the Syracuse University machine shop. Finally, Dr. Horton was intimately involved in the writing of the manuscript and provided a much-needed perspective during the resubmission process.

I also wish to thank the SBI facility manager, Dr. Eric Finkelstein, and administrative staff, Karen Low, Lynore de la Rosa, and Jason Markle for their advice and help over the past few years. I appreciate their patience and willingness to always help.

Finally, I would like to thank my mother and father, who supported my decision to return to school and pursue a PhD. Without their support, this process would have never happened and for that, I am deeply grateful.

TABLE OF CONTENTS

List of Figuresxiii

Chapter 1: Introduction 1

1.1 The need for bone tissue engineering..... 1

 1.1.1 Creating a tissue engineered solution 4

1.2 The structure and composition of bone 4

 1.2.1 Cellular component 5

 1.2.2 Bone matrix 6

 1.2.3 Cortical and cancellous bone 7

 1.2.4 Hierarchy of the long bone 8

1.3 Bone vasculature and its role in bone growth and homeostasis 10

 1.3.1 New bone growth 11

 1.3.2 Bone remodeling 13

 1.3.3 Fracture repair 14

1.4 Challenges of developing a tissue engineered construct 15

 1.4.1 Challenge 1 – Soft matrix for cellular encapsulation 15

 1.4.2 Challenge 2 – Strategies for combining soft and hard components 17

 1.4.3 Challenge 3 – Adding perfusable vasculature 18

1.5 Scope of dissertation 20

1.6 References 20

Chapter 2: Behavior of Encapsulated Saos-2 Cells within Gelatin Methacrylate Hydrogels

..... 30

2.1 Abstract 30

2.2 Introduction 31

2.3 Materials and Methods	32
2.3.1 Gelatin methacrylate pre-polymer solution preparation.....	32
2.3.2 Saos-2 culture and encapsulation	33
2.3.3 Osteosarcoma mineralization	34
2.3.4 Histochemical analysis, Live/Dead staining, and image processing	34
2.3.5 Micro-computed tomography.....	35
2.3.6 Quantitative values and statistical analysis	36
2.4 Results.....	36
2.4.1 Formation of cell-laden hydrogels.....	36
2.4.2 Viability of encapsulated cells.....	38
2.4.3 Cellular morphology.....	41
2.4.4 Mineral deposition.....	43
2.5 Discussion	45
2.6 Conclusions	48
2.7 Non-Author Acknowledgements	48
2.8 Disclosure statement.....	49
2.9 References	49
Chapter 3: Developing 3D Scaffolds in the Field of Tissue Engineering to Treat Complex Bone Defects	54
3.1 Abstract	54
3.2 Introduction	55
3.3 Materials and Methods	57
3.3.1 Development of hybrid spools.....	57
3.3.2 Chemical composition testing	58

3.3.3 3D printing and mechanical testing	58
3.3.4 Cell incorporation within log-pile scaffolds	59
3.4 Results.....	60
3.4.1 3D printing using hybrid PCL spools	60
3.4.2 Composition and mechanical properties of printed scaffolds	62
3.4.3 3D printing of complex porous geometries	63
3.4.4 Cell incorporation within log-pile scaffold	65
3.5 Discussion	67
3.6 Conclusions	69
3.7 Non-Author Acknowledgements	70
3.8 Disclosure Statement	70
3.9 References	70
Chapter 4: Perfusion Directed 3D Mineral Formation within Cell-Laden Hydrogels	74
4.1 Abstract	74
4.2 Introduction	75
4.3 Materials and Methods	77
4.3.1 3D printing of frames and pipes	77
4.3.2 Design and fabrication of polycarbonate bioreactor.....	77
4.3.3 Gelatin methacrylate (GelMA) synthesis	78
4.3.4 Cell culture and perfusion setup	78
4.3.5 Cellular viability	79
4.3.6 MicroCT analysis	79
4.3.7 Histological analysis.....	80
4.3.8 COMSOL modeling	81

4.3.9 Statistical analysis	83
4.4 Results.....	83
4.4.1 Design and fabrication of a plug-and-flow construct.....	83
4.4.2 Perfusable GelMA laden hydrogels containing Saos-2 cells	85
4.4.3 Channel mineralization and modeling.....	88
4.4.4 Histological analysis and quantification.....	91
4.4.5 Construct scalability	93
4.4.6 Estimation of the influence of mineral formation on oxygen diffusion	95
4.5 Discussion	96
4.6 Conclusions	99
4.7 Non-Author Acknowledgements	99
4.8 Disclosure statement.....	99
4.9 References	100
4.10 Supplementary figures	105
Chapter 5: Ongoing Work and Future Recommendations	109
5.1 Introduction	109
5.2 The addition of endothelial cells to the perfusable system	111
5.3 In vivo extension of model system.....	115
5.4 Final remarks.....	118
5.5 References	118
VITA	122

LIST OF FIGURES

Figure 2.1: Cellular encapsulation schematic. (A) Schematic of surface tension encapsulation technique. 75,000 Saos-2 cells in 20 μ l aliquots were combined with 130 μ l of prepolymer solution containing .25% photoinitiator and pipetted dropwise into a bed of vegetable oil. UV light was cast onto the hydrogel drops for one minute to cure before being rinsed with PBS and transferred into incubation media. (B) Cured hydrogel spheres containing encapsulated cells resembled disc like structures with dimensions approaching 6mm x 6mm x 4mm (scale bar = 5mm). (C) Mechanical data of various GelMA (w/v) concentrations modified from previous work. [18].....37

Figure 2.2: Cellular viability and activity within degradable hydrogel scaffolds of different stiffness. (A) Cells were grown within hydrogel constructs for 5 days and analyzed for cellular viability using calcein-AM (live = green) and ethidium homodimer (dead = red). Fluorescent images of live/dead cells show live and dead cells throughout the entire scaffold. (B) Representative schematic of the region of interest used to standardize measurements between fixed and sectioned histological samples. Areas between the center of the slices and the peripheries were used due to sectioning artifacts. (C) Cells stained with DAPI were counted in the ROI of histological slices for 3 day, 7 day, and 14 day timepoints. Increases in cellular population over time within the hydrogels were evident in all samples at all timepoints (n = 3; * = p < 0.05). (C) Saos-2 cells tagged with green fluorescent protein (GFP) showed activity in all samples well over one month after encapsulation (scale bar = 100 μ m). (D) Fluorescence in histological samples due to DAPI staining allowed for apparent porosity of hydrogels containing encapsulated cells to be measured for 3 day, 14 day and 49 day timepoints. Blue coloring represents GelMA staining while

black coloring represents apparent void space. All gels degraded significantly over time ($n = 3$; $* = p < 0.05$; scale bar = $100\mu\text{m}$).....40

Figure 2.3: Nuclear and cytoskeleton staining of encapsulated Saos-2 cells. (A) Cells were grown within hydrogel constructs for either 3, 7, or 14 days, fixed, sectioned, and stained for f-actin (red = phalloidin) and counterstained for nuclei (blue = DAPI). Representative pictures at 7 days (scale bar = $100\mu\text{m}$) and 14 days (high resolution; scale bar = $20\mu\text{m}$) show distinct morphological differences in the ROI of samples of different stiffness at all timepoints. (B) Histological samples stained with phalloidin and counterstained with DAPI were analyzed for morphological differences in the nuclei and lacunae at 3 day, 7 day, and 14 day timepoints. Measurements showed significant differences in aggregate nuclear diameters and areas, as well as aggregate lacunae diameters and areas, for softer hydrogels over time ($n = 3$; $* = p < 0.05$).....42

Figure 2.4: Mineralization and microCT of encapsulated Saos-2 cells. (A) Cells were grown within hydrogel constructs for 7 days and were subsequently placed in osteogenic media for an additional 14 days. Constructs were fixed, sectioned, stained for mineral deposition (red = alizarin red S) and counterstained for nuclei (blue = DAPI). Representative pictures for all samples show distinct difference in the mineral located within the ROI for different gel stiffnesses (top scale bar = $100\mu\text{m}$; bottom scale bar = $20\mu\text{m}$). (B) Cells were grown within hydrogel constructs for 14 days and were subsequently placed in osteogenic media for an additional 14 days. Samples were analyzed via microCT for total mineral within the constructs of different stiffnesses. (C) Histological samples stained with alizarin red S and counterstained with DAPI were analyzed for mineral cluster area and area fraction of mineral coverage within the ROI and showed significant differences for implants of varying moduli ($n = 2$; $* = p < 0.05$). MicroCT scans were analyzed

for total mineral throughout the constructs and showed no significant differences between implants of varying moduli (n = 3).....44

Figure 3.1: 3D printing schematic using hybrid PCL spools. (A) The raw material is fed into the filament extruder creating a long strand of three polymer spools (PCL, PCL-HA, and PCL-PLA). (B) A commercially available MakerBot Replicator 3D printer. (C) The printer settings are set for each filament spool, respectively. (D) The model of the log-pile scaffolds and the printed counterparts to the right. Scale bar: 2mm. HA, hydroxyapatite; PCL, polycaprolactone; PLA, polylactic acid.....61

Figure 3.2: Printed scaffold compositions and mechanical properties. (A) High-resolution TGA of polymer spools. (B) Results in tabular form showing the degradation points and percentages for each compound. (C) Compression testing apparatus to obtain mechanical properties of log-pile scaffolds. (D) Stress-strain plots and bar graphs of modulus and maximum stresses for each polymer spool (n=5). TGA, thermogravimetric analysis.....63

Figure 3.3: 3D printing of complex geometries. (A) Cartesian data for a human femur were placed into the MakerBot Desktop. (B) A slice from the diaphysis of the femur was taken and Lattice meshed in Meshmixer. On the right is the 3D printed model in PCL. (C) Longer slice from the diaphysis was Voronoi meshed in Meshmixer to create a hollow cage-like representation of the outside femur. On the right is the 3D printed PCL model.....65

Figure 3.4: Incorporation of cells within 3D printed scaffolds. (A) Schematic representation of the process used for incorporating living cells within printed scaffolds. The case was slightly

larger than the 6mm³ log-pile structure to allow for GelMA-cell solution perfusion. **(B)** PCL scaffold infused with 7% GelMA containing 15% (v/v) MiO orange coloring to show complete perfusion of GelMA throughout the scaffold (left to right: PCL GelMA top, PCL GelMA middle, PCL GelMA bottom). **(C)** Live (green)/Dead (red) calcein-AM/ethidium homodimer pictures from PCL/PLA scaffold (left to right: PCL-PLA GelMA top, PCL-PLA GelMA middle, PCL-PLA GelMA bottom). GelMA, gelatin methacrylate.....66

Figure 4.1: Design and performance testing of 3D-printed construct and bioreactor apparatus. Schematic and representative images of the mechanically supportive ABS frame with inserted pipe before **(A)** and after **(B)** photopolymerization of GelMA, and after dissolution of the sacrificial PVA pipe **(C)**. Schematic image of a two-piece polycarbonate bioreactor containing a PDMS gasket between layers **(D)** and leakage test of polycarbonate bioreactor showing liquid-tight seal in machined device **(E)**. Complete bioreactor setup inside a standard cell culture incubator **(F)**.....85

Figure 4.2: Perfusion can direct mineral deposition. Schematic representation of outcomes following osteogenic induction under **(A)** perfusion or **(F)** static culture conditions. Cell viability by fluorescent live (green)/dead (red) staining after perfusion **(B, C)** or static culture **(G, H)** conditions for either 1 **(B, G)** or 14 days **(C, H)** respectively. Brightfield microscopy showed an accumulation of an opaque matrix surrounding the perfused pipe **(D)** that was not evident in static constructs lacking a pipe **(I)** (scale bar: 400µm). Micro-CT imaging demonstrated mineral deposits surrounding the perfused pipe **(E)**, whereas mineral accumulated only at the periphery of constructs maintained in static conditions **(J)**.....87

Figure 4.3: MicroCT analysis of mineral deposition. Representative microCT image of total mineral deposition after culture in osteogenic media under static (S) or perfused (P) conditions for 1, 2, or 4 weeks (A). For representative images, the entire frame was digitally contoured in order to visually show how mineralization occurs in static samples immersed in osteogenic media versus samples perfused directly with osteogenic media. Mineral volume deposited around pipes after 1, 2, or 4 weeks of both static osteogenic culture and osteogenic media perfusion showed significant increases in volume after 4 weeks (4wk static and 4wk flow n=7, 2wk flow n=8, rest n=6. * p<0.05 via one-way ANOVA) (B). Density of mineral deposited around pipe after 1, 2, or 4 weeks of both static osteogenic culture and osteogenic media perfusion remained constant at every time point (4wk static and 4wk flow n=7, 2wk flow n=8, rest n=6) (C).....90

Figure 4.4: Histological analysis of perfused constructs. Cellular localization decreases, and matrix mineralization increases as function of distance from the perfused channels. Representative Alizarin Red (A) and H&E (B) histology stains of construct samples after either 1, 2, or 4 weeks of perfusion with osteogenic media (scale bar: 500µm). Box plot analysis of H&E samples was used to measure cell number in measured increments away from the central pipe (scale bar: 325µm) (C). Histogram quantification of the number of cells as a function of distance away from the lumen for 1, 2 and 4 week perfused samples shows that cell number decreases as the distance from the perfused channel increases (n=3, *p<0.05 via one-way ANOVA) (D).....92

Figure 4.5: Schematic representing the scalability of perfusable constructs. Multiple channels spaced at optimal distances are capable of being perfused via one inlet (A). COMSOL modeling of oxygen diffusion between one channel (B Top) and two channels spaced 1mm apart (B Bottom), as well as COMSOL modeling of the radial oxygen consumption by cells around the

channels within cell laden constructs spaced 1mm apart (C) was used to determine optimal pipe spacing in larger constructs. Schematic of a scaled cell-laden construct (D) and corresponding ABS cage (6x6x6 mm³) (E). CAD isometric view of a machined, two-piece polycarbonate bioreactor containing a PDMS gasket between layers (red) (F). Micro-CT imaging of mineral deposition surrounding pipes (G, side view; H Cross-sectional view) after four weeks of perfusion with osteogenic media showed that the model system could be easily scaled. Representative Alizarin Red histology of a large-scale construct after perfusion with osteogenic media for 4 weeks showed robust mineralization (I) (scale bar: 500µm).....94

Figure 4.6: Effect of mineral formation on oxygen diffusion radially across the channel.

Surface slices were obtained from 3D data sets in MIMICS, and mineral area was measured (A-B). A schematic model showing the three domains used for COMSOL modeling (C). Table shows the various parameters used to calculate Domain 3 (D, Top table). Simulation of oxygen diffusion for weeks 1, 2 and 4 (D, Bottom) (white arrows showing the donut shell thickness). Distribution of oxygen radially away from the channel surface for weeks 1, 2 and 4 along with control without any mineral deposits (E).....96

Figure S4.1: Polycarbonate base plate dimensions and scale.....105

Figure S4.2: Polycarbonate top plate dimensions and scale.....106

Figure S4.3: Representative series of static and perfused images showing contrast of deposited mineral from background and frames after microCT scanning. Representative whole views of in-tact constructs within 16mm diameter sample holders after scanning show

contrast of deposited mineral (white) from background (grey) and sample frames (dark grey). To normalize data, only mineralized pipes were contoured for mineral (ROI).....107

Figure S4.4: Total mineral quantification. Total mineral deposited around pipes after 1, 2, or 4 weeks of both static osteogenic culture and osteogenic media perfusion showed significant increases in deposition after 4 weeks (4wk static and 4wk flow n=7, 2wk flow n=8, rest n=6. * p<0.05 via one-way ANOVA).....108

Figure 5.1: MicroCT analysis of mineral deposition within a co-culture single pipe system. HUVECS (H) were either seeding along the perfusable channels (Channel) or added in a 2:1 ratio with Saos-2 cells in the GelMA matrix (Bulk) and were either perfused with osteogenic media (Flow) or left in static control wells (Static). After two weeks of perfusion, HUVECS encapsulated in the bulk material significantly increased Saos-2 mineral deposition as compared to the constructs containing HUVEC lined channels and their static controls (* p<0.05 as compared to H Bulk Flow 2Wk, n=5).....113

Figure 5.2: MicroCT analysis of mineral deposition within a co-culture double pipe system. HUVECS (H) were added in a 2:1 ratio with Saos-2 cells (S) in the GelMA matrix and perfused with osteogenic media for either 1 or 2 weeks. After two weeks of perfusion, HUVEC+Saos-2 constructs did not show a significant increase in mineral deposition as compared to samples containing only Saos-2 cells. (*p<0.05 as compared to S+H Flow 2Wk; \$p<0.05 as compared to S Flow 2Wk; n=3 for HUVEC only samples, n=5 for rest).....114

Figure 5.3: Ectopic implantation of thermoplastic ABS frames containing primary BMSC and VEC cells. 6x6x6mm³ frames containing encapsulated BMSCs, VECs, or a combination of both were implanted subcutaneously in c57BL/6J mice (red arrows, top X-ray). After two weeks of implantation, the implants were retrieved and showed blood invasion and minimal host ingrowth in the cell-laden constructs (bottom)*.....116

Figure 5.4: Cartoon depicting surgical anastomosis of perfusable structurally supported cell-laden constructs. (A) 3D printed constructs containing cell-laden GelMA and perfusable channels will be anastomosed directly into the host femoral artery and sewn in place via 3D printed anchor grommets. (B) 3D rendering of structural frame (blue) and stainless-steel catheter connections (grey)*.....117

CHAPTER 1: INTRODUCTION

1.1 The need for bone tissue engineering

Over the past decade, there has been an increased focus on providing a tissue engineered solution for orthopedic bone defects which cannot heal properly. These types of defects, many of which involve bone fracture, can be caused by birth disorders, tumors, infections, revision surgeries, and high impact traumas and pose a large financial burden on the medical community.[1-5] In fact, as of 2010 the American Academy of Orthopedic Surgeons estimated that there were over 6 million fractures annually in the United States alone resulting in hundreds of thousands of bone graft procedures costing approximately \$2.5 billion dollars.[4, 6]

It has been estimated that approximately 10% of all bone fractures do not heal properly and therefore require clinical intervention.[5] These types of segmental bone defects, which are commonly referred to as critically sized defects, include fractures that either cannot heal naturally without intervention, regenerate less than 10% over the course of the lifetime of the injury, or are approximately 2 to 3 times larger than the diameter of the injured bone.[6] As segmental bone defects come in different shapes and sizes, there are a range of clinical techniques used to aid the bone healing process. In general, these solutions rely on either vascularized autografts, allografts, synthetic implants, or specialized techniques such as distracted osteogenesis[1, 6-8].

The preferred treatment of a segmental bone defect is a vascularized bone graft, such as pedicled vascularized bone graft used in repairing broken wrists or fractures in the femoral neck and hip.[6, 9] These types of grafts are harvested from the patient itself and include host vasculature, thereby

allowing for direct anastomosis to the local blood supply. Vascularized bone grafts have been shown to dramatically enhance healing times, however they do include drawbacks such as donor site morbidity and the necessity of shielding the surgical site from weight bearing applications during the healing process.[6, 9, 10]

Due to the donor morbidity associated with vascularized bone grafts, allografts are a widely available solution as they are not patient derived.[1] Additionally, allografts can serve as solutions to fractures that will necessitate load bearing post-surgery, making them an attractive option in the treatment of a segmental defects.[1, 6] However, as allografts are not vascularized and the material is not patient specific, concerns such as disease transmission, the possibility of implant failure, and on rare occasions host rejection, remain.[6]

Implants are another common solution to repairing segmental bone defects and can be made from a variety of materials. For instance, intramedullary nails, which are the standard of care for injuries such as tibial shaft fractures, have been shown to be highly biocompatible.[5, 8] However, as the implants are generally not made from organic material, the possibility of corrosion, wear, and fibrous encapsulation remain issues that could lead to implant failure or secondary surgery.[11, 12] Fortunately, implants made of stainless steel and titanium have mitigated these concerns greatly.

Techniques such as distraction osteogenesis have also been used to treat segmental bone defects with great success.[6, 13] In this particular technique, the cortical shell of the fractured bone is cut, leaving the periosteum and medullary cavity intact.[6] The cut is then stabilized with an external fixator that extends the bone segment between the cut and the defect at a rate of 1mm/day,

thereby “distracting” the natural callus formed during bone repair.[6, 14] Essentially, the “distraction” of the callus stimulates bone formation *de novo* through both mechanical and biological stimulation, and eliminates the need for graft material.[14] However, while the external fixator makes weight bearing possible, its application may be extremely cumbersome to the patient and the time frame for healing could be prolonged.[6]

Autografts, whether they are vascularized as explained before or avascular, remain the current gold standard for bone replacement in a clinical setting.[15] Not only are they harvested from host material, but they generally include the inherent structure and growth factors needed for bone repair.[6] However, while autografts provide an excellent option for the repair of segmental defects, they do still have drawbacks such as donor site morbidity and limited availability in elderly patients.[6] As such, researchers have attempted to find possible alternative solutions in the form of tissue engineered constructs. For instance, in one such case a β -tricalcium phosphate matrix combined with recombinant human homodimeric PDGF subunit B, a peptide signaling molecule involved in bone repair, were compared against autografts in ankle arthrodesis cases.[16] It was shown that while the fusion rates were similar between the two groups, the PDGF constructs seemed to reduce the patient pain. Regardless, while current clinical practices for the repair of segmental bone defects have been very successful, they do all have their own drawbacks and research into alternative solutions, such as tissue engineered constructs, is necessary to improve patient care and advance the field of orthopedics.[5]

1.1.1 Creating a tissue engineered solution

The noted issues associated with clinical approaches to treat segmental bone defects and fractures highlight the need for a robust and reproducible tissue engineered bone replacement. More specifically, this replacement must be capable of providing a suitable microenvironment which not only is able to house appropriate cells for regenerative purposes, but also capable of recruiting cells *in vivo* to support a complete restoration of the defective bone tissue.[7] Not only will this improve the quality of life for those maligned with orthopedic defects of any kind, but will hopefully reduce the burden on healthcare systems around the world. However, before attempting to create a tissue engineered solution, the complex architecture of native bone needs to be understood.

1.2 The structure and composition of bone

Bone is a hard, composite tissue which houses the body's organs, provides the structural support needed for the body's motion, and serves as the calcium repository for the human body.[17] Additionally, due to advances in bone biology over the past decade, bone has also been identified as an endocrine organ which is vital in regulating the body's glucose and testosterone levels.[17] As such, not only must a healthy human skeleton have sufficient structural properties, it must also be capable of continuous adaptation and remodeling through complex interplays between cellular, organic, and inorganic components.[17, 18]

1.2.1 Cellular component

There are three main types of bone cells which reside within the bone hierarchy that derive from either the mesenchymal or hematopoietic stem cell lineages. Two of these cells, osteoclasts and osteoblasts, are directly responsible for the bones ability to remodel itself over time via coupled actions.[6, 18] The first cell, called osteoclasts, are multinucleated cells which originate from mononuclear hematopoietic stem cells and are responsible for the resorption stage of bone remodeling.[19-21] Osteoclast precursor cells are found circulating in the blood and, when stimulated through a combination of signals expressed by osteogenic lineage cells such as receptor activator of nuclear factor- κ B ligand (RANKL) and macrophage colony-stimulating factor (M-CSF), fuse together into large multinucleated osteoclasts.[6, 18, 19] Once fused, mature osteoclasts attach to the surface of the bone via α v β 3 integrins and acidify the environment on the bone surface through H⁺ATPase-mediated extracellular proton transport, leading to the breaking down of the organic and inorganic bone components.[18, 21, 22] The second type of bone cells, called osteoblasts, originate from the non-haematopoietic cells within the bone marrow.[6] Once osteoblasts are mature, they are primarily responsible for secreting osteoid, the main organic component of bone which contains primarily type-I collagen and other non-collagenous proteins.[20] As the resorbed bone is replaced by the osteoblasts, a process that can take up to 3 months, mature osteoblasts follow one of three paths.[20, 23] Some of the osteoblasts will flatten, become quiescent, and line the surface of the newly formed bone, while others will simply die via apoptosis.[23, 24] The third pathway, however, gives rise to the third bone cell type, called the osteocyte. Osteocytes are osteoblasts which have become encased within the lacunae of mineralized osteoid bone matrix.[21] Osteocytes, which comprise 90 percent of the total number of bone cells within the skeleton, develop long dendritic processes which facilitate communication

between other cells in the mineralized matrix and the bone lining cells via microscopic channels between the lacunae called canaliculi.[20, 21, 25]

1.2.2 Bone matrix

The bone matrix is a complex combination of organic and inorganic components and comprises approximately 90% of the entire tissue volume, the rest of which is taken up by cells and blood vessels.[20, 21, 26] The organic matrix component, which is mainly a combination of different forms of collagen, accounts for about 20% of the matrix and gives the bone tensile strength.[20, 21, 26] The inorganic matrix component, which is the mineral component of bone, is responsible for approximately 65% of the matrix by weight and is responsible for the bones compressive strength.[20, 21, 27]

Type I collagen accounts for roughly 90% of the entire organic matrix component, the rest of which is a mixture of type V and XII collagen and several non-collagenous proteins.[20, 21, 28] Of the non-collagenous proteins, osteocalcin is the most abundant as it is readily secreted by osteoblasts and has a high binding affinity to hydroxyapatite mineral.[21, 29] Furthermore, osteocalcin has been shown to be a key regulator of glucose metabolism and testosterone levels within the body, thereby making the skeleton an endocrine organ.[17] Osteopontin is the second most abundant non-collagenous protein in the bone matrix and is secreted by numerous bone cells and progenitors. Due to its acidic nature, osteopontin readily binds Ca^{+2} ions and is responsible for both the suppression and promotion of mineral formation. Additionally, osteopontin contains numerous Arg-Gly-Asp (RGD) motifs and readily aids cell adhesion and movement.[21, 30] Other notable proteins found in the bone matrix include bone phosphoproteins, bone sialoprotein, and

numerous proteoglycans which all are attributed to regulating how cells interact with the matrix, how cells communicate with one another, and how mineralization occurs.[20, 26]

The inorganic components of bone are a combination of numerous ions and a form of apatite mineral. Ca^{2+} , PO_4^{3-} and CO_3^{2-} are among the main ions found in the bone, along with Mg^{2+} , Fe^{2+} , Na^+ , K^+ , F^- and Cl^- and serve as the major reservoir source for the rest of the bodies calcium and phosphorous.[20, 21, 31] Apatite mineral, which is the major inorganic component, comprises approximately 65% of the total mass of the bone[32] and is not pure hydroxyapatite ($\text{Ca}_{10}(\text{PO}_4)_6(\text{OH})_2$), but rather a form of apatite that contains acid phosphate groups and carbonate ions but no hydroxyl groups.[20, 21]

1.2.3 Cortical and cancellous bone

Natural bone consists of hard cortical bone, spongy cancellous bone, and bone marrow. Cortical bone, which has a high mechanical strength and comprises the outer hard layer of bone, is responsible for approximately 80% of the human skeleton weight.[21, 33] Cancellous bone, on the other hand, has a low mechanical strength as compared to cortical bone and is a porous structure that contains bone marrow. Bone marrow contains stem cells capable of differentiating into osteoblasts, adipocytes, chondrocytes and fibroblasts, as well haematopoietic stem cells capable of differentiating into myeloid lineage cells, lymphoid lineage cells, and osteoclasts.[34] Additionally, it is speculated that since oxygen tension ranges from 1% to about 7% of atmospheric oxygen levels within the marrow depending on the location of capillaries, specific niches are formed which enable populations of stem cells to remain undifferentiated.[34, 35]

Depending on the arrangement of the cortical bone, cancellous bone, and bone marrow, the bones in the human skeleton are classified as either long bones, short bones, flat bones, or irregular bones.[21] The first group, long bones, are bones such as the femur and tibia. These types of bones are generally longer than they are wide and consist of a long cortical shaft called the diaphysis which surrounds a medullary cavity containing bone marrow.[20] As you move away from the center of the diaphysis of a long bone, referred to as the midshaft, the cortical walls become thinner, the bone diameter widens, and there is an increasing amount of cancellous bone in the center underneath the cortical shell.[20] This area of increased cancellous bone is called the metaphysis and supports the growth plate, a layer of hyaline cartilage that separates the metaphysis from the rounded end of the long bone.[20] This rounded end, called the epiphysis, is filled with cancellous bone and bone marrow and has a layer of articular cartilage directly next to the bone joint.

1.2.4 Hierarchy of the long bone

Regardless of the geometrical arrangement of cortical and cancellous bone, their basic hierarchical structure is common through all native bone. As stated previously, osteoblasts secrete osteoid, the mineralized extracellular matrix comprised of collagen and non-collagenous proteins. The collagen polymerizes quite rapidly to form collagen fibrils that serve as the deposition points for apatite crystals. Alkaline phosphatase, an enzyme which is also secreted by osteoblasts, aids in phosphate and calcium deposition and causes a rather organized crystal deposition along these collagen fibrils.[31] These mineralized collagen fibrils are packed tightly in lamellar units and represent the basic hierarchical unit for mature cortical and cancellous bone.

In cancellous bone, the lamellar units are arranged in functional units called trabeculum. Geometrically, the trabeculae are arranged as a porous mesh of rods and struts that increase the compressive strength of the bone. The orientation of the trabeculae change over time in a highly organized way to support the areas of the bone that experience the most strain.[21]

Similar to cancellous bone, the lamellar units also form the functional unit of cortical bone called the osteon. Osteons, which are anywhere from 100 to 500 μm in diameter, are formed by concentric rings of lamellar units surrounding a central channel containing blood vessels and nerves called the Haversian canal.[20, 36] Within each lamellar ring, the collagen fibers are oriented parallel to each other, but run in different directions to adjacent lamellar units.[21] Osteocytes are located in lacunae within the lamellar rings and extend processes radially outwards from the Haversian canal through a network of canaliculi, thereby ensuring the diffusion of nutrients throughout the bone tissue as well as providing a mechanosensation communication network capable of passing signals throughout the bone structure.[20, 25] At the edges of osteons is a thin sheet of bone matrix called the cement line within which most canaliculi and collagen fibers stop, essentially isolating each osteon from one another.[20, 25] Running transverse throughout the osteon network within cortical bones are small channels called Volkmann's canals that effectively connect the vertical Haversian network. Additionally, since these small canals run the entirety of the cortical bone, they serve to transmit blood vessels and nutrients from the outside periosteum surrounding the bone to the endosteal surface surrounding the cancellous bone, thereby creating the vascular lining of the medullary cavity.[21, 36]

The periosteum is a thin sheet of highly vascularized tissue which surrounds the outer surface of bone. Structurally, the periosteum is comprised of an outer fibrous layer and an inner vascularized

cellular layer. The inner layer, also called the osteogenic layer, contains cells that are capable of differentiating into osteoblasts while the outer layer connects bones to tendons and ligaments.[20, 25]

1.3 Bone vasculature and its role in bone growth and homeostasis

Although much of the focus on the bone hierarchy revolves around its load bearing structure, healthy bone is also highly vascularized. In order to provide adequate nutrients and oxygen to the tissue, as well as ensure the removal of metabolic waste, bone contains an intricate vascular network that receives up to 11% of the total cardiac output of the human body.[34, 37] In fact, in native bone the vascular network is arranged in such a way that no area is further than 100 μm from a nutrient source, ensuring that the diffusion of nutrients and systemic signaling molecules is not impeded to any bone cells.[2, 38]

There are four main regions of arterial input into the human long bone: the diaphyseal nutrient arteries, the metaphyseal arteries, the epiphyseal arteries, and the periosteal arteries.[2, 39] The largest arteries are the diaphyseal nutrient arteries which supplies up to 50% of all blood to the human long bone and enter into the central medullary cavity as well as regions of the metaphysis and cortex.[2] The diaphyseal nutrient arteries, which are located on the outer bone cortex, enter the medullary canal through small openings called foramina and are generally accompanied by large veins. As these arteries pass through the cortical bone, they branch into the Haversian and Volkmann canals in the osteons, and sinusoids within the marrow.[2, 40] Similar to the diaphyseal nutrient arteries, the metaphyseal and epiphyseal arteries enter into the epiphysis and metaphysis through their respective vascular foramina and serve to reinforce the vascular branches from the

diaphyseal arteries. Finally, the periosteal arteries, which are located on the inner side of the highly vascularized periosteum, enter the long bone through the Volkmann canals to supply the areas of the cortex not supplied via the diaphyseal arteries.[2] After circulating through the bone, the blood leaves through the central sinus veins.[2, 41]

In addition to providing nutrient exchange and waste removal, the bone vasculature is a key component to bone growth and remodeling, as well as fracture repair. In all three instances, the vasculature, or lack thereof, can be considered the regulatory force for how the bone is grown or repaired.

1.3.1 New bone growth

Bone is formed by intramembranous and endochondral ossification, depending on the type of bone being formed. Intramembranous ossification is the method in which flat bones are formed while long bones are formed by both intramembranous and endochondral ossification.[42, 43] In both instances, however, vasculature, or the lack thereof, mediates the growth process.

In intramembranous ossification, the growth space is first invaded by capillaries that are followed by mesenchymal cells which differentiate into osteoblasts. These first osteoblasts form a cluster, called the ossification center, and proceed to secrete osteoid which hardens within a few days. As the osteoblasts within the hardened ossification center differentiate into osteocytes, new osteoblasts form on the outside edges of the new bone. This process continues, and the new bony matrix begins to fuse together around the capillaries creating the trabeculae of the newly formed cancellous bone. As the trabecular matrix continues to grow, osteoblasts and other mesenchyme

cells continue to aggregate on the outside of the trabeculae and form the beginning layer of a new, highly vascularized periosteum. Eventually, osteogenic cells from the periosteum form cortical hard bone surrounding the cancellous tissue.[42, 43]

Unlike intramembranous ossification, endochondral ossification occurs as vasculature invades cartilage regions. In new long bone formation, the mesenchymal cells originally differentiate into chondrocytes which create a cartilage template that will slowly be replaced by bone. Surrounding the growing cartilage template of the new bone are a group of mesenchymal cells which form the perichondrium that will eventually become the periosteum of the long bone.[2, 43, 44] As the region of cartilage grows through chondrocyte proliferation and secretion of type II collagen, the chondrocytes in the center enlarge into hypertrophic chondrocytes.[44] The hypertrophic chondrocytes attract blood vessels from the surrounding perichondrium via the release of vascular endothelial growth factors, thereby causing blood vessels to invade the hypoxic cartilage environment and, as was also seen in intramembranous ossification, bring with them mesenchymal cells which differentiate into osteoblasts.[2, 43, 44] As the osteoblasts and vasculature continue to aggregate and replace the cartilage and chondrocytes in the center of what will eventually be the medullary cavity of the long bone diaphysis, they begin depositing bone within the structure, creating what is called the primary ossification center.[2, 43, 44] As bone and vasculature replace the cartilage in the diaphysis of the newly forming long bone, chondrocytes and cartilage continue to grow outward from the primary ossification center, elongating the bone and creating what will eventually be the proximal and distal epiphysis of the bone.[2, 43] The remodeling and organization in the diaphysis continues as osteoclasts are recruited, and the reorganization that occurred in the medullary repeats in the two epiphyseal regions, creating secondary ossification centers.[2, 43, 44] In long bones, chondrocytes continue to grow and proliferate between the

primary and secondary ossification centers and form a flattened, disc shape of collagen which directs bone growth, called the growth plate.[44] On the edges of the growth plates, chondrocyte proliferation drops and the chondrocytes serve as a reservoir for future growth.[44]

1.3.2 Bone remodeling

As stated previously, osteoblasts and osteoclasts are the two main bone cells involved in bone remodeling, a process that occurs through the entire lifespan of bone.[2] However, while the osteoblasts and osteoclasts are generally the focus of the remodeling process, the bone vasculature serves as a key mediator and is integral to the bone metabolic unit (BMU) within which remodeling takes place.[23] In fact, it has been shown that when the blood supply is inhibited or damaged, necrosis and bone loss occurs as bone remodeling is impaired.[34]

The bone remodeling process is fairly well defined in the context of the aforementioned BMUs. As bones age, mature osteoblasts lose their ability to secrete osteoprotegerin (OPG), a cytokine decoy receptor that binds to RANKL, a ligand also secreted by osteoblasts. Without OPG competition for RANKL, RANKL is free to bind to osteoclast progenitor cell RANK receptors, thereby allowing for osteoclast differentiation and activation.[2, 23] Accordingly, when areas of cortical and cancellous bone age, osteoclasts are signaled to begin resorption and begin resorbing bone in a trench like fashion called a Howship lacunae.[2, 23] As the resorption is occurring, mesenchymal osteoprogenitors are directed into the BMU and begin new bone deposition in the resorbed surface, a process that can take up to 3 months to complete.[2, 23]

1.3.3 Fracture repair

As can be expected, the normal stages of fracture repair are also highly tied to the bone vasculature. Unlike soft tissue, bone undergoes a complex healing process that involves intramembranous and endochondral bone formation as well as bone remodeling, all of which are dependent on a healthy skeletal vasculature.[2] More specifically, when a fracture occurs, the damage to the intraosseous vasculature and periosteum are what initially drives the regenerative process.

When a fracture occurs, the blood supply of the bone is disrupted, leading to hypoxic conditions in the surrounding tissue.[34, 39] In the first stage of repair, the blood around the injury clots, forming a hematoma, and the surrounding tissue becomes inflamed.[42, 45] The hypoxic conditions are extremely important in this first phase of fracture repair as they create a cascade of events which cause a release of several growth factors and cytokines that recruit endothelial cells and direct cellular differentiation.[2] As the hematoma is formed, hypoxic osteoblasts release vascular endothelial growth factor (VEGF) which stimulates angiogenesis through the recruitment of endothelial cells.[46] However, as endothelial cells are recruited to the fracture site, stem cells, and inflammatory cells, such as neutrophils, travel alongside the invading vasculature.[46, 47] The inflammatory cells release proangiogenic cytokines which aid in capillary repair while the VEGF stimulates the invading endothelial cells to release osteogenic cytokines that promote osteoblast differentiation and recruitment.[46] As the cells within the hematoma die, invading fibroblasts form a loose connective tissue, called granulation tissue, in the injury site alongside the newer blood vessels.[39] Eventually, this tissue is replaced by fibrocartilage as the hypoxic environment drives the differentiation of chondrocytes, thereby stabilizing the fracture and forming the internal callus.[2, 42] Concurrent to the internal callus forming, the periosteum begins to undergo

intramembranous bone formation, leading to the creation of an external callus.[39, 42] The two calluses eventually combine and form a stabilizing large fracture callus. Once the fracture callus has formed, the internal callus is replaced by woven bone, which unlike lamellar bone is an irregular grouping of collagen.[20, 39] After the formation of this hard callus, the bone remodeling process begins and the fracture callus is gradually replaced with lamellar bone.[39]

1.4 Challenges of developing a tissue engineered construct

In order to create a tissue engineered bone substitute, numerous variables need to be taken into account. A complete solution must be capable of supporting the numerous multicellular interactions required for functional bone growth, must address the structural complexity of bone, and must contain a defined vasculature or porosity capable delivering nutrients in a controlled and ordered way.[48-52] Unfortunately, a complete solution which incorporates all of these areas has not been developed.

1.4.1 Challenge 1 – Soft matrix for cellular encapsulation

Traditional strategies for bone tissue engineering have relied upon creating scaffolds that provide structural support containing seeded osteo-competent cells.[53] Hard bioceramics such as hydroxyapatite and calcium phosphate have shown good strength and integration with native bone, but seeding cells post manufacturing sometimes result in an inhomogeneous distribution of cells.[53, 54] Additionally, with the lack of a well-defined vasculature and proper nutrient exchange, such approaches generally result in construct mineralization only at the peripheries of the scaffold and the presence of a necrotic core.[2, 55]

One popular manufacturing approach in bone tissue engineering that has received increased attention over the past decade involves cellular encapsulation within a soft biomaterial. In general, cellular encapsulation usually involves either synthetic or natural hydrogels with which cells can be incorporated into the matrix *de novo*. Additionally, cellular encapsulation can allow for the cells to be incorporated at specific locations and densities within the construct, thereby improving upon the cell seeding limitations previously mentioned.[56-59]

In the context of creating a bone tissue substitute, it is necessary to ensure that the base material not only closely mimics the native bone extracellular matrix, but also supports cell viability and proper tissue growth. As 90% of the organic bone extracellular matrix is comprised of collagen, naturally derived biomaterials such as gelatin are widely used as a starting material.[60] More specifically, collagen derived cross-linkable hydrogels such as gelatin methacrylate (GelMA) are extremely attractive as scaffold materials for bone tissue engineering due to the fact that they have tailorable mechanical properties, exhibit minimum immunogenicity, are biodegradable, and have tunable porosities needed for proper nutrient diffusion.[58-61]

Although cell encapsulation within a hydrogel is an appealing approach for the incorporation of relevant cells and growth factors into a bone tissue substitute, several issues need to be addressed. First, it is important to know how encapsulated cells function and remodel the hydrogel environment, as well as how the encapsulation process influences cellular viability and function. Additionally, in order to create a clinically relevant scaffold for bone tissue engineering, both the hydrogel biocompatibility as well as load bearing capacity needs to be taken into account,

indicating that the soft hydrogel would need to be encased in a load bearing material for *in vivo* applications.[62, 63]

1.4.2 Challenge 2 – Strategies for combining soft and hard components

While cellular encapsulation provides a means for the reliable spatial distribution of cells within a hydrated construct, the structural integrity and load bearing capabilities of hydrogels are not sufficient when creating a possible device for implantation into bone. Additionally, apart from the structural strength of the engineered device, careful attention must be paid to patient-specific geometries when designing a possible bone tissue substitute. Unfortunately, while traditional fabrication methods, such as freeze drying, solvent casting, porogen leaching and gas foaming are capable of creating macroscopic patient specific geometries for a bone tissue construct, they are not compatible with cellular encapsulation and are unable to create constructs containing an interconnected, user-defined porosity.[64-66]

In an effort to create hard constructs containing interconnected pores which would be capable of supporting cell-laden hydrogels, manufacturing techniques such as laser sintering and Fused Deposition Modeling (FDM) have been used.[67, 68] However, while these techniques are capable of creating constructs with interconnected pores, cellular encapsulation would need to occur after machining. Alternatively, photomasking and stereolithography techniques are capable of creating soft constructs containing interconnected pores, but do not address the issue of combining hard scaffolds with soft internal matrices.[1, 7, 69]

With the advent of commercial 3D printing, researchers are now capable of using additive manufacturing platforms to create both hard and soft scaffolds that mimic complex 3D geometries.[70, 71] Common materials used for bone tissue engineering scaffolding such as hydroxyapatite and polycaprolactone (PCL) are also now able to be transformed into custom made spools capable of being used with printers such as MakerBot.[72-74] More importantly, as 3D printing technology has continued to improve, printing hard scaffolds alongside encapsulated cells has become a reality. In one instance, 3D printing was used to print chondrocytes and bone marrow cells within alginate hydrogels supplemented with calcium phosphate and hydroxyapatite.[75] In another promising instance, a custom built six nozzle printer was used to print molten PCL alongside encapsulated human osteoblasts and chondrocytes in a construct containing porous spaces for nutrient diffusion.[76] However, despite these promising advances in the 3D printing of hard constructs containing encapsulated cells, the inability to develop perfusable microvascular networks within structures remains a major obstacle in preventing their widespread clinical use.

1.4.3 Challenge 3 – Adding perfusable vasculature

In native bone, perfusion of blood through defined vascular networks separated by only a few hundred microns guarantees effective nutrient supply, waste removal, and access of systemic signaling molecules to individual bone cells.[20, 41, 77] Accordingly, by mimicking this hierarchical perfusable vascular network within a bone substitute, clinical outcomes could be drastically improved by enhancing integration with surrounding host tissue, as well as by allowing the restoration of controlled blood flow to the site of the injury.[78, 79]

To mimic vascular physiology, integration of user defined channels within cell-laden hydrogels is a promising approach that would significantly advance tissue-engineering technologies.[80] However, in addition to the inherent manufacturing difficulties presented in the fabrication of user defined 3D channels, other issues such as material properties, fabrication times and processes, and cellular viability need to be taken into account.[81, 82]

Micro-fabrication techniques such as soft- and photolithography have been used to generate hollow microfluidic channels within both synthetic and naturally derived cell-laden hydrogels but, while such constructs have shown increased cellular viability while being perfused with media as compared to static controls, the fabrication of the 3D channels in user defined patterns is extremely difficult.[83-87] Other types of machining approaches involve methods such as needles[88, 89] and sacrificial/fugitive-molding[90] and rely on either needle extraction or the dissolution of sacrificial material in order to create hollow channels. Although these approaches are inexpensive and scalable, they are limited by the size of the needle or sacrificial template used.

Advances in 3D printing and additive manufacturing techniques provide an exciting avenue for the creation of structurally supportive constructs containing user defined vascular and osteo-competent cells. However, while there has been a significant amount of work in this area, a complete bone tissue engineering solution has yet to be achieved. In many instances, the combination of sacrificial 3D printed materials such as carbohydrates or pluronics within large cell-laden hydrogels has proven successful, but in each case the printed structure was very specific to the problem being explored and was either not suitable for bone tissue engineering or difficult to modify for different applications.[87, 90-92]

1.5 Scope of dissertation

The overarching goal of this work is to develop a comprehensive vascularized bone tissue implant to eventually serve as a viable *in vivo* therapy for a critically sized segmental bone defect. To advance that goal, this thesis focuses on the development of a bone tissue model consisting of user defined perfusable vascular networks within structurally reinforced hydrogels that are laden with osteoblast-like cells.

The introduction, Chapter 1, serves to present a basic view of the structure of bone and highlight challenges that must be addressed when developing a bone tissue engineered solution for critical bone defects. Chapter 2 aims to explore the first challenge identified in creating a bone tissue substitute and presents a study on how encapsulated osteoblast-like cells interact within a diffusion limited gelatin methacrylate hydrogel. Building upon Chapter 2, Chapter 3 investigates the second challenge and presents a study on 3D printed structural cages for cell laden hydrogels and explores how the structural cages can be combined with cell-laden hydrogels. Chapter 4 addresses the third identified challenge and focuses on how user defined vasculature can be added to a structurally supported cell-laden hydrogel to create a perfusable bone tissue construct. In Chapter 5, future directions and ongoing modifications to the current model presented in Chapter 4 are discussed.

1.6 References

1. Gibbs, D.M., et al., *Hope versus hype: what can additive manufacturing realistically offer trauma and orthopedic surgery?* Regenerative Medicine, 2014. **9**(4): p. 535-549.

2. Santos, M.I. and R.L. Reis, *Vascularization in bone tissue engineering: physiology, current strategies, major hurdles and future challenges*. Macromolecular Bioscience, 2010. **10**(1): p. 12-27.
3. Warnke, P., et al., *Growth and transplantation of a custom vascularised bone graft in a man*. The Lancet, 2004. **364**(9436): p. 766-770.
4. Laurencin, C., Y. Khan, and S.F. El-Amin, *Bone graft substitutes*. Expert Review of Medical Devices, 2006. **3**(1): p. 49-57.
5. Einhorn, T.A. and L.C. Gerstenfeld, *Fracture healing: mechanisms and interventions*. Nature Reviews Rheumatology, 2015. **11**(1): p. 45.
6. Pneumaticos, S.G., et al., *Segmental bone defects: from cellular and molecular pathways to the development of novel biological treatments*. Journal of Cellular and Molecular Medicine, 2010. **14**(11): p. 2561-2569.
7. Black, C.R., et al., *Bone tissue engineering*. Current Molecular Biology Reports, 2015. **1**(3): p. 132-140.
8. Kurien, T., R. Pearson, and B. Scammell, *Bone graft substitutes currently available in orthopaedic practice: the evidence for their use*. Bone Joint J, 2013. **95**(5): p. 583-597.
9. Rizzo, M. and S.L. Moran. *Vascularized bone grafts and their applications in the treatment of carpal pathology*. in *Seminars in plastic surgery*. 2008. Thieme Medical Publishers.
10. Scheufler, O., et al., *Spatial and temporal patterns of bone formation in ectopically pre-fabricated, autologous cell-based engineered bone flaps in rabbits*. Journal of Cellular and Molecular Medicine, 2008. **12**(4): p. 1238-1249.
11. Berrey Jr, B.H., et al., *Fractures of allografts. Frequency, treatment, and end-results*. JBJS, 1990. **72**(6): p. 825-833.
12. Basu, B., *Biomaterials for Musculoskeletal regeneration: concepts*. 2016: Springer.

13. Ilizarov, G.A., *Clinical application of the tension-stress effect for limb lengthening*. Clinical Orthopaedics and Related Research, 1990(250): p. 8-26.
14. Rachmiel, A. and D. Shilo, *The use of distraction osteogenesis in oral and maxillofacial surgery*. Annals of Maxillofacial Surgery, 2015. **5**(2): p. 146.
15. Healy, K. and R. Guldberg, *Bone tissue engineering*. Journal of Musculoskeletal and Neuronal Interactions, 2007. **7**(4): p. 328.
16. DiGiovanni, C.W., et al., *Recombinant human platelet-derived growth factor-BB and beta-tricalcium phosphate (rhPDGF-BB/ β -TCP): an alternative to autogenous bone graft*. JBJS, 2013. **95**(13): p. 1184-1192.
17. Guntur, A. and C. Rosen, *Bone as an endocrine organ*. Endocrine Practice, 2012. **18**(5): p. 758-762.
18. Teitelbaum, S.L., *Osteoclasts: what do they do and how do they do it?* The American Journal of Pathology, 2007. **170**(2): p. 427-435.
19. Jee, W., *Integrated bone tissue physiology: anatomy and physiology*. Bone Mechanics Handbook, 2001.
20. Buckwalter, J., et al., *Bone biology. Part I: structure, blood supply, cells, matrix, and mineralization*. JBJS, 1995. **77**(8): p. 1256-1275.
21. Basu, B., *Natural Bone and Tooth: Structure and Properties*, in *Biomaterials for Musculoskeletal Regeneration*. 2017, Springer. p. 45-85.
22. Baron, R., *Molecular mechanisms of bone resorption by the osteoclast*. The Anatomical Record, 1989. **224**(2): p. 317-324.
23. Jilka, R.L., *Biology of the basic multicellular unit and the pathophysiology of osteoporosis*. Pediatric Blood & Cancer, 2003. **41**(3): p. 182-185.

24. Parfitt, A., *Bone forming cells in clinical conditions*. Bone: A Treatise, The Osteoblast and Osteocyte., 1990. **1**: p. 351-429.
25. Buckwalter, J. and R. Cooper, *Bone structure and function*. Instructional Course Lectures, 1987. **36**: p. 27-48.
26. Triffitt, J.T., *The organic matrix of bone tissue*. Fundamental and Clinical Bone Physiology, 1980: p. 45-82.
27. Wall, J., S. Chatterji, and J. Jeffery, *The influence that bone density and the orientation and particle size of the mineral phase have on the mechanical properties of bone*. Journal of Bioengineering, 1978. **2**(6): p. 517-526.
28. Burr, D., *The contribution of the organic matrix to bone's material properties*. Bone, 2002. **31**(1): p. 8-11.
29. Lian, J., et al., *Induction of bone-related proteins, osteocalcin and osteopontin, and their matrix ultrastructural localization with development of chondrocyte hypertrophy in vitro*. Journal of Cellular Biochemistry, 1993. **52**(2): p. 206-219.
30. Shapses, S., et al., *Osteopontin facilitates bone resorption, decreasing bone mineral crystallinity and content during calcium deficiency*. Calcified Tissue International, 2003. **73**(1): p. 86-92.
31. Glimcher, M., *The nature of the mineral component of bone and the mechanism of calcification*. Instructional Course Lectures, 1987. **36**: p. 49-69.
32. Jensen, D.B., et al. *Bone Tissue: A Relationship Between Micro and Nano Structural Composition and its Corresponding Electrostatic Properties with Applications in Tissue Engineering*. in *Industry Applications Conference, 2007. 42nd IAS Annual Meeting. Conference Record of the 2007 IEEE*. 2007. IEEE.

33. Recker, R.R. and J. Barger-Lux, *Embryology, anatomy, and microstructure of bone. Disorders of Bone and Mineral Metabolism*. New York: Raven, 1992. **219**.
34. Marenzana, M. and T.R. Arnett, *The key role of the blood supply to bone*. Bone Research, 2013. **1**: p. 203-215.
35. Eliasson, P. and J.I. Jönsson, *The hematopoietic stem cell niche: low in oxygen but a nice place to be*. Journal of Cellular Physiology, 2010. **222**(1): p. 17-22.
36. Cooper, R.R., J.W. Milgram, and R.A. Robinson, *Morphology of the osteon: an electron microscopic study*. JBJS, 1966. **48**(7): p. 1239-1271.
37. Portal-Núñez, S., D. Lozano, and P. Esbrit, *Role of angiogenesis on bone formation*. Histology and Histopathology, 2012. **27**(4): p. 559.
38. Mikos, A.G., et al., *Prevascularization of porous biodegradable polymers*. Biotechnology and Bioengineering, 1993. **42**(6): p. 716-723.
39. Carano, R.A. and E.H. Filvaroff, *Angiogenesis and bone repair*. Drug Discovery Today, 2003. **8**(21): p. 980-989.
40. Wilson, A. and A. Trumpp, *Bone-marrow haematopoietic-stem-cell niches*. Nature Reviews Immunology, 2006. **6**(2): p. 93.
41. Laroche, M., *Intraosseous circulation from physiology to disease*. Joint Bone Spine, 2002. **69**(3): p. 262-269.
42. Kanczler, J. and R. Oreffo, *Osteogenesis and angiogenesis: the potential for engineering bone*. Eur Cell Mater, 2008. **15**(2): p. 100-114.
43. Chung, U.-i., et al., *Distinct osteogenic mechanisms of bones of distinct origins*. Journal of Orthopaedic Science, 2004. **9**(4): p. 410-414.
44. Kronenberg, H.M., *Developmental regulation of the growth plate*. Nature, 2003. **423**(6937): p. 332.

45. Glowacki, J., *Angiogenesis in fracture repair*. Clinical Orthopaedics and Related Research, 1998. **355**: p. S82-S89.
46. Stegen, S., N. van Gestel, and G. Carmeliet, *Bringing new life to damaged bone: the importance of angiogenesis in bone repair and regeneration*. Bone, 2015. **70**: p. 19-27.
47. Loi, F., et al., *Inflammation, fracture and bone repair*. Bone, 2016. **86**: p. 119-130.
48. Hutmacher, D.W., *Scaffold design and fabrication technologies for engineering tissues—state of the art and future perspectives*. Journal of Biomaterials Science, Polymer Edition, 2001. **12**(1): p. 107-124.
49. Burg, K.J., S. Porter, and J.F. Kellam, *Biomaterial developments for bone tissue engineering*. Biomaterials, 2000. **21**(23): p. 2347-2359.
50. Reichert, J.C. and D.W. Hutmacher, *Bone tissue engineering*, in *Tissue Engineering*. 2011, Springer. p. 431-456.
51. Bose, S., S. Vahabzadeh, and A. Bandyopadhyay, *Bone tissue engineering using 3D printing*. Materials Today, 2013. **16**(12): p. 496-504.
52. Stevens, M.M., *Biomaterials for bone tissue engineering*. Materials Today, 2008. **11**(5): p. 18-25.
53. Sladkova, M. and G.M. de Peppo, *Bioreactor systems for human bone tissue engineering*. Processes, 2014. **2**(2): p. 494-525.
54. Rice, J.J., et al., *Engineering the regenerative microenvironment with biomaterials*. Advanced Healthcare Materials, 2013. **2**(1): p. 57-71.
55. Cartmell, S.H., et al., *Effects of medium perfusion rate on cell-seeded three-dimensional bone constructs in vitro*. Tissue Engineering, 2003. **9**(6): p. 1197-1203.
56. Drury, J.L. and D.J. Mooney, *Hydrogels for tissue engineering: scaffold design variables and applications*. Biomaterials, 2003. **24**(24): p. 4337-4351.

57. Gauvin, R., et al., *Microfabrication of complex porous tissue engineering scaffolds using 3D projection stereolithography*. *Biomaterials*, 2012. **33**(15): p. 3824-3834.
58. Peppas, N.A., et al., *Hydrogels in biology and medicine: from molecular principles to bionanotechnology*. *Advanced Materials*, 2006. **18**(11): p. 1345-1360.
59. Slaughter, B.V., et al., *Hydrogels in regenerative medicine*. *Advanced Materials*, 2009. **21**(32-33): p. 3307-3329.
60. Van Den Bulcke, A.I., et al., *Structural and rheological properties of methacrylamide modified gelatin hydrogels*. *Biomacromolecules*, 2000. **1**(1): p. 31-38.
61. Nichol, J.W., et al., *Cell-laden microengineered gelatin methacrylate hydrogels*. *Biomaterials*, 2010. **31**(21): p. 5536-5544.
62. Xavier, J.R., et al., *Bioactive nanoengineered hydrogels for bone tissue engineering: a growth-factor-free approach*. *ACS Nano*, 2015. **9**(3): p. 3109-3118.
63. Bodugoz-Senturk, H., et al., *Poly (vinyl alcohol)–acrylamide hydrogels as load-bearing cartilage substitute*. *Biomaterials*, 2009. **30**(4): p. 589-596.
64. Chevalier, E., et al., *Fabrication of porous substrates: a review of processes using pore forming agents in the biomaterial field*. *Journal of Pharmaceutical Sciences*, 2008. **97**(3): p. 1135-1154.
65. Peltola, S.M., et al., *A review of rapid prototyping techniques for tissue engineering purposes*. *Annals of Medicine*, 2008. **40**(4): p. 268-280.
66. Billiet, T., et al., *A review of trends and limitations in hydrogel-rapid prototyping for tissue engineering*. *Biomaterials*, 2012. **33**(26): p. 6020-6041.
67. Williams, J.M., et al., *Bone tissue engineering using polycaprolactone scaffolds fabricated via selective laser sintering*. *Biomaterials*, 2005. **26**(23): p. 4817-4827.

68. Hutmacher, D.W., *Scaffolds in tissue engineering bone and cartilage*, in *The Biomaterials: Silver Jubilee Compendium*. 2006, Elsevier. p. 175-189.
69. Cooke, M.N., et al., *Use of stereolithography to manufacture critical-sized 3D biodegradable scaffolds for bone ingrowth*. *Journal of Biomedical Materials Research Part B: Applied Biomaterials*, 2003. **64**(2): p. 65-69.
70. Patrício, T., et al., *Fabrication and characterisation of PCL and PCL/PLA scaffolds for tissue engineering*. *Rapid Prototyping Journal*, 2014. **20**(2): p. 145-156.
71. Tuan, H.S. and D.W. Hutmacher, *Application of micro CT and computation modeling in bone tissue engineering*. *Computer-Aided Design*, 2005. **37**(11): p. 1151-1161.
72. Wei, C., et al., *High-precision flexible fabrication of tissue engineering scaffolds using distinct polymers*. *Biofabrication*, 2012. **4**(2): p. 025009.
73. Shor, L., et al., *Fabrication of three-dimensional polycaprolactone/hydroxyapatite tissue scaffolds and osteoblast-scaffold interactions in vitro*. *Biomaterials*, 2007. **28**(35): p. 5291-5297.
74. Swetha, M., et al., *Biocomposites containing natural polymers and hydroxyapatite for bone tissue engineering*. *International Journal of Biological Macromolecules*, 2010. **47**(1): p. 1-4.
75. Fedorovich, N.E., et al., *Biofabrication of osteochondral tissue equivalents by printing topologically defined, cell-laden hydrogel scaffolds*. *Tissue Engineering Part C: Methods*, 2011. **18**(1): p. 33-44.
76. Shim, J.-H., et al., *Bioprinting of a mechanically enhanced three-dimensional dual cell-laden construct for osteochondral tissue engineering using a multi-head tissue/organ building system*. *Journal of Micromechanics and Microengineering*, 2012. **22**(8): p. 085014.

77. McCarthy, I., *The physiology of bone blood flow: a review*. JBJS, 2006. **88**: p. 4-9.
78. Mercado-Pagán, Á.E., et al., *Vascularization in bone tissue engineering constructs*. Annals of Biomedical Engineering, 2015. **43**(3): p. 718-729.
79. Krishnan, L., N.J. Willett, and R.E. Guldborg, *Vascularization strategies for bone regeneration*. Annals of Biomedical Engineering, 2014. **42**(2): p. 432-444.
80. Annabi, N., et al., *Controlling the porosity and microarchitecture of hydrogels for tissue engineering*. Tissue Engineering Part B: Reviews, 2010. **16**(4): p. 371-383.
81. Bae, H., et al., *Building vascular networks*. Science Translational Medicine, 2012. **4**(160): p. 160ps23-160ps23.
82. Kaully, T., et al., *Vascularization—the conduit to viable engineered tissues*. Tissue Engineering Part B: Reviews, 2009. **15**(2): p. 159-169.
83. Zheng, Y., et al., *Microstructured templates for directed growth and vascularization of soft tissue in vivo*. Biomaterials, 2011. **32**(23): p. 5391-5401.
84. Golden, A.P. and J. Tien, *Fabrication of microfluidic hydrogels using molded gelatin as a sacrificial element*. Lab on a Chip, 2007. **7**(6): p. 720-725.
85. Zhao, L., et al., *The integration of 3-D cell printing and mesoscopic fluorescence molecular tomography of vascular constructs within thick hydrogel scaffolds*. Biomaterials, 2012. **33**(21): p. 5325-5332.
86. Zhang, Y., Y. Yu, and I.T. Ozbolat, *Direct bioprinting of vessel-like tubular microfluidic channels*. Journal of nanotechnology in engineering and medicine, 2013. **4**(2): p. 020902.
87. Bertassoni, L.E., et al., *Hydrogel bioprinted microchannel networks for vascularization of tissue engineering constructs*. Lab on a Chip, 2014. **14**(13): p. 2202-2211.
88. Chrobak, K.M., D.R. Potter, and J. Tien, *Formation of perfused, functional microvascular tubes in vitro*. Microvascular Research, 2006. **71**(3): p. 185-196.

89. Price, G.M., et al., *Effect of mechanical factors on the function of engineered human blood microvessels in microfluidic collagen gels*. *Biomaterials*, 2010. **31**(24): p. 6182-6189.
90. Miller, J.S., et al., *Rapid casting of patterned vascular networks for perfusable engineered three-dimensional tissues*. *Nature Materials*, 2012. **11**(9): p. 768.
91. Kolesky, D.B., et al., *Three-dimensional bioprinting of thick vascularized tissues*. *Proceedings of the National Academy of Sciences*, 2016. **113**(12): p. 3179-3184.
92. Byambaa, B., et al., *Bioprinted osteogenic and vasculogenic patterns for engineering 3D bone tissue*. *Advanced Healthcare Materials*, 2017. **6**(16).

CHAPTER 2: BEHAVIOR OF ENCAPSULATED SAOS-2 CELLS WITHIN GELATIN METHACRYLATE HYDROGELS^{Δ*}[1]

2.1 Abstract

The field of tissue engineering is still seeking a viable substitute to repair and replace damaged bone using a combination of porous implants, biochemical factors, and relevant cell types. While progress in this field has been made, current engineered solutions have not been able to mimic the architectural and biological requirements needed to provide a complete solution. In this work, osteoblast-like human osteosarcoma cells were encapsulated inside gelatin methacrylate (GelMA) hydrogels of three different weight/volume (w/v) concentrations and stimulated to form mineral in order to determine the relationship between both bone formation and cellular activity with matrix density. Distinct differences between cell morphology and mineral formation were found within the three types of hydrogels. Less dense, low w/v constructs were shown to provide a more cell friendly microenvironment that promoted dispersed mineral formation while dense, high w/v constructs provided a more structured environment for uniform bone-mineral formation. Additionally, while cells were able to function in all three types of hydrogels, cells in the less dense GelMA constructs were shown to grow in large colonies within the gelatin matrix while cells in the dense GelMA constructs tended to aggregate and grow along the construct peripheries.

^ΔAdapted from: Sawyer SW, Oest ME, Margulies BS, Soman P. (2016) Behavior of encapsulated saos-2 cells within gelatin methacrylate hydrogels. *Journal of Tissue Science & Engineering* 7(2):173.

* Reprinted as permitted by the open-access Creative Commons Attribution License

2.2 Introduction

Bone has emerged as the second most transplanted tissue in the world with forecasted revenue of \$6.6 billion by 2020 in the United States alone.[2, 3] While clinical grafts are used in many reparative orthopedic procedures, they often fail due to graft necrosis and lack of integration with host tissue.[4, 5] Due to the limited success of such grafts, numerous alternative solutions to repairing and regenerating bone have been proposed that consist of combinations of different types of porous osteoconductive biomaterials, osteoinductive growth factors, and osteogenic cells.[6-9] However, no single option has emerged as a complete engineered solution. When creating a proper bone tissue substitute, several variables need to be taken into account: the scale of the implant needs to be optimized for proper porosity and nutrient distribution, the base material must be biocompatible and biodegradable in ways that promote high cell viability and natural tissue growth, and the mechanical support of the implant should be suitable for proper weight bearing applications.[3, 8-12] Current tissue engineering strategies have not been able to address all of the aforementioned variables for an organ as intricate as bone. Traditionally, bone tissue engineering has adopted the strategy of creating scaffolds that provide structural support followed by the seeding of relevant cells onto the construct post-manufacturing. Although the exclusion of living cells during manufacturing gives the flexibility of using a variety of fabrication techniques needed to make intricate tissue substitutes, the cell seeding approach relies on the ability of cells to infiltrate the interiors of the 3D scaffold and often results in inadequate cell dispersion and cellular densities. To address this limitation, another manufacturing approach involving cell encapsulation within a soft biomaterial has also been widely explored. Cell encapsulation generally utilizes either synthetic or naturally derived hydrogels and includes the incorporation of living cells into a hydrated matrix during fabrication, thus allowing for the precise control over the cellular density and distribution within a soft 3D construct.[13-16]

Although cell encapsulation is an appealing approach for the incorporation of relevant cells and growth factors into a bone tissue substitute, several issues need to be addressed. Not only is it important to know how the hydrogel properties influence the viability and function of encapsulated osteoblastic cells, it is important to understand how soft hydrated matrices influence bone mineral formation. Furthermore, the soft cell-laden hydrogels need to be integrated within a protective, structural frame in order to realize the goal of developing a clinically relevant biomimetic construct for bone tissue engineering. In this current study, we focus on how encapsulated cells interact within the hydrated microenvironment of a soft bone tissue substitute. To this end, we encapsulate osteoblast-like human osteosarcoma cells (Saos-2) inside GelMA hydrogels of varying weight/volume (w/v) concentrations and stimulate them to form mineral in order to determine the relationship between bone formation and hydrogel density.

2.3 Materials and Methods

2.3.1 Gelatin methacrylate pre-polymer solution preparation

Gelatin methacrylate (GelMA) macromer was synthesized using a previously reported protocol to serve as the base hydrogel matrix for cellular encapsulation.[17, 18] Briefly, porcine skin gelatin (Sigma Aldrich) was mixed at 10% (w/v) in phosphate buffered saline (PBS, Thermo Fisher Scientific), stirred at 45°C, mixed with methacrylic anhydride, and stirred for 3 hours. After stirring, the solution was dialyzed against distilled water for one week at 40°C, freeze-dried, and stored at -80°C until needed. For cell encapsulation experiments, three different

GelMA pre-polymer solutions (7, 10 and 15% w/v) were created by combining the freeze-dried GelMA macromer with various amounts of PBS and 0.25% UV photoinitiator Irgacure 2959 (Specialty Chemicals, Switzerland). The pre-polymer solutions were sterile filtered and stored at 2°C in autoclaved Pyrex bottles (Corning) wrapped with tin foil. Pre-polymer solutions below 7% were not used as they were not capable of being photo-cured while pre-polymer solution above 15% were not capable of being properly dissolved and sterile filtered.

2.3.2 Saos-2 culture and encapsulation

We employed human osteosarcoma cells (Saos-2; ATCC) transfected with a commercially available green fluorescent protein (GFP) lentivirus (Santa Cruz Biotechnology) as analogues for osteoblasts since they are a robust cell line capable of being used in the initial stages of new bone defect models. The GFP tagged Saos-2 cells were cultured in Dulbecco's Modification of Eagle's Media (DMEM; Life Technologies) supplemented with 10% fetal bovine serum (v/v) (FBS lot G12102; Atlanta Biologicals), 1% penicillin-streptomycin (Life Technologies) and 1% GlutaMAX (Life Technologies). Cells were passaged using standardized protocols with 0.25% trypsin-EDTA (Life Technologies) and maintained at conditions of 37°C with 5% CO₂. Cells were encapsulated in GelMA matrices of varying densities by mixing 20µL of a stock cell solution containing approximately 3750 cells/µL with 130µL of 7%, 10%, or 15% GelMA pre-polymer solution (w/v). The cell/GelMA solution was pipetted drop-wise into 5mL of autoclaved vegetable oil and UV cured for 1 minute with an intensity of 5mW/cm² using a Hamamatsu LED Controller (Hamamatsu C11924-511; Hamamatsu Photonics K.K., Japan), taking advantage of an oil emersion based surface tension technique for cell encapsulation (**Fig. 2.1A**).[19] The solidified GelMA hydrogels containing encapsulated cells were then washed five

times with 5mL of sterile PBS, transferred into 2mL of supplemented DMEM, and cultured as previously reported. Media was exchanged on each construct every 2 to 3 days until being fixed with 2% paraformaldehyde (Sigma) in PBS.

2.3.3 Osteosarcoma mineralization

Saos-2 cells were encapsulated and cultured as previously mentioned for specific durations of time before being chemically stimulated to produce mineral. Specifically, Saos-2 cells were encapsulated at approximately 75,000 cells per construct and allowed to grow for either 7 days (for histological staining assays) or 2 weeks (for microCT) before being chemically stimulated with an induction media. The induction media consisted of DMEM containing 10% FBS and 1% PSG supplemented with 0.1 μ M dexamethasone (Sigma Aldrich), 25 μ g/mL L-ascorbic acid-2-phosphate (AA2P; Sigma Aldrich), and an increasing regiment of β -glycerophosphate (BGP; Sigma Aldrich).[20] The BGP regimen included one media change with 5mM BGP, followed by one media change with 10mM BGP, and all subsequent media changes containing 20mM BGP. Once the specific time points for each experiment were reached, the samples were fixed in a 2% paraformaldehyde solution and cryo-protected with a 30% sucrose solution for both micro-computed tomography imaging and sectioning.

2.3.4 Histochemical analysis, Live/Dead staining, and image processing

All encapsulated samples were fixed in a 2% formaldehyde solution. Chemically stimulated samples were cryo-protected with a 30% sucrose solution in PBS for both micro-computed tomography imaging and sectioning, while non-stimulated samples were cryo-protected using a

14% ethylenediaminetetraacetic acid (EDTA; Sigma) and 30% sucrose solution in PBS. Samples to be sectioned were embedded in Tissue Freezing Medium Blue (TFM™; Electron Microscopy Sciences), snap frozen using liquid nitrogen, and sectioned into 10µm slices using a Leica CM3050 cryostat (Leica Biosystems, Germany). Following sectioning, non-chemically stimulated samples to be stained for F-actin were treated with 0.1 M sodium citrate buffer solution pH 6.0, washed with PBS, and stained with Alexa Fluor 568 Phalloidin (1:100 dilution; Life Technologies). Nuclei were counterstained with 2.5 µg/mL 4', 6-diamidino-2-phenylindole (DAPI; Life Technologies) in PBS. Following sectioning, all chemically stimulated samples to be analyzed for mineral were stained with 40mM alizarin red S pH 4.2 (Sigma Aldrich) and counterstained with 2.5 µg/mL DAPI in PBS. The viability of cells was analyzed using a Live/Dead assay. To evaluate cell viability, all three different types of hydrogels containing encapsulated cells were placed in media containing calcein-AM (1:2000 dilution; Life Technologies) and ethidium homodimer (1:500 dilution; Life Technologies) after 5 days of growth and incubated at 37°C for 1 hour. Raw .tiff images were taken for all sectioned samples using an epifluorescence equipped Nikon Eclipse E-400 microscope (Nikon Corporation). All reported images were processed linearly for brightness and contrast using Adobe Photoshop CC 2015 (Adobe Systems Inc.). Once adjusted for brightness and contrast, images were converted to gray scale and subsequently overlaid to produce published images.

2.3.5 Micro-computed tomography

Chemically stimulated samples were fixed in a 2% formaldehyde solution and subsequently cryo-protected with a 30% sucrose solution for micro-computed tomography imaging and sectioning. A Scanco micro-CT 40 (Scanco Medical) was used to image and quantify mineral

formation in chemically stimulated samples. Samples were placed in groups of 3 inside gauze packed micro-CT canisters and kept hydrated with 2% formaldehyde solution during imaging. Samples were imaged at a 16 μm isotropic voxel resolution (55 kV, 145 mA, 200 ms integration time). After scanning, mineralized tissue volume (bone volume, BV) and density (BMD) were calculated by applying a lower global threshold (166 mg HA/cm³) to the image, which was digitally contoured.

2.3.6 Quantitative values and statistical analysis

All quantitative values, with the exception of micro-computed tomography values, were obtained using open-source ImageJ (NIH) software. Retrieved data was entered manually into Microsoft Excel (Microsoft Corporation) where values were reported as means \pm standard deviation. One-way ANOVA was performed using Microsoft Excel data pack. P-values < 0.05 were considered statistically significant.

2.4 Results

2.4.1 Formation of cell-laden hydrogels

In order to determine how osteoblast-like cells behaved while encapsulated within a soft gelatin matrix, 75,000 Saos-2 cells were mixed with three different concentrations of GelMA prepolymer solution (7%, 10%, and 15% w/v), pipetted into an oil bath to form hydrated beads, and UV cured for one minute (**Fig. 2.1A**). Free radicals released from the photoinitiator (Irgacure 2959) in the pre-polymer solution caused the covalent binding of acrylate groups during the UV

exposure, thereby crosslinking GelMA drops (~6mm x 6mm x 4mm) (**Fig. 2.1B**). This technique utilized the surface tension between aqueous GelMA solution and vegetable oil to crosslink GelMA drops at the air-GelMA-oil interface, and provided an easy-to-use approach with high degree of reproducibility.[19] A relatively low seeding density was used in order to maximize cell-matrix interactions within the three different types of hydrogels and the volume of the drops was specifically chosen to mimic murine bone defects.

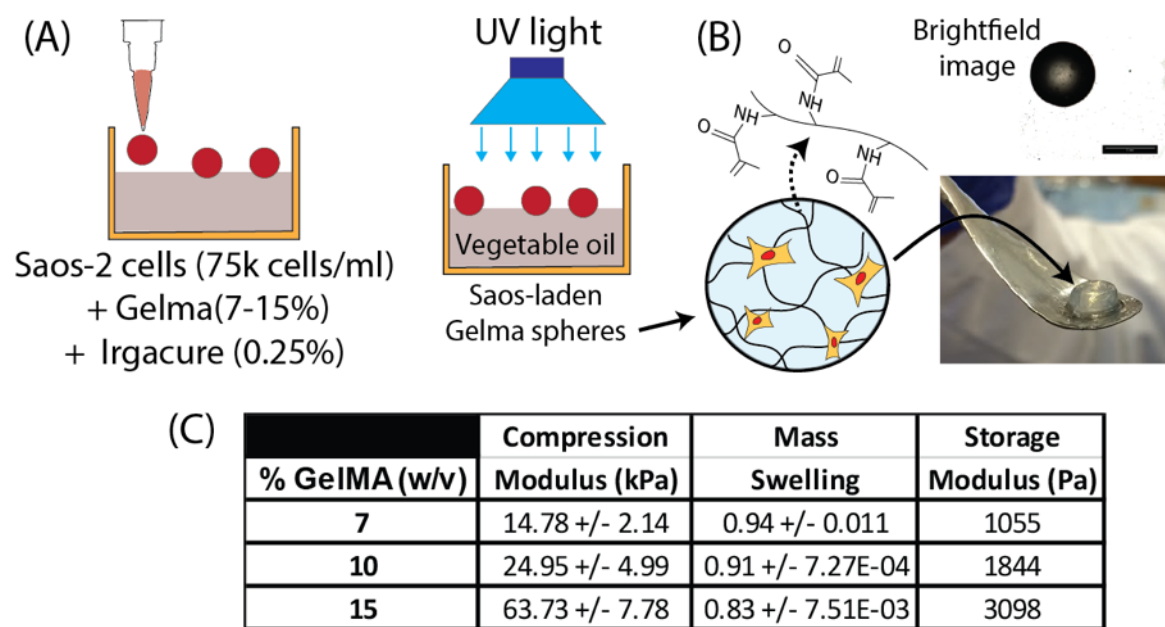


Figure 2.1: Cellular encapsulation schematic. (A) Schematic of surface tension encapsulation technique. 75,000 Saos-2 cells in 20 μ l aliquots were combined with 130 μ l of prepolymer solution containing .25% photoinitiator and pipetted dropwise into a bed of vegetable oil. UV light was cast onto the hydrogel drops for one minute to cure before being rinsed with PBS and transferred into incubation media. (B) Cured hydrogel spheres containing encapsulated cells resembled disc like structures with dimensions approaching 6mm x 6mm x 4mm (scale bar = 5mm). (C) Mechanical data of various GelMA (w/v) concentrations modified from previous work.[18]

2.4.2 Viability of encapsulated cells

The size of the hydrogel drop was designed to maximize cell-matrix interactions in a porous space that mimicked a murine bone defect. Viability was quantified 5 days after encapsulation using ethidium homodimer (dead cells = red staining) versus calcein-AM (live cells = green staining) (**Fig. 2.2A**). It was found that there was an apparent higher viability in the less dense 7% hydrogels with approximately 60% live as opposed to only 40% live in both the 10% and 15% gels. However, due to inherent diffusion limitations in constructs many millimeters in size, low cell viability was observed. In order to determine how cells behaved within the hydrogel matrices at various stages of growth, histological sectioning was performed. Accordingly, the GelMA drops were fixed in 2% paraformaldehyde and cryosectioned into 10 μm slices to allow for imaging. A specific region of interest (ROI) was chosen to standardize measurements between samples (**Fig. 2.2B**). The ROI used in all analysis was determined to be the area between the center of the sectioned slices and the corresponding slice periphery.

Due to expected nutrient diffusion limitations within the denser hydrogels, it was necessary to quantify cell number in the sectioned ROIs at specific time points to determine cell migration patterns. To analyze whether cells were forming colonies inside the bulk material or simply migrating out of the constructs, cells were counted in the ROIs for each of the three types of hydrogels at 3 day, 7 day and 14 day timepoints by staining fixed slices with DAPI (nuclei) (**Fig. 2.2C Left**). More cells were counted, on average, in the ROIs of the 7% gels at all timepoints and decreased as the gels became denser. For the 3 day time point, 19 cells on average were observed in the 7% constructs while only 12 cells were counted in the 15% constructs. Additionally, over time the number of cells within the ROI of the 7% gels increased at a higher

rate than those in the 15% gels, with 39 cells on average appearing in the 7% and only 17 cells appearing in the 15%. This represented an approximately 100% increase in the amount of cells in the ROI of the 7% gel with only a 41% increase in the 15% gel.

Cells encapsulated within GelMA spheres were transfected with GFP in order to determine spatial cell location inside the scaffolds prior to fixation, as well as inherent cellular activity at all stages of growth. At each specified timepoint, fixed and sectioned samples were imaged for green emissions to ensure that counted cells were still active. In addition to the standard 3 day, 7 day, and 14 day time points, cells were imaged inside of the ROIs well over 1 month after the initial photocuring to show long term activity (**Fig. 2.2C Right**).

As a result of GelMA autofluorescence when exposed to UV light after cell nuclei were stained with DAPI, construct degradation of all three types of hydrogels could be measured. Constructs were fixed and stained with DAPI at 3 day, 14 day and 49 day time points in order to determine if a quantifiable relationship existed between bulk matrix degradation and hydrogel density (**Fig. 2.2D**). In general, the less dense hydrogels showed higher porosities (defined as void area fraction within a 10 μ m slice) than denser hydrogels at all time points. Compared to the dense 15% hydrogels, 7% gels were 4% more porous at 3 days, 7% more porous at 14 days and 16% more porous at 49 days. Additionally, it was shown that denser gels degraded slower over time, with 7% gels increasing in porosity by 21% from 3 to 49 days, compared to an 11% increase in 10% gels and a 9% increase in 15% gels.

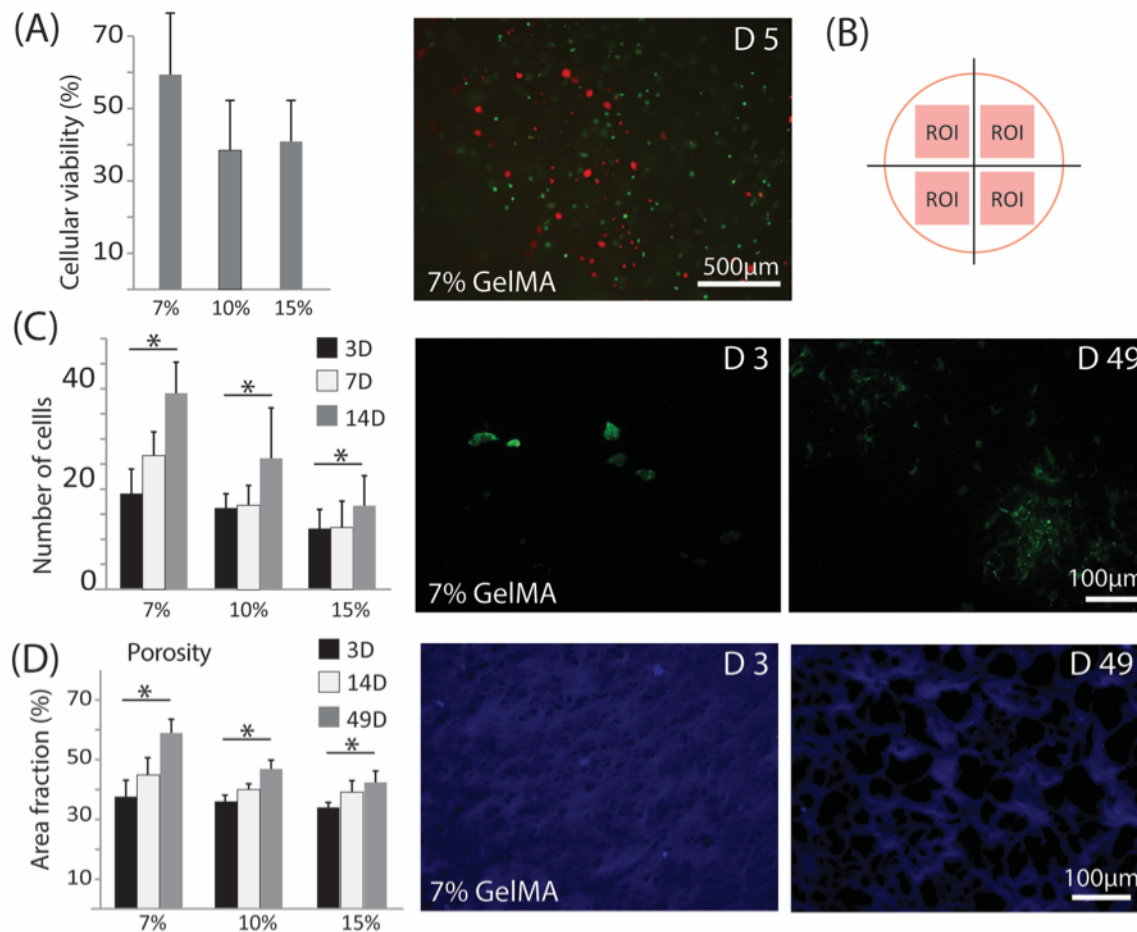


Figure 2.2: Cellular viability and activity within degradable hydrogel scaffolds of different stiffness. (A) Cells were grown within hydrogel constructs for 5 days and analyzed for cellular viability using calcein-AM (live = green) and ethidium homodimer (dead = red). Fluorescent images of live/dead cells show live and dead cells throughout the entire scaffold. (B) Representative schematic of the region of interest used to standardize measurements between fixed and sectioned histological samples. Areas between the center of the slices and the peripheries were used due to sectioning artifacts. (C) Cells stained with DAPI were counted in the ROI of histological slices for 3 day, 7 day, and 14 day timepoints. Increases in cellular population over time within the hydrogels were evident in all samples at all timepoints ($n = 3$; $* = p < 0.05$). (D) Saos-2 cells tagged with green fluorescent protein (GFP) appeared in all

samples well over one month after encapsulation (scale bar = 100 μ m). **(D)** Fluorescence in histological samples due to DAPI staining allowed for apparent porosity of hydrogels containing encapsulated cells to be measured for 3 day, 14 day and 49 day timepoints. Blue coloring represents GelMA staining while black coloring represents apparent void space. All gels degraded significantly over time (n = 3; * = p < 0.05; scale bar = 100 μ m).

2.4.3 Cellular morphology

In addition to showing cell migratory differences throughout the three different hydrogel constructs, cell morphology was cataloged at different time points to determine if matrix density had an effect on cellular growth. Cell morphology was determined in the ROI for each of the three types of gels at 3 day, 7 day, and 14 day time-points by staining fixed construct slices with DAPI (nuclei) and phalloidin (F-actin). At early timepoints, cell morphology appeared similar in the 7%, 10% and 15% gels, but changed dramatically at the later timepoints. At later timepoints, cells within the ROI in the less dense gels formed large, defined clusters while cells in the 10% and 15% gels formed either limited or no clusters. Representative images of each type of construct indicate significant differences between cellular aggregations and morphology between the 7%, 10%, and 15% samples (**Fig. 2.3A Top**). This observation is evident in the high-resolution photographs at the 14D timepoint (**Fig. 2.3A Bottom**).

The aggregate nucleus diameter and area of encapsulated cells, as well as the aggregate lacunae diameter and area of encapsulated cells, were quantified in order to highlight the differences between how cell colonies grew within the bulk matrix of the three different hydrogels (**Fig. 2.3B**). The aggregate area and diameter of nuclei stained with DAPI were rather consistent for all

different gels at each of the three timepoints, except for numerous large clusters of nuclei that were predominately observed in the 7% gels after 14 days of culture. Synonymously, the aggregate lacunae area and diameter were similar in all scaffolds at each stage of growth except for the large clusters of cells that formed intricate lacunae after 14 days in the soft 7% gels.

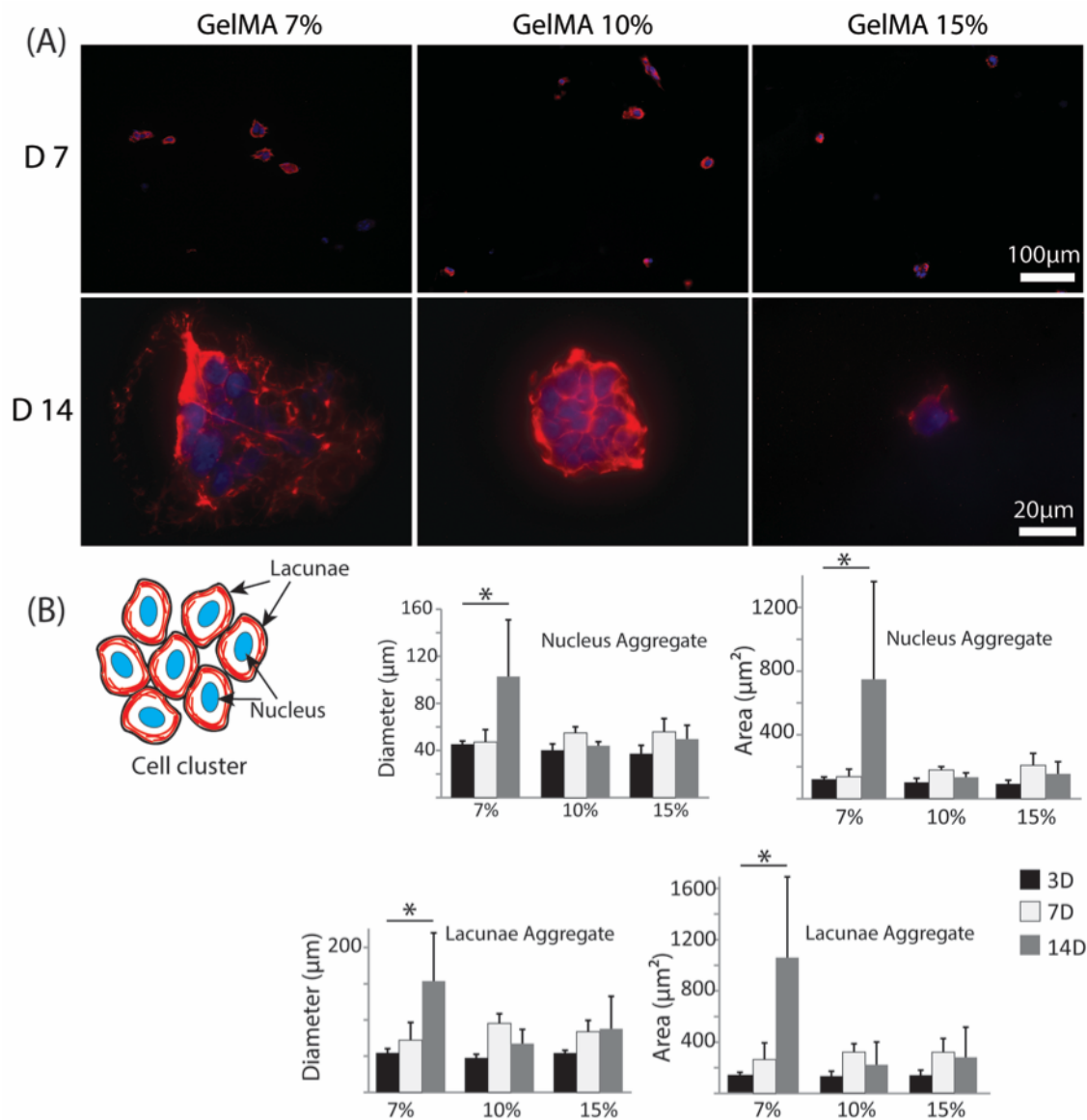


Figure 2.3: Nuclear and cytoskeleton staining of encapsulated Saos-2 cells. (A) Cells were grown within hydrogel constructs for either 3, 7, or 14 days, fixed, sectioned, and stained for f-actin (red = phalloidin) and counterstained for nuclei (blue = DAPI). Representative pictures at

7 days (scale bar = 100 μ m) and 14 days (high resolution; scale bar = 20 μ m) show distinct morphological differences in the ROI of samples of different densities at all timepoints. **(B)** Histological samples stained with phalloidin and counterstained with DAPI were analyzed for morphological differences in the nuclei and lacunae at 3 day, 7 day, and 14 day timepoints. Measurements showed significant differences in aggregate nuclear diameters and areas, as well as aggregate lacunae diameters and areas, for softer hydrogels over time (n = 3; * = p < 0.05).

2.4.4 Mineral deposition

To better examine the potential effects of matrix stiffness on osteogenesis, Alizarin red S staining was used to identify the presence of deposited calcium in chemically stimulated hydrogels. Cells were stimulated to produce mineral 7 days after encapsulation and were subsequently grown for an additional 2 weeks in osteogenic media in order to determine what effect hydrogel density had on bone nodule formation. Alizarin red and DAPI counterstain were used to visualize fixed samples for mineral **(Fig. 2.4A)**, and mineral content and mineral area within the ROI was quantified **(Fig. 2.4C)**. Consistent with previous results, the total area fraction of mineral within the ROI was greater by 3-fold in the ROI of 7% gels than in the dense 15% gels, while mineral clusters in the ROI of less-dense hydrogels had areas 3.5-fold greater than those in 15% gels.

A different group of samples were grown for 2 weeks in order to mimic the 14-day culture period used in the cellular morphology studies and were subsequently stimulated in osteogenic media for an additional 14 days. After four weeks, samples were fixed and scanned via microCT to determine total bone mineral content **(Fig. 2.4B, C)**. 7% hydrogels showed indiscrete mineral

formation throughout the entire construct while 15% gels showed concentrated mineral formation at the peripheries. Total mineral content appeared to be similar in both the 7% and 15% samples with 0.053 mg HA and 0.058 mg HA respectively.

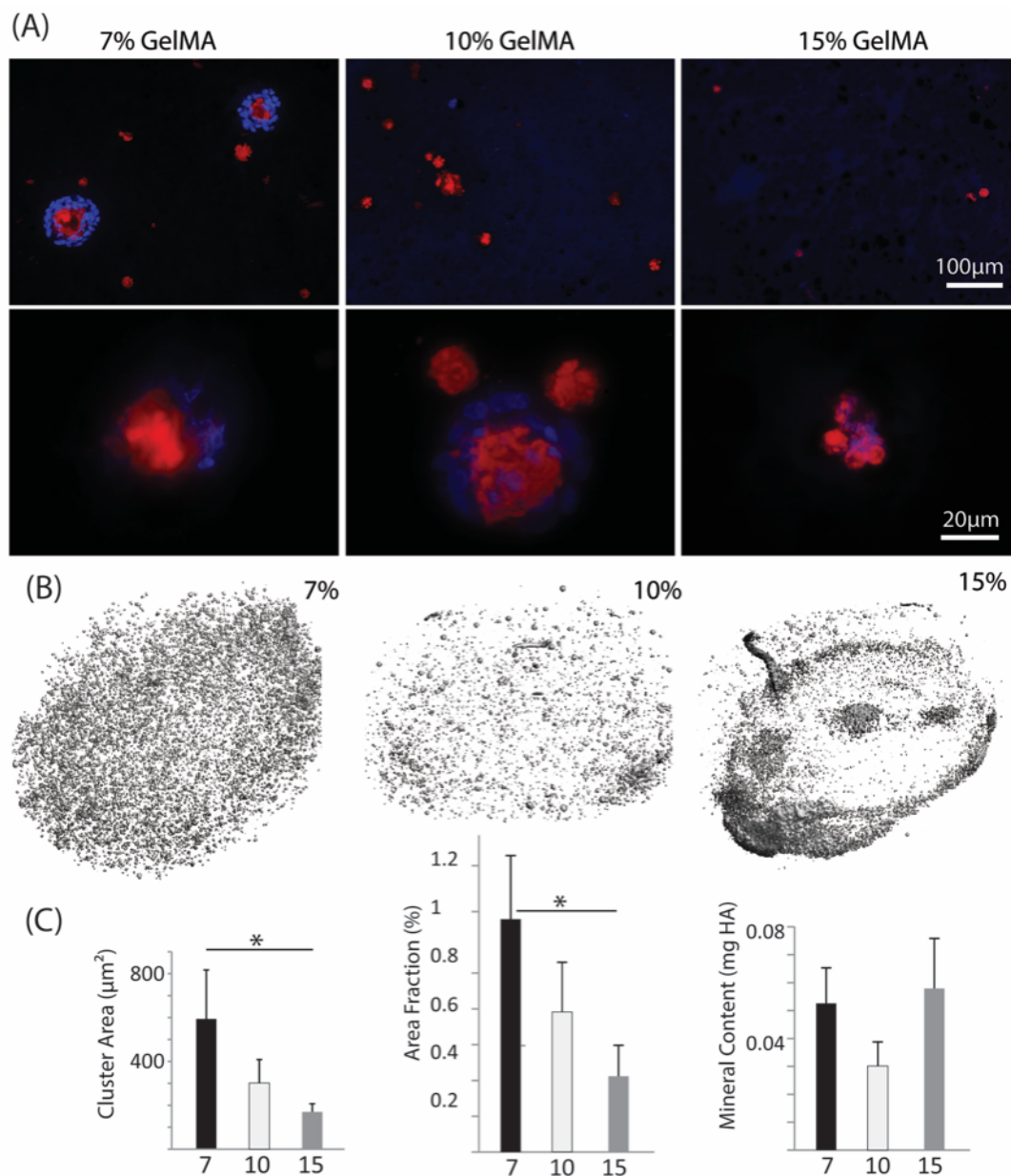


Figure 2.4: Mineralization and microCT of encapsulated Saos-2 cells. (A) Cells were grown within hydrogel constructs for 7 days and were subsequently placed in osteogenic media for an additional 14 days. Constructs were fixed, sectioned, stained for mineral deposition (red =

alizarin red S) and counterstained for nuclei (blue = DAPI). Representative pictures for all samples show distinct difference in the mineral located within the ROI for different gel densities (top scale bar = 100 μ m; bottom scale bar = 20 μ m). **(B)** Cells were grown within hydrogel constructs for 14 days and were subsequently placed in osteogenic media for an additional 14 days. Samples were analyzed via microCT for total mineral within the constructs of different stiffnesses. **(C)** Histological samples stained with alizarin red S and counterstained with DAPI were analyzed for mineral cluster area and area fraction of mineral coverage within the ROI and showed significant differences for hydrogels of varying density ($n = 2$; $* = p < 0.05$). MicroCT scans were analyzed for total mineral throughout the constructs and showed no significant differences between hydrogels of varying density ($n = 3$).

2.5 Discussion

As compared to conventional studies performed on non-physiological 2-D substrates, Saos-2-laden GelMA hydrogels provide a more realistic 3-D environment with which to study bone regeneration.[21, 22] Although human osteosarcoma Saos-2 cells do not completely represent the response of primary human osteoblasts, Saos-2 do serve as a robust, model cell line capable of allowing for the assessment of the biocompatibility and differentiating potential of the GelMA matrix. As such, the results from this work indicate that the density of GelMA plays a vital role in encapsulated cell viability, morphology, and function.

UV crosslinking of photopolymers have several advantages over both chemical and ionic (physical) crosslinking strategies. UV crosslinking allows for easy tuning of material properties, eliminates the need for organic solvents, and provides short reaction times. One recent study

reported the encapsulation of human mesenchymal stem cells within a synthetic hydrogel containing Irgacure 2959 photoinitiator and demonstrated excellent cellular viability 14 days after UV crosslinking for varying curing times.[23] Specifically, UV light (100 W/365 nm) was exposed to hMSC-laden hydrogels for times varying between 2.5 minutes and 10 minutes, and DNA damage was not detected when exposure time was kept around 2.5 minutes. Other studies, which used similar UV crosslinking techniques for 2-3 minutes, also demonstrated no significant changes or damage to the cells as a result of UV exposure.[24] In our study, we only use an exposure time of 1 minute, much lower than the reported times causing observable DNA damage.

Recent work with UV-crosslinkable hydrogels containing living cells has shown success in an *in vivo* setting. Specifically, N-methacryloyl chitosan hydrogels mixed with living cells was demonstrated to undergo rapid transdermal crosslinking *in vivo* within 60 s through minimally invasive clinical surgery. Histological analysis revealed that low-dose UV irradiation did not induce skin injury and the acute inflammatory response disappeared after only 7 days.[25] Another study showed that encapsulated bone marrow-derived mesenchymal stem cells in UV crosslinked GelMA hydrogels demonstrated enhanced osteogenesis *in vivo* with significant mineralization.[26] In yet another study, GelMA hydrogels containing multipotent stromal cells within an ectopic rat model was used to engineer endochondral bone.[27]

As mentioned previously, low cellular viability of encapsulated osteosarcomas was expected since cells are required to be within 200-300 μ m of a nutrient supply in order to properly function *in vivo*. Due to the larger size of our cell-laden hydrogels and inherent diffusion limitations associated with dense constructs, viabilities ranging from 40 to 60 percent were normal. In a

similar study, Saos-2 cells were encapsulated within sodium-alginate drops of only 1mm in diameter and were found to survive at higher rates as compared to the GelMA drops used in this study, further emphasizing the role media diffusion plays in maintaining high levels of cellular viability.[28]

The observed cell count differences in the ROIs of the three different gels suggested that cells were migrating outside of the denser constructs due to poor nutrient diffusion. This result was in line with a recent study where it was shown that the cellular viability of encapsulated mesenchymal stem cells (MSCs) inside the matrix of porous gelatin constructs increased as porosity increased.[29] Additionally, the observation that cells within the ROIs of the more porous matrices were able to form larger clusters further suggested that cells within the less dense gels remained active in the bulk material while cells in the dense gels migrated towards the peripheries. Furthermore, the ability of cells within the 7% and 10% hydrogels to form defined cell colonies was consistent with existing literature detailing how cells behave while encapsulated in soft material. One recent study used sub-millimeter sized beads to encapsulate MG-63 osteosarcoma cells within gelatin-modified alginate (AlGel) hydrogels[30] and showed that the clusters of cells that formed within the AlGel had several protrusions with lengths of approximately 30 μ m extending between colonies. Similar phenomena have also been observed within encapsulated hematopoietic stem cells[31] and human embryonic stem cells.[32]

In this work, we used GelMA, a collagen derivative, as our soft component since it has tailorable mechanical properties, is able to be chemically modified with various peptides, is biodegradable, and has crosslinked environments similar to the natural extracellular matrix (ECM). Although dense GelMA matrices showed less mineralization near the center of the construct, cells were

still metabolically active and capable of surviving. Additionally, since there were no significant differences between the amounts of mineral produced in the 7% constructs versus the 15% constructs, it could be suggested that the encapsulated cells in the denser scaffolds migrated towards the periphery in order to uniformly encase the structure. Furthermore, although the levels of BGP used in the osteogenic media far exceeded reported physiological levels[33, 34], indiscriminate mineralization was not observed in acellular controls, suggesting that all mineral observed was cell mediated. Based on these observations, it is plausible to suggest that properly vascularized hydrogels of increased density could encourage osteogenic cells to create mineral in a consistent, ordered fashion.

2.6 Conclusions

This work showcases the advantages of using a gelatin-based porous hydrogel for bone tissue engineering. By understanding how the osteoblast-like cells function within hydrogels of different densities, it may be possible to capitalize on this knowledge and design more complex structures capable of directed bone formation. Specifically, going forward the denser hydrogels used in this study will be the base material for future work due to the robust mineral formation at the hydrogel peripheries.

2.7 Non-Author Acknowledgements

We would like to thank Shihao Yang for his assistance in synthesizing GelMA macromer and analyzing data, as well as Sean DeBoyace for his help in culturing cells. This work was

supported by the Soft Interfaces Integrative Graduate Education and Research Traineeship (IGERT) at Syracuse University and funded by the National Science Foundation (NSF).

2.8 Disclosure statement

There are no competing financial interests pertaining to this work.

2.9 References

1. Sawyer, S., et al., *Behavior of encapsulated saos-2 cells within gelatin methacrylate hydrogels*. J Tissue Sci Eng, 2016. **7**(173): p. 2.
2. Liu, Y., J. Lim, and S.-H. Teoh, *Review: development of clinically relevant scaffolds for vascularised bone tissue engineering*. Biotechnology Advances, 2013. **31**(5): p. 688-705.
3. Amini, A.R., C.T. Laurencin, and S.P. Nukavarapu, *Bone tissue engineering: recent advances and challenges*. Critical Reviews™ in Biomedical Engineering, 2012. **40**(5).
4. Eastlack, R.K., et al., *Osteocel Plus Cellular Allograft in Anterior Cervical Discectomy and Fusion: Evaluation of Clinical and Radiographic Outcomes From a Prospective Multicenter Study*. Spine, 2014. **39**(22): p. E1331-E1337.
5. Deyo, R.A., et al., *Use of bone morphogenetic proteins in spinal fusion surgery for older adults with lumbar stenosis: trends, complications, repeat surgery, and charges*. Spine, 2012. **37**(3): p. 222.
6. Griffith, L.G. and G. Naughton, *Tissue Engineering--Current Challenges and Expanding Opportunities*. Science, 2002. **295**(5557): p. 1009-1014.

7. Loh, Q.L. and C. Choong, *Three-dimensional scaffolds for tissue engineering applications: Role of porosity and pore size*. *Tissue Engineering Part B: Reviews*, 2013. **19**(6): p. 485-502.
8. Burg, K.J., S. Porter, and J.F. Kellam, *Biomaterial developments for bone tissue engineering*. *Biomaterials*, 2000. **21**(23): p. 2347-2359.
9. Reichert, J.C. and D.W. Hutmacher, *Bone tissue engineering*, in *Tissue Engineering*. 2011, Springer. p. 431-456.
10. Bose, S., S. Vahabzadeh, and A. Bandyopadhyay, *Bone tissue engineering using 3D printing*. *Materials Today*, 2013. **16**(12): p. 496-504.
11. Stevens, M.M., *Biomaterials for bone tissue engineering*. *Materials Today*, 2008. **11**(5): p. 18-25.
12. Hutmacher, D.W., *Scaffold design and fabrication technologies for engineering tissues—state of the art and future perspectives*. *Journal of Biomaterials Science, Polymer Edition*, 2001. **12**(1): p. 107-124.
13. Annabi, N., et al., *25th Anniversary Article: Rational design and applications of hydrogels in regenerative medicine*. *Advanced Materials*, 2014. **26**(1): p. 85-124.
14. Schuurman, W., et al., *Gelatin-Methacrylamide Hydrogels as Potential Biomaterials for Fabrication of Tissue-Engineered Cartilage Constructs*. *Macromolecular Bioscience*, 2013. **13**(5): p. 551-561.
15. Lewis, K.J. and K.S. Anseth, *Hydrogel scaffolds to study cell biology in four dimensions*. *MRS Bulletin*, 2013. **38**(03): p. 260-268.
16. Peppas, N.A., et al., *Hydrogels in biology and medicine: from molecular principles to bionanotechnology*. *Advanced Materials*, 2006. **18**(11): p. 1345-1360.

17. Wu, Y., et al., *Fabrication of conductive gelatin methacrylate–polyaniline hydrogels*. *Acta Biomaterialia*, 2016. **33**: p. 122-130.
18. Chen, Y.X., et al., *A Novel Suspended Hydrogel Membrane Platform for Cell Culture*. *Journal of Nanotechnology in Engineering and Medicine*, 2015. **6**(2): p. 021002.
19. Pradhan, S., C.S. Chaudhury, and E.A. Lipke, *Dual-phase, surface tension-based fabrication method for generation of tumor millibeads*. *Langmuir*, 2014. **30**(13): p. 3817-3825.
20. Thakur, N.A., S.D. DeBoyace, and B.S. Margulies, *Antagonism of the Met5-enkephalin-opioid growth factor receptor-signaling axis promotes MSC to differentiate into osteoblasts*. *Journal of Orthopaedic Research*, 2015. **34**(7): p. 1195-1205.
21. Saldaña, L., et al., *In search of representative models of human bone-forming cells for cytocompatibility studies*. *Acta Biomaterialia*, 2011. **7**(12): p. 4210-4221.
22. Ayobian-Markazi, N., T. Fouroutan, and M.J. Kharazifar, *Comparison of cell viability and morphology of a human osteoblastlike cell line (SaOS-2) seeded on various bone substitute materials: An in vitro study*. *Dental Research Journal*, 2012. **9**(1).
23. Kumar, D., et al., *Three-dimensional hypoxic culture of human mesenchymal stem cells encapsulated in a photocurable, biodegradable polymer hydrogel: a potential injectable cellular product for nucleus pulposus regeneration*. *Acta Biomaterialia*, 2014. **10**(8): p. 3463-3474.
24. Chung, C., et al., *Influence of gel properties on neocartilage formation by auricular chondrocytes photoencapsulated in hyaluronic acid networks*. *Journal of Biomedical Materials Research Part A*, 2006. **77**(3): p. 518-525.

25. Li, B., et al., *Hydrosoluble, UV-crosslinkable and injectable chitosan for patterned cell-laden microgel and rapid transdermal curing hydrogel in vivo*. *Acta Biomaterialia*, 2015. **22**: p. 59-69.
26. Zhao, X., et al., *Injectable Stem Cell-Laden Photocrosslinkable Microspheres Fabricated Using Microfluidics for Rapid Generation of Osteogenic Tissue Constructs*. *Advanced Functional Materials*, 2016. **26**(17): p. 2809-2819.
27. Visser, J., et al., *Endochondral bone formation in gelatin methacrylamide hydrogel with embedded cartilage-derived matrix particles*. *Biomaterials*, 2015. **37**: p. 174-182.
28. Schloßmacher, U., et al., *Alginate/silica composite hydrogel as a potential morphogenetically active scaffold for three-dimensional tissue engineering*. *RSC Advances*, 2013. **3**(28): p. 11185-11194.
29. Wang, L., et al., *Fabrication of Cell-Laden Macroporous Biodegradable Hydrogels with Tunable Porosities and Pore Sizes*. *Tissue Engineering Part C: Methods*, 2014. **21**(3): p. 263-273.
30. Grigore, A., et al., *Behavior of encapsulated MG-63 cells in RGD and gelatine-modified alginate hydrogels*. *Tissue Engineering Part A*, 2014. **20**(15-16): p. 2140-2150.
31. Yuan, Y., et al., *Ex vivo amplification of human hematopoietic stem and progenitor cells in an alginate three-dimensional culture system*. *International Journal of Laboratory Hematology*, 2011. **33**(5): p. 516-525.
32. Chayosumrit, M., B. Tuch, and K. Sidhu, *Alginate microcapsule for propagation and directed differentiation of hESCs to definitive endoderm*. *Biomaterials*, 2010. **31**(3): p. 505-514.
33. Boyan, B., et al., *Osteoblast-mediated mineral deposition in culture is dependent on surface microtopography*. *Calcified Tissue International*, 2002. **71**(6): p. 519-529.

34. Bonewald, L., et al., *von Kossa staining alone is not sufficient to confirm that mineralization in vitro represents bone formation*. *Calcified Tissue International*, 2003. **72**(5): p. 537-547.

CHAPTER 3: DEVELOPING 3D SCAFFOLDS IN THE FIELD OF TISSUE ENGINEERING TO TREAT COMPLEX BONE DEFECTS^{Δ*}[1]

3.1 Abstract

Polymers have been extensively used to develop 3D scaffolds in the field of tissue engineering and consist of certain design requirements such as biocompatibility, structural properties, and varying porosity inside of complex geometries, all with the ultimate goal of incorporating living cells within the scaffold structure. In this work, we present the synthesis and material characterization of hybrid spools using polycaprolactone (PCL) as the base polymer. We demonstrate that a commercial 3D Fused Deposition Modelling printer such as Makerbot can be used to print 3D scaffolds using three types of polymer spools: PCL, PCL-poly lactic acid (PLA) and PCL-hydroxyapatite (HA). Data derived from computerized tomography can be used to develop hollow porous cages using PCL. Lastly, we demonstrate that log-pile scaffolds are capable of being infused with a mixture of living cells and gelatin hydrogel. This work could be potentially useful in the treatment of patients with complex bone defects.

^Δ Adapted from: Albrecht LD, Sawyer SW, Soman P. (2016) Developing 3D scaffolds in the field of tissue engineering to treat complex bone defects. *3D Printing and Additive Manufacturing* 3(2):106-12.

* Reprinted as permitted by Mary Ann Liebert, Inc. author agreement for personal reuse.

3.2 Introduction

Bone has emerged as the second most transplanted tissue in the world as a result of patient traumas, aging populations, osteoporosis, and bone tumors.[2] Since current clinical therapies have not been sufficiently successful, the field of bone tissue engineering continues to develop new bone substitutes by combining porous biomaterial scaffolds with relevant cells, growth factors and other stimuli. Important aspects of bone tissue engineering include the fabrication of porous polymer scaffolds with patient-specific geometries, the necessary structural strength to house living cells, and the ability to facilitate tissue ingrowth during *in vitro* development of bone tissue or during *in vivo* implantation.[3-7]

To promote cell proliferation, tissue growth, and remodeling, porous scaffolds have been developed using several different manufacturing approaches. Use of traditional fabrication methods such as solvent casting, freeze drying, porogen leaching, fiber bonding, dual phase separation, and gas foaming typically create simple geometries and only allow limited control over pore-interconnectivity within 3D scaffolds, both of which are extremely essential for bone tissue applications.[8-10] With the goal of developing scaffolds with a 100% pore-interconnectivity, additive manufacturing and other solid free form fabrication (SFF) techniques such as laser sintering[11], stereolithography[12], and Fused Deposition Modelling (FDM) [4, 13] have been used.[6, 7] Several researchers have developed manufacturing equipment based on FDM principles where a polymer spool is extruded through a heated nozzle and can subsequently be moved using commands obtained from a computer-aided manufacturing program.[13, 14]

While most labs have typically developed custom made extrusion-based equipment to print user-defined 3D scaffolds, the emergence of easy-to-use commercial 3D printers have allowed other

researchers with non-manufacturing backgrounds to print complex 3D models. For example, physicians use Makerbot printers to develop anatomically accurate physical models for educational purposes and practice surgeries. The drawback, however, is that these physical models can be only built using commercially available and easy-to-use polymer spools. Certain types of biomaterial spools such as polycaprolactone (PCL), a thermoplastic commonly used for bone tissue engineering applications,[15] are not commercially available and have to be custom-made in research labs. Furthermore, these direct-writing techniques that rely on the properties of non-commercial colloidal biomaterial inks capable of being printed as droplets, hot-melts, or continuous filament lines [16-20] need specialized manufacturing knowledge to operate them. Moreover, incorporation of living cells within 3D printed scaffolds is yet another significant challenge and cells seeded on scaffolds with small pore-sizes could result in uneven cellular distribution throughout the scaffold.

In this work we demonstrate the synthesis and fabrication of 3D scaffolds using hybrid polycaprolactone (PCL) spools using an easy-to-use commercial Makerbot 3D printer. Hybrid spools were developed by mixing commercially available fillers such as poly-l-lactic-acid (PLA) or hydroxyapatite (HA) particles within the PCL matrix, following which mechanical and materials properties were characterized. We also demonstrate the incorporation of living cells into the interior of the log-pile scaffold with a facile and easy-to-use technique.

3.3 Materials and Methods

3.3.1 Development of hybrid spools

Spools were made using a Randcastle microfilament extruder (Randcastle Inc.) and a base material of polycaprolactone (PCL) pellets having a 3mm diameter and 70kDa-90kDa molecular weight (Sigma Aldrich) (**Fig. 3.1A**). The raw PCL material and the fillers, either hydroxyapatite (HA) (Sigma Aldrich) or poly-l-lactic-acid (PLA) were mixed and fed into the extruder hopper. The shear force of the machine's extrusion screw fed the raw material (PCL) and filler (either PLA or HA) into the four heating zones, allowing for homogenization of PCL-PLA composites and mixing of PCL-HA composites. A cooling zone was located below the third heating zone and the thread of the screw was reversed, thereby causing a buildup of pressure that forced the melted polymer mixture out of the head (heating zone 4). The temperatures were kept at 160° Fahrenheit (72° Celsius), just above 140° Fahrenheit (F) or 60° Celsius (C), which was the melting point for PCL, for the pure PCL spool in order to keep the polymer in liquid state during the extrusion process and maintain constant pressure. For the PCL-HA spool the temperatures were raised to 170°F (76.6°C) in order to allow HA powder to mix with liquid PCL, and for the PCL-PLA spool the temperatures were raised to 320°F (160°C) in order to melt both of the polymers since PLA has a melting point between 300°-320°F. The pressure for each spool was kept at 1000 psi +/- 200 psi and fed through a custom nozzle with an opening diameter of 1.57mm. The filament expanded once it left the extruder head to the appropriate 1.75 +/- 0.05mm so that it could be wound into spools and fed into the commercially available 3D printer, Makerbot Replicator 2 (Makerbot Industries) (**Fig. 3.1B**).

3.3.2 Chemical composition and testing

To determine the final material composition post extrusion and printing, a high resolution thermogravimetric analysis (TGA) was performed on PCL, PCL-HA and PCL-PLA samples using a Q500 thermogravimetric analysis (TA Instruments). The TGA heated spool samples to and beyond their degradation points while weighing them so that the amounts of each polymer/component could be determined based on weight percentages.

3.3.3 3D printing and mechanical testing

Spools were loaded into the Makerbot and both Solidworks (Dassult Systems) and Meshmixer (Autodesk) were used to generate the .stl files used to make the g-code for the printed scaffolds. Solidworks was used to make the log-pile geometry with two different sizes: (1) 10.5mm x 10.5mm x 12mm, and (2) 6mm³, both containing sufficient porosities that allowed for repeatable and mechanically reliable prints. In addition to log-pile scaffolds, two complex geometries were fabricated using a computerized tomography (CT) scan of a right femur. The scans were converted to .stl files and added to Meshmixer, a program that allows for unique customization of .stl files in order to make user-specified designs that could be printed reliably.

To test the mechanical strength of the scaffolds, the larger log-pile structures (**Fig. 3.1**) were placed between two plates on a compression MTS machine (Sintech 2 G) with a 10K Newton load cell. The samples were compressed to failure and the machine recorded the downward cross head travel and the force from the load cell.

3.3.4 Cell incorporation within log-pile scaffolds

A mixture of gelatin methacrylate (GelMA) mixed with human osteosarcoma cells (Saos-2) were incorporated within log-pile scaffolds. Using a previously reported protocol GelMA was synthesized.[21, 22] Briefly, porcine skin gelatin was mixed at 10% (w/v) in phosphate buffered saline (PBS, Thermo Fisher Scientific) and stirred at 45°C until dissolved. After the porcine skin gelatin was dissolved, methacrylic anhydride was added to the solution and stirred at the same temperature for 3 hours. After stirring, the solution was dialyzed against distilled water for seven days at 40°C, freeze-dried, and stored at -80°C until needed. For cell encapsulation experiments, a final GelMA prepolymer solution of 7% was prepared by mixing freeze-dried GelMA with PBS and 0.25% UV photoinitiator Irgacure 2959 (Specialty Chemicals, Switzerland) at room temperature.

Human osteosarcoma cells (Saos-2) were purchased from American Type Culture Collection (ATCC) and cultured in Dulbecco's Modification of Eagle's Media (DMEM; Life Technologies) supplemented with 10% fetal bovine serum (v/v) (FBS lot K14133; Atlanta Biological), 1% penicillin-streptomycin (Life Technologies) and 1% GlutaMAX (Life Technologies). Cells were passaged using 0.25% trypsin-EDTA (Life Technologies) and maintained at 37°C. A mixture of GelMA and Saos-2 cells was created by adding 20 μ L of a cell solution containing approximately 5000 cells/ μ L to 130 μ L of GelMA prepolymer solution. Cell/GelMA solution was pipetted dropwise onto sterilized PCL, PCL/PLA, and PCL/HA scaffolds and subsequently crosslinked using a Hamamatsu LED Controller (Hamamatsu C11924-511; Hamamatsu Photonics K.K., Japan). Viability of cells were analyzed using a Live/Dead assay on day 5. To evaluate cell viability, scaffolds were placed in media containing calcein-AM (1:2000 dilution; Life

Technologies) and ethidium homodimer (1:500 dilution; Life Technologies) and incubated at 37°C for 1 hour. After 1 hour, scaffolds were cut into three equal pieces using single edge industrial razor blades and imaged using an epifluorescence microscope (Nikon, Eclipse E-400, Nikon Corporation, Japan). Raw .tiff images were taken for all samples and processed linearly for contrast and brightness using Adobe Photoshop CC 2015 (Adobe Systems Inc., CA). Processed images were overlaid and false colored to create final live/dead images with green representing live cells and red representing dead cells. Brightfield images were not processed linearly for contrast and brightness. Images were also obtained using Hirox KH-8700 digital microscope (Hirox-USA, Inc., NJ).

3.4 Results

3.4.1 3D printing using hybrid PCL spools

The overall process of manufacturing log-pile geometries using hybrid spools is depicted in Figure 1. In order to manufacture spools, a Randcastle microfilament extruder was used to combine base PCL material with either HA or PLA (**Fig. 3.1A**). Extruded filaments of an appropriate diameter of 1.75 ± 0.05 mm could then be wound and fed into a commercially available Makerbot Replicator 2 3D printer (**Fig. 3.1B**).

A range of process parameters used for 3D printing (**Fig. 3.1C**) were determined from the melting point and degradation point information for each spool that were obtained from thermogravimetric analysis. A set of temperatures were chosen within these ranges and optimized such that the spools could be fed into the machine in a reliable and repeatable manner.

Temperature, which was the critical variable, was adjusted to allow easy printability (extrusion) using viscous melts.

For clarity, the “diameter” variable does not refer to the diameter of the spool, but rather to a number fed into Makerbot Slicer program. This was necessary to compensate the pushing force on various spools. For PCL and PCL-HA spools, this variable was decreased from 1.75mm (standard size) to 1.5mm in order to force the extruder to push more filament out, effectively compensating for the differences in density from PLA (1.4g/cm³) to PCL (1.14g/cm³). Finalized log-pile prints were realized after optimizing the printing conditions (**Fig. 3.1D**).

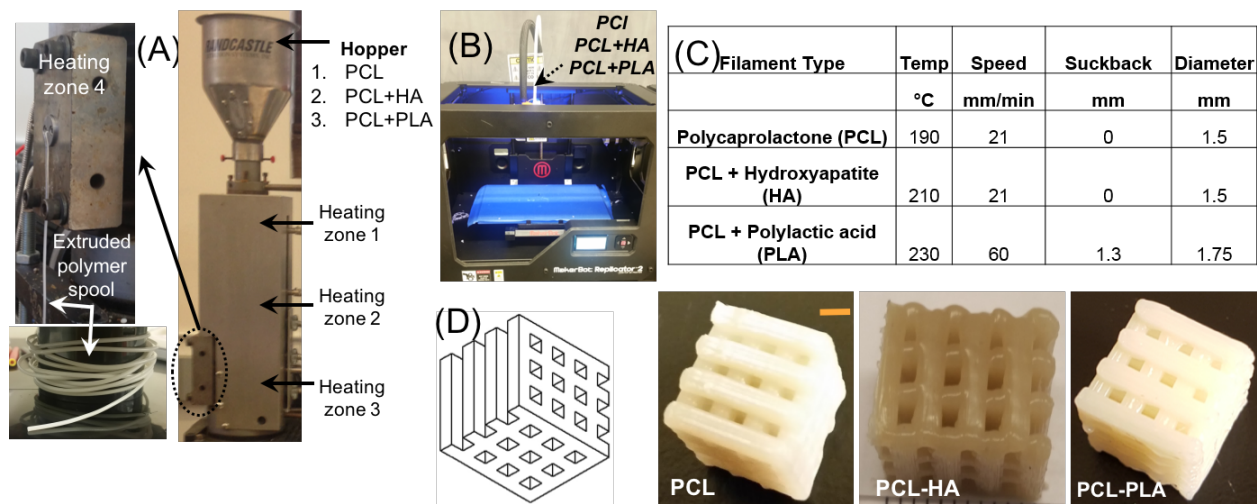


Figure 3.1: 3D printing schematic using hybrid PCL spools. (A) The raw material is fed into the filament extruder creating a long strand of three polymer spools (PCL, PCL-HA, and PCL-PLA). (B) A commercially available MakerBot Replicator 3D printer. (C) The printer settings are set for each filament spool, respectively. (D) The model of the log-pile scaffolds and the printed counterparts to the right. Scale bar: 2mm. HA, hydroxyapatite; PCL, polycaprolactone; PLA, polylactic acid.

3.4.2 Composition and mechanical properties of printed scaffolds

High-resolution thermogravimetric analysis (**Fig. 3.2A**) was used to quantify the exact amount of filler (PLA or HA) in the PCL matrix. The sample was heated above its degradation point and the derivative of the heat of the furnace (the rate of heating) was measured as it related to the drop in weight of the test-sample. This analysis was used primarily to demonstrate two distinct degradation points and a % composition of hybrid samples (**Fig. 3.2A, B**). Both PCL and PCL-HA had a degradation point of 383°C and the change weight between PCL and PCL-HA (15.81%) was representative of the weight of HA present in PCL-HA spool, as inorganic HA does not degrade and remains on the balance after complete degradation of the PCL component. The actual amount of HA was found to be slightly lower after thermogravimetric analysis than was present during the spool-making process (15.81% as compared to 20%).

Similarly, the amount of PLA was found to be slightly lower after analysis. The mixture of PCL and PLA had two distinct degradation points (the first degradation point for PLA being at 325°C and the second point for PCL being at 355°C) which were used as markers for determining the percentage of each constituent in the combined spool (**Fig. 3.2B**). From the thermogravimetric analysis, the exact amount of PLA in PCL matrix was determined to be 47.7%, a minor deviation from the 50:50 ratio initially put into the extrusion hopper

Mechanical properties for log-pile scaffolds were obtained from the stress-strain curves using a MTS machine (**Fig. 3.2B, C, D**). PCL-PLA, PCL-HA and PCL had average compressive strength of 159.2 MPa, 59.3 MPa and 44.3 MPa respectively (n=5). The increase in moduli in the

hybrid PCL-PLA spools was a result of the higher moduli of pure PLA filler added to the PCL matrix.

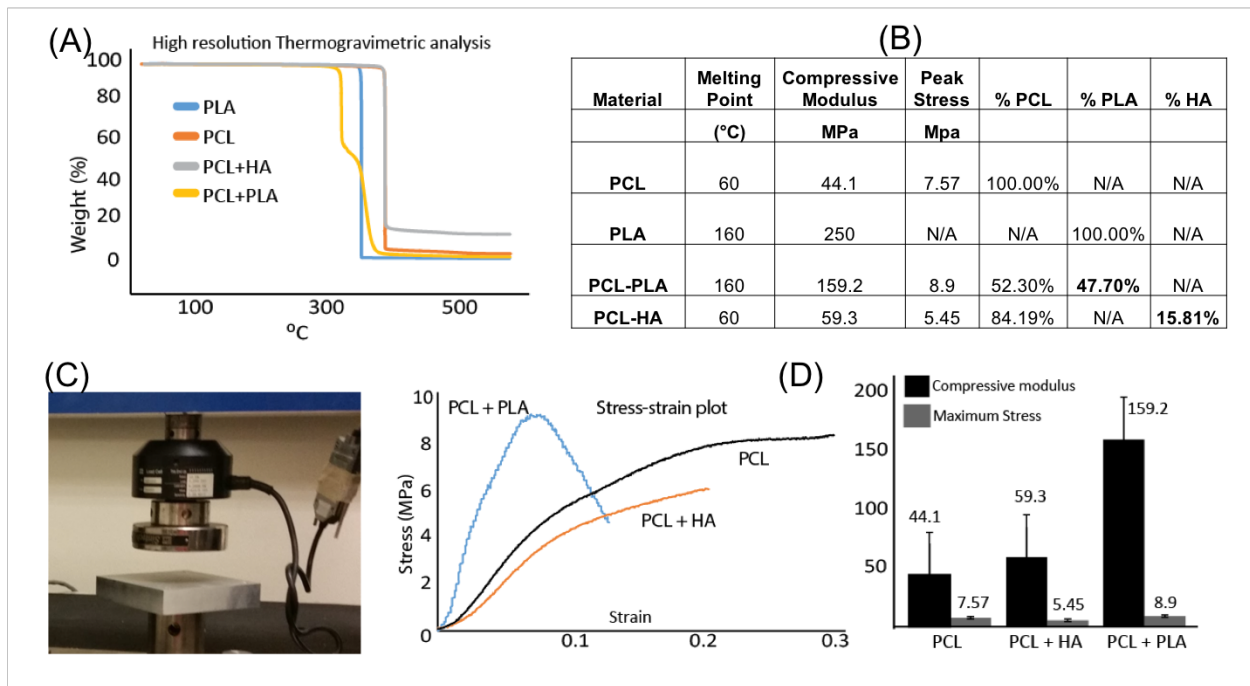


Figure 3.2: Printed scaffold compositions and mechanical properties. (A) High-resolution TGA of polymer spools. (B) Results in tabular form showing the degradation points and percentages for each compound. (C) Compression testing apparatus to obtain mechanical properties of log-pile scaffolds. (D) Stress-strain plots and bar graphs of modulus and maximum stresses for each polymer spool (n=5). TGA, thermogravimetric analysis.

3.4.3 3D printing of complex porous geometries

PCL is a common biopolymer used for bone tissue engineering applications and its ability to be readily augmented and printed in specific shapes via commercial 3D printers could lead to enhanced clinical solutions for bone defects. Custom scaffolds for bone repair are able to be printed from Cartesian data obtained from a CT scan, allowing the possibility of patient-specific

support cages for bone tissue engineering (**Fig. 3.3**). The first geometry shown was created in order to have a log-pile lattice similar to the log-pile geometry described earlier and was modified from the .stl file of a human femur (**Fig. 3.3A**). A scaled femur model was placed into the mesh program and sliced in order to obtain a small cross section of the diaphysis. The Meshmixer program was then used to render the model into various different layers while keeping the same external geometry (**Fig. 3.3B**, red outline). The lattice structure was used to maximize the internal free space while minimizing the amount of material used to support reliable printing of the structure.

To increase the internal free space, another type of scaffold was developed using Voronoi analysis, a solution which only uses the surface data in the .stl file (**Fig. 3.3C**). The Voronoi was made by reducing the number of triangles on the surface of the .stl file and subsequently using the Dual Edges function to give them all a tubular thickness and density. For each filament, the .stl files were uploaded into the Makerbot Desktop software and the settings were edited in the slicing program to obtain printing repeatability. The resulting hollow cages maintained the external geometry as derived from the CT scan, while still leaving space for the incorporation of biomaterials containing living cells.

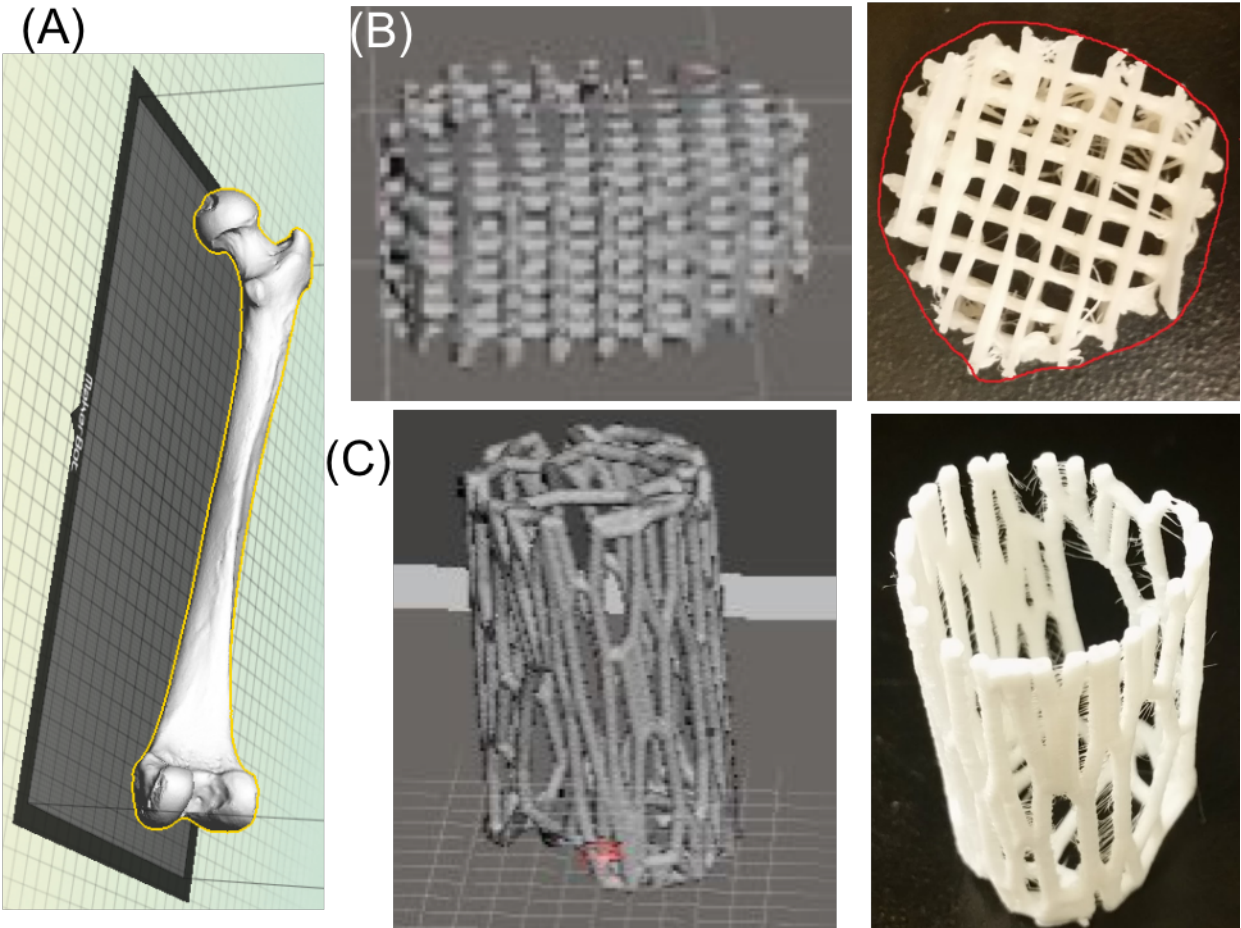


Figure 3.3: 3D printing of complex geometries. (A) Cartesian data for a human femur were placed into the MakerBot Desktop. (B) A slice from the diaphysis of the femur was taken and Lattice meshed in Meshmixer. On the right is the 3D printed model in PCL. (C) Longer slice from the diaphysis was Voronoi meshed in Meshmixer to create a hollow cage-like representation of the outside femur. On the right is the 3D printed PCL model.

3.4.4 Cell incorporation within log-pile scaffold

To visually model a process in which live cells could be contained within a 3D printed log-pile structure, a 6mm³ PCL log-pile scaffold was placed inside a rectangular chamber and

subsequently covered with 7% GelMA containing 15% (v/v) MiO orange coloring (Kraft Foods Inc., IL) (**Fig. 3.4A**). The GelMA was pipetted drop-wise onto the PCL scaffolds and simultaneously solidified using UV light exposure. Sliced sections from the top, middle, and bottom areas were successfully able to show a thorough incorporation of GelMA within in the interiors of the log-pile scaffold (**Fig. 3.4B**). As reported, the infusion process was facilitated by using a plastic column containing a small outlet port in the bottom of the chamber, thereby allowing an even flow-through of GelMA solution throughout the entire scaffold.

For cell encapsulation, a mixture of gelatin methacrylate (7% GelMA) and human osteosarcoma cells (5000 cells/ μ L; Saos-2) were incorporated within a PCL-PLA log-pile structure in a similar manner. After day 5, the log-pile structure was incubated with calcein-AM and ethidium homodimer and imaged fluorescently for live/dead analysis (**Fig. 3.4C**). Live cells (green) were shown in the top, middle and bottom sections of the sliced log-pile scaffold.

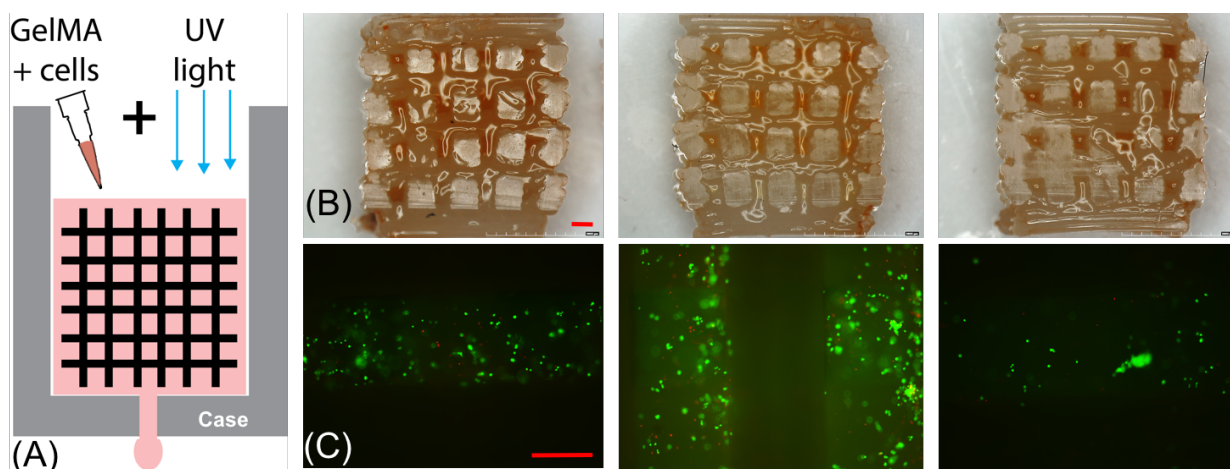


Figure 3.4: Incorporation of cells within 3D printed scaffolds. (A) Schematic representation of the process used for incorporating living cells within printed scaffolds. The case was slightly larger than the 6mm³ log-pile structure to allow for GelMA-cell solution perfusion. (B) PCL scaffold infused with 7% GelMA containing 15% (v/v) MiO orange coloring to show complete

infusion of GelMA throughout the scaffold (left to right: PCL GelMA top, PCL GelMA middle, PCL GelMA bottom). (C) Live (green)/Dead (red) calcein-AM/ethidium homodimer pictures from PCL/PLA scaffold (left to right: PCL-PLA GelMA top, PCL-PLA GelMA middle, PCL-PLA GelMA bottom). GelMA, gelatin methacrylate.

3.5 Discussion

We chose PCL as our base material due to its extensive use in developing scaffolds for bone tissue engineering. PCL is a semi-crystalline aliphatic polymer with suitable rheological properties such as glass transition temperature and melting point, and is readily biodegradable by hydrolysis.[23] HA, while a major component of native bone that has been shown to promote bone mineralization, is difficult to machine due to its brittle characteristics.[24, 25]

One significant challenge in creating the composite spools was the difficulties in achieving filaments of consistent diameter (1.75mm), a necessary requirement for several commercially available 3D printers. This was achieved by controlling the extruder-pressure and barrel screw revolution, and by varying the “suckback” variable on MakerBot (**Fig. 3.1C**). The “suckback” is typically set at 1.3mm at a velocity of 25mm/s in order to break off each extrusion. Since PCL has a high specific heat, “suckback” was set to zero to avoid blocking the printer nozzle.

A second challenge that will need to be addressed in subsequent studies is the apparent loss of both HA and PLA in the spool manufacturing process (**Fig. 3.2B**). As previously mentioned, there was a slight decrease in the amount of HA (15.81% as compared to 20%) and PLA (47.70% as compared to 50%) measured in the composite PCL-HA and PCL-PLA spools as

compared the starting materials placed into the hopper. While the exact cause of the loss is unknown, it is most likely attributed to the adhesion of HA and PLA to either the inner barrel of the extruder or any of the other various surfaces that they came in contact with throughout the manufacturing steps.

Natural bone is an organic/inorganic composite typically consisting of cortical and cancellous bone[26] with a compressive strength ranging from 131-205 MPa and a Young's Modulus ranging between 10 – 20 GPa.[27, 28] As reported here, the compressive strength of the hybrid spools had moduli ranging from 59-159MPa, thereby falling within the target zone required for bone tissue engineering. However, as the compressive strengths of the spools were on the low end of that of natural bone, more work would be needed to replicate the properties of natural bone.

Model scaffolds used for bone tissue engineering should mimic both the mechanical and chemical composition of natural bone. Since natural bone contains collagen fibers,[26] we decided to incorporate GelMA laden with living cells into the printed log-pile scaffolds. We chose GelMA, a denatured form of collagen, as the model hydrogel because it contains an abundance of biologically active cell-adhesion motifs, has highly controllable mechanical properties, and provides increased transparency for imaging.[29] Human Saos-2 cells were chosen in this study due to the fact that they are a robust cell line that can be used in the initial stages of new bone defect models. By choosing Saos-2 for our initial work, we were able to limit donor dependent differences that would arise from primary cells. In the future, we plan to use bone marrow derived stem cells to obtain an understanding of how scaffold design parameters influence the cell number and their metabolic activities. Integration of the structural

cage with cell-laden GelMA showed a construct compatible with the multifunctional nature of bone and showcased the potential for a tissue engineering model capable of improving the handling characteristics of soft hydrogel constructs under weight bearing conditions. The open frame design provided sufficient space for cell-laden hydrogels to support bone mineralization, remodeling, and integration with host tissues, while at the same time providing an interface that could possibly integrate with host tissues.

3.6 Conclusion

Polymers, with their favorable processing properties, have been extensively used to develop 3D scaffolds for tissue engineering applications. 3D printing of tissue engineering scaffolds often requires customized instruments such as heated extruders and computer controlled XYZ stages with precisely coordinated movements in order to lend themselves properly in the creation of biopolymer properties (viscosity, melting temperature, printing speed). This project developed hybrid spools with PCL polymer as the base material as well as hybrid spools readily compatible with commercial 3D printers such as the MakerBot. Porous geometries were printed using CT scan data with both internal log-pile lattice structures as well external meshed structures. Finally, we demonstrated that living cells mixed in gelatin hydrogels could be incorporated within log-pile scaffolds with high initial cellular viability.

Moving forward, while it was shown that cell-laden GelMA could be incorporated between the struts of PCL and PCL composites, the varying viability of the cells in the center and bottom of the log-pile scaffolds indicates that an inherent porosity is needed for the proper delivery of nutrients to the encapsulated cells. Additionally, as it was shown that the compressive strength

of the PCL and PCL cages were less than pure thermoplastic PLA cages alone, future work in the manufacturing of a structurally supported cell-laden hydrogel will utilize pure thermoplastic cages instead of PCL composites.

3.7 Non-Author Acknowledgements

We acknowledge Syracuse Biomaterial Institute (SBI) for providing equipment used for all the experiments in this paper. We thank Erin McMullin and Professor Patrick Mather for training and access to TGA instrument, Ciba Specialty Chemicals for photoinitiator samples, the Biology Department of Syracuse University for usage of confocal facility.

3.8 Disclosure statement

The authors have no financial or nonfinancial relationships to disclose.

3.9 References

1. Albrecht, L.D., S.W. Sawyer, and P. Soman, *Developing 3D scaffolds in the field of tissue engineering to treat complex bone defects*. 3D Printing and Additive Manufacturing, 2016. **3**(2): p. 106-112.
2. Liu, Y., J. Lim, and S.-H. Teoh, *Review: development of clinically relevant scaffolds for vascularised bone tissue engineering*. Biotechnology Advances, 2013. **31**(5): p. 688-705.
3. Domb, A.J., J. Kost, and D. Wiseman, *Handbook of biodegradable polymers*. Vol. 7. 1998: CRC Press.

4. Hutmacher, D.W., *Scaffolds in tissue engineering bone and cartilage*. Biomaterials, 2000. **21**(24): p. 2529-2543.
5. Atala, A., *Engineering tissues, organs and cells*. Journal of tissue engineering and regenerative medicine, 2007. **1**(2): p. 83-96.
6. Tarik Arafat, M., I. Gibson, and X. Li, *State of the art and future direction of additive manufactured scaffolds-based bone tissue engineering*. Rapid Prototyping Journal, 2014. **20**(1): p. 13-26.
7. Trachtenberg, J.E., et al., *Open-source three-dimensional printing of biodegradable polymer scaffolds for tissue engineering*. Journal of Biomedical Materials Research Part A, 2014. **102**(12): p. 4326-4335.
8. Chevalier, E., et al., *Fabrication of porous substrates: a review of processes using pore forming agents in the biomaterial field*. Journal of Pharmaceutical Sciences, 2008. **97**(3): p. 1135-1154.
9. Peltola, S.M., et al., *A review of rapid prototyping techniques for tissue engineering purposes*. Annals of Medicine, 2008. **40**(4): p. 268-280.
10. Billiet, T., et al., *A review of trends and limitations in hydrogel-rapid prototyping for tissue engineering*. Biomaterials, 2012. **33**(26): p. 6020-6041.
11. Williams, J.M., et al., *Bone tissue engineering using polycaprolactone scaffolds fabricated via selective laser sintering*. Biomaterials, 2005. **26**(23): p. 4817-4827.
12. Cooke, M.N., et al., *Use of stereolithography to manufacture critical-sized 3D biodegradable scaffolds for bone ingrowth*. Journal of Biomedical Materials Research Part B: Applied Biomaterials, 2003. **64**(2): p. 65-69.
13. Patrício, T., et al., *Fabrication and characterisation of PCL and PCL/PLA scaffolds for tissue engineering*. Rapid Prototyping Journal, 2014. **20**(2): p. 145-156.

14. Tuan, H.S. and D.W. Hutmacher, *Application of micro CT and computation modeling in bone tissue engineering*. Computer-Aided Design, 2005. **37**(11): p. 1151-1161.
15. Wei, C., et al., *High-precision flexible fabrication of tissue engineering scaffolds using distinct polymers*. Biofabrication, 2012. **4**(2): p. 025009.
16. Hutmacher, D.W., M. Sittinger, and M.V. Risbud, *Scaffold-based tissue engineering: rationale for computer-aided design and solid free-form fabrication systems*. Trends in Biotechnology, 2004. **22**(7): p. 354-362.
17. Gratson, G.M., et al., *Direct-write assembly of three-dimensional photonic crystals: conversion of polymer scaffolds to silicon hollow-woodpile structures*. 2005, DTIC Document.
18. Wang, F., et al., *Precision extruding deposition and characterization of cellular poly- ϵ -caprolactone tissue scaffolds*. Rapid Prototyping Journal, 2004. **10**(1): p. 42-49.
19. Park, S.H., et al., *Scaffolds for bone tissue engineering fabricated from two different materials by the rapid prototyping technique: PCL versus PLGA*. Journal of Materials Science: Materials in Medicine, 2012. **23**(11): p. 2671-2678.
20. Bose, S., S. Vahabzadeh, and A. Bandyopadhyay, *Bone tissue engineering using 3D printing*. Materials Today, 2013. **16**(12): p. 496-504.
21. Nichol, J.W., et al., *Cell-laden microengineered gelatin methacrylate hydrogels*. Biomaterials, 2010. **31**(21): p. 5536-5544.
22. Soman, P., et al., *Digital microfabrication of user-defined 3D microstructures in cell-laden hydrogels*. Biotechnology and Bioengineering, 2013. **110**(11): p. 3038-3047.
23. Sun, M. and S. Downes, *Physicochemical characterisation of novel ultra-thin biodegradable scaffolds for peripheral nerve repair*. Journal of Materials Science: Materials in Medicine, 2009. **20**(5): p. 1181-1192.

24. Shor, L., et al., *Fabrication of three-dimensional polycaprolactone/hydroxyapatite tissue scaffolds and osteoblast-scaffold interactions in vitro*. *Biomaterials*, 2007. **28**(35): p. 5291-5297.
25. Swetha, M., et al., *Biocomposites containing natural polymers and hydroxyapatite for bone tissue engineering*. *International Journal of Biological Macromolecules*, 2010. **47**(1): p. 1-4.
26. Rho, J.-Y., L. Kuhn-Spearing, and P. Zioupos, *Mechanical properties and the hierarchical structure of bone*. *Medical Engineering & Physics*, 1998. **20**(2): p. 92-102.
27. Kutz, M., *Standard handbook of biomedical engineering and design*. 2003: McGraw-Hill New York.
28. Rho, J.Y., R.B. Ashman, and C.H. Turner, *Young's modulus of trabecular and cortical bone material: ultrasonic and microtensile measurements*. *Journal of Biomechanics*, 1993. **26**(2): p. 111-119.
29. Chen, Y.X., et al., *A novel suspended hydrogel membrane platform for cell culture*. *Journal of Nanotechnology in Engineering and Medicine*, 2015. **6**(2): p. 021002.

CHAPTER 4: PERFUSION DIRECTED 3D MINERAL FORMATION WITHIN CELL-LADEN HYDROGELS^{Δ*}[1]

4.1 Abstract

Despite the promise of stem cell engineering and the new advances in bioprinting technologies, one of the major challenges in the manufacturing of large-scale bone tissue scaffolds is the inability to perfuse nutrients throughout thick constructs. Here, we report a scalable method to create perfusable bone constructs using a combination of cell-laden hydrogels and a 3D printed sacrificial polymer. Osteoblast-like Saos-2 cells were encapsulated within a gelatin methacrylate (GelMA) hydrogel and 3D printed polyvinyl alcohol (PVA) pipes were used to create perfusable channels. A custom-built bioreactor was used to perfuse osteogenic media directly through the channels in order to induce mineral deposition which was subsequently quantified via microCT. Histological staining was used to verify mineral deposition around the perfused channels, while COMSOL modeling was used to simulate oxygen diffusion between adjacent channels. This information was used to design a scaled-up construct containing a 3D array of perfusable channels within cell-laden GelMA. Progressive matrix mineralization was observed by cells surrounding perfused channels as opposed to surface mineral deposition in static constructs. MicroCT confirmed that there was a direct relationship between channel mineralization within perfused constructs and time within the bioreactor.

^Δ Adapted from: Sawyer SW, Shridhar SV, Zhang K, Albrecht LD, Filip AB, Horton JA, Soman P. (2018) Perfusion directed 3D mineral formation within cell-laden hydrogels. *Biofabrication* 10(3).

* Reprinted with permission from IOP Publishing with minor editing provisions.

4.2 Introduction

One of the largest barriers to engineering a large-scale bone tissue replacement is the ability to supply essential nutrients throughout the entire construct. Since hypoxia and necrosis occur to cells that lie outside of the natural diffusion range of 200–300 μm , proper vasculature must be available within the replacement tissue to ensure graft viability.[2-4] In traditional static culture systems, nutrient diffusion, and therefore mineralization and cellular viability, is limited to the outer 200-300 μm of the construct while deeper regions of the system remain hypoxic.[5, 6]

In an attempt to increase nutrient diffusion into engineered scaffolds, a variety of means such as solvent casting, particulate leaching, phase separation, gas foaming, emulsion freeze drying, and fiber meshes have been used to generate a wide range of porous scaffolds.[7-10] While these particular methods have been shown to enhance mass transfer within the machined constructs as well as improve cell seeding, cell proliferation, and construct mineralization, they unfortunately have not provided a complete solution. In particular, these methods do not easily provide the precise control over pore parameters needed for larger tissue constructs and can often result in inhomogeneous cellular densities and outcome measures that are hard to predict. Furthermore, since these methods often require harsh solvents and high temperatures, incorporating live cells during fabrication is near impossible.[10-12] Alternatively, the encapsulation of osteogenic cells within biocompatible hydrogel bioinks such as collagen, alginate, and gelatin can allow for a uniform and controlled distribution of cells *in situ*. [13-20] However, the absence of macroporous voids in the cell-laden hydrogel constructs present similar nutrient diffusion limitations.[4] Additionally, although the cell friendly hydrogel provides an environment which is able to closely

mimic the natural extracellular matrix, their weak mechanical stability provides yet another obstacle for their use in bone tissue engineering.

Recently, 3D printing technologies have enabled the creation of user-defined channels within cell-laden hydrogels through the extrusion of bioinks in a layer-by-layer manner alongside co-printed sacrificial materials.[21-28] Post-print, the sacrificial material is removed via non-toxic means, resulting in user defined channels within bulk gels. However, methods such as this require custom-made bioprinters with specialized control hardware and software as well as tunable viscoelastic bioinks that must be specifically matched with the printing parameters. While perfusion of these constructs with nutrients is possible, the systems used are difficult to scale.

A simpler, and readily scalable, fabrication method is one that combines the casting of cell-laden hydrogels around pre-fabricated 3D printed structures containing sacrificial materials. In this work, we utilize an unmodified, commercially available 3D printer and water soluble sacrificial material (PVA) to establish perfusable channels within the center of a diffusion limited, structurally supported GelMA hydrogel laden with osteoblast-like cells. The construct is designed to have one inlet and one outlet that provides a direct interface between the cell-laden GelMA and perfusion of nutrients via a scalable, pump-driven bioreactor system. The simple horizontal channel geometry provides a robust method with which to analyze the influence of long-term (4week) perfusion of osteogenic media on the viability and function of encapsulated cells. Additionally, COMSOL modeling of oxygen diffusion is used to determine optimal spacing between adjacent 3D printed channels, allowing for the design to be scaled up into a perfusable, 5 pipe array.

4.3 Materials and Methods

4.3.1 3D printing of frames and pipes

Acrylonitrile butadiene styrene (ABS) thermoplastic frames with inner dimensions of 9mm long x 6mm wide x 3mm deep containing 1mm holes along the construct peripheries and sacrificial polyvinyl alcohol (PVA, 400 μ m diameter) pipes were printed using a commercially available MakerBot Replicator 2 3D printer (MakerBot) (**Fig. 4.1A**). PVA pipes were UV sterilized for 24 hours and ABS frames were sterilized via submersion in 70% EtOH for 24 hours.

4.3.2 Design and fabrication of polycarbonate bioreactor

Polycarbonate bioreactors were machined from clear, autoclavable, scratch and UV resistant polycarbonate sheets (McMaster-Carr) (**Fig. 4.1 D-F**). Briefly, pre-milled polycarbonate blanks were machined in a MT300 Pro CNC Milling Center (AutoMateCNC) to create both the bottom bioreactor base and its corresponding top plate (**Fig. S4.1-2**). The bottom bioreactor base plate contained four wells approximately 13mm long x 9mm wide x 3mm deep surrounded by 10 screw holes machined using a #43 drill bit. Vertical holes for perfusion along the periphery of the base plate were machined using a #52 (outer) and #72 (inner) drill bit for 21G needle (Thermo Fisher Scientific) insertion. Top plates contained screw holes machined using a #34 drill bit. To ensure a water-tight seal between the polycarbonate base and top, a polydimethylsiloxane gasket (PDMS, Ellsworth Adhesives) mixed in a 1:4 ratio was cured at 60°C for 24 hours and inserted between the base and top sections.

4.3.3 Gelatin methacrylate (GelMA) synthesis

20% (w/v) gelatin methacrylate (GelMA) prepolymer solution used for cellular encapsulation was synthesized according to our previous work.[29] Briefly, porcine skin gelatin (Sigma Aldrich) was mixed at 10% (w/v) in phosphate buffered saline (PBS, Thermo Fisher Scientific) and reacted with methacrylic anhydride (Sigma Aldrich). After dialysis and lyophilization, GelMA macromer was stored at -80°C until needed. Prior to cellular encapsulation, GelMA macromer was combined with PBS and 0.25% UV photo-initiator Irgacure 2959 (Specialty Chemicals) to form the prepolymer solution and sterile filtered using a 0.20 µm filter (Corning).

4.3.4 Cell culture and perfusion setup

Human osteosarcoma cells (Saos-2, ATCC), which can be used to represent the early stages of osteogenesis,[30] were chosen as osteoblast analogues for our model system. Dulbecco's Modification of Eagle's Media (DMEM, Life Technologies) supplemented with 1% Glutamax (Life Technologies), 1% penicillin-streptomycin (Life Technologies), and 10% fetal bovine serum (FBS lot G12102, Atlanta Biologicals) was used as the base media for Saos-2 culture. Cells were maintained at 37°C in a humidified, 5% CO₂ atmosphere and passaged prior to any new experiment. In order to chemically induce Saos-2 cells to produce mineral, the base media was supplemented with 100 µM L-ascorbic acid-2-phosphate (AA2P, Sigma-Aldrich), 5mM β-glycerophosphate (BGP, Sigma-Aldrich), and 10 nM dexamethasone (DEX, Sigma-Aldrich).

Prior to in situ polymerization, approximately 1×10^6 cells were suspended in 20% (w/v) GelMA to create a 15% (w/v) solution (162 µl final volume), and transferred to the 3D printed hybrid ABS

frame/PVA pipe construct via dropwise pipetting (**Fig. 4.1B**). After the construct was filled, the cell-GelMA solution was UV cured for 1 minute 20 seconds at approximately 5 mW/cm² via a Hamamatsu LED Controller (Hamamatsu C11924-51; Hamamatsu Photonics K.K., Japan). PVA pipes were eluted from the constructs by incubation for 24 hours in warmed media (**Fig. 4.1C**). Constructs destined for static culture conditions remained in 12-well culture dishes, with media renewed every 2-3 days. Constructs destined for perfusion conditions were transferred and press fit within the polycarbonate bioreactor base (**Fig. 4.1D-E**). Construct perfusion was maintained using a syringe pump system (NE-300 Just InfusionTM, New Era) at 0.2 μ l/hr per well, for up to 28 days (**Fig. 4.1F**). Syringes were replaced as needed during the course of the experiments.

4.3.5 Cellular viability

Cell viability of encapsulated Saos-2 cells was evaluated using a Live/Dead assay for two time points: 1 day after encapsulation and 14 days after either perfusion or static culture using osteogenic media. Samples to be evaluated were sliced into 1mm thick sections and transferred into culture media supplemented with calcein-AM (live, 1:2000 dilution, Life Technologies) and ethidium homodimer (dead, 1:500 dilution, Life Technologies) for one hour prior to imaging.

4.3.6 MicroCT analysis

Constructs were removed from the bioreactor intact, fixed in formaldehyde (4% for 24 hours), washed in PBS, and placed lengthwise in a 16 mm diameter sample holder for micro-CT imaging (micro-CT 40, Scanco Medical AG, Brüttisellen, Switzerland). Foam spacers were placed between samples, which were kept hydrated with PBS. Samples were imaged at a 16-20 μ m isotropic voxel

resolution (55 kV, 145 mA, 200 ms integration time). After scanning, mineralized tissue volume (bone volume, BV) and density (BMD) were calculated by applying a lower global threshold (166 mg HA/cm³) to the image, which was digitally contoured to isolate the entire length of the perfusion channel from the bulk construct mass (**Fig. S4.3**). Thickness of the mineralized matrix surrounding the perfusion channel was calculated using the 2D section morphology tool in BoneJ.[31] Briefly, the reconstructed micro-CT images (.isq files) were imported into ImageJ, cropped to isolate the perfusion channel, and a global threshold of 166 mg HA/cm³ was applied prior to running BoneJ. The BoneJ plugin then calculates an average “cortical thickness” for each image slice, which corresponds to mineral wall thickness in this model. Consistency in thresholding between ImageJ and Scanco software was ensured by importing a scan of the Scanco hydroxyapatite (HA) quality control phantom into ImageJ, and plotting greyscale (ImageJ) values vs. HA density. However, based on the fact that the structural organization and chemical constitution of the deposited mineral cannot be verified via micro-CT, the cell-mediated deposition is referred to as “mineral” in the subsequent text.

4.3.7 Histological analysis

Perfused samples were prepared for histological analysis via standard snap freezing protocols. Briefly, samples were fixed in 4% formaldehyde for 24 hours before treatment with a 30% sucrose in PBS solution for 48 hours. After sucrose treatment, samples were embedded in Tissue Freezing Medium (Electron Microscopy Sciences) and frozen over dry ice. Sections (10µm thick) were cut on a Leica CM3050 cryostat (Leica Biosystems, Germany) and mounted on lysine coated SuperFrost Plus slides. Cover-slipped and stained sections were imaged using a Nikon Eclipse E-400 microscope (Nikon Corporation).

Hematoxylin and Eosin (H&E) Staining: Sections were stained by standard H&E procedure using Mayer's Hematoxylin and Eosin/Phloxine solutions (Electron Microscopy Sciences). Sections were then dehydrated through an ethanol series, cleared in xylene, and cover-slipped with Permount (Fisher Scientific) for imaging. Imaged sections were analyzed via ImageJ (NIH) for cell quantification.

Alizarin Red S Staining: Calcium mineral deposition was visualized using 40mM Alizarin Red S solution (4.1 pH, Sigma). After staining for 5 minutes, slides were washed in deionized water and mounted and imaged as previously described.

Image J Box Plot Analysis: H&E images were imported into ImageJ and analyzed via a box analysis for cell quantification. Briefly, images were converted to binary via automatic thresholding and values representing cells were recorded in boxed increments of 325 μm^2 away from the edge of the channel lumen. For each image, three different directions were analyzed away from the central channel.

4.3.8 COMSOL modeling

COMSOL was first used to model oxygen diffusion within cell-laden GelMA constructs between adjacent channels spaced 1mm apart (edge-to-edge). Two domains were considered. Domain 1 represented the primary flow of nutrients supplied from the inlet reservoir and was solved using Navier-Stokes steady state flow analysis. Domain 2 represented the diffusion of media and consumption by cells, and was solved by diffusion-consumption analysis using Michaelis–Menten rate laws. The “Reacting Flow of Porous Media” module in COMSOL was used to plot steady state oxygen diffusion within cell-laden GelMA. The GelMA matrix was represented via user-

defined material values of porosity (0.5)[32], and permeability (1×10^{-7})[33]. The maximum amount of dissolvable oxygen was assumed to be 0.2185 [mol.m⁻³][34], approximately representing oxygen dissolved in water. The consumption of oxygen by cells was represented as a decrease in oxygen species over time, following the equation, $R = -kt$, where R is the reaction rate ($R < 0$), k is the rate constant relating to oxygen concentration, and t is time in [s]. The rate constant was determined to be 2×10^{-5} [mol.s⁻¹] by taking into account the oxygen consumption rate of cells within each GelMA construct.[35]

COMSOL was also used to model the changes in oxygen diffusion within cell-laden GelMA constructs due to mineral deposition around the lumen/channels. In this model, three domains were considered. Domain 1 represented the primary flow of nutrients supplied from the inlet reservoir and Domain 2 represented the diffusion of media and consumption by cells encapsulated within GelMA. A new Domain 3 was introduced in the form of a donut-shell and represented both regions of mineral deposition and cell-laden GelMA. With more perfusion time, the thickness of Domain 3 increased and the porosity decreased due to an increasing amount of mineral deposition. The thickness of the donut-shell Domain 3 was obtained from Image J data, while the material porosity of Domain 3 ($P_{donut-shell}$) at weeks 1, 2, and 4 was calculated as described below. The porosity of Domain 3 was a combination of (i) the porosity of the mineralized GelMA (identified from CT data) and (ii) the porosity of cell-laden GelMA (identified as void regions in CT data) given by the following equation (**Fig. 4.6B-C**):

$$P_{donut-shell} = A * P_{mineral} + (1 - A) * P_{GelMA}$$

where A is the fraction of the donut-shell area occupied by mineralized GelMA and $(1-A)$ is the remaining fraction that is occupied by cell-laden GelMA. Porosity of pure bone, $P_{mineral}$ (0.035) and cell-laden GelMA P_{GelMA} (0.5) were obtained from previously published work[32, 36]. In this

work, the inner channel radius was assumed to be 0.2 mm while the outer donut-shell radius for weeks 1, 2 and 4 were calculated as 0.2719 mm, 0.2854 mm and 0.2873 mm respectively from the Bone J cortical thickness measurements of the mineralized crust. A , the fraction of donut shell area occupied by the mineral, was calculated via a two-step process. First, CT data was imported into MIMICS (Materialise, Belgium), a medical image processing software program, and 30 surface slices were generated for each time point and converted into 2D masks before being exported into Image J as binary (.stl) files. Second, the freehand boundary option in Image J was used to mark the irregular outer boundaries in each image to calculate the area occupied by mineral and void regions (area occupied by cell-laden GelMA). This data was then used to calculate $P_{donut-shell}$ for week 1, 2 and 4 (**Fig. 4.6D**).

4.3.9 Statistical analysis

Numerical data was entered into Microsoft Excel to calculate mean and standard deviation and either Student's t-test or one-way ANOVA was used to assess statistical significance of differences. P-values less than 0.05 were accepted as statistically significant.

4.4 Results

4.4.1 Design and fabrication of a plug-and-flow construct

Mechanically supportive ABS cages capable of housing GelMA hydrogels were printed using a commercially available 3D printer. Sacrificial polyvinyl alcohol (PVA) pipes were printed and inserted into holes within the ABS cage peripheries (**white, Fig. 4.1A, B**). GelMA prepolymer was

cast into the constructs and UV cured (**Fig. 4.1B, C**) prior to the dissolution of the pipes (**Fig. 4.1C**). A fully customizable, two-piece plug-and-flow bioreactor fitted with a PDMS gasket was used to house the 3D printed constructs (**Fig. 4.1D-F, S4.1-2**). Within the bioreactor base, the 3D printed constructs containing GelMA hydrogels could be press fit and perfused with DI water containing an orange food dye via a standard syringe pump. Flowing wells containing no constructs showed fluid-tight seals (**Fig. 4.1E middle-top**) while the well containing an ABS cage and GelMA hydrogel with dissolved pipe showed directed dye flow (**Fig. 4.1E bottom**).

All aspects of the plug-and-flow model process were capable of being fully sterilized using conventional techniques. Specifically, the PVA pipes and bioreactors were UV sterilized for 24 hours prior to use and the ABS frames were sterilized in 70% EtOH. Accordingly, the system was capable of being placed within a standard cell culture incubator for extended periods of time (**Fig. 4.1F**). Nutrients needed for cell viability were perfused through the constructs via a syringe pump placed within the incubator and gas exchange took place through a pressure relief needle in the waste collection area.

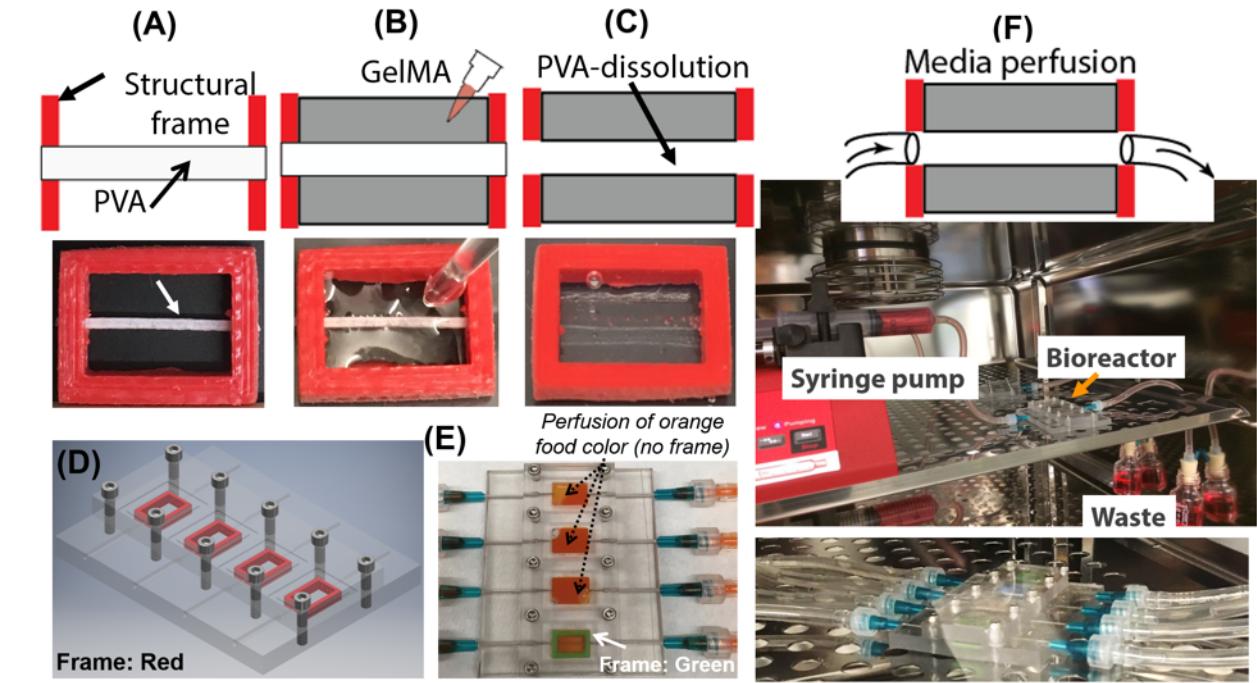


Figure 4.1: Design and performance testing of 3D-printed construct and bioreactor apparatus. Schematic and representative images of the mechanically supportive ABS frame with inserted pipe before (A) and after (B) photopolymerization of GelMA, and after dissolution of the sacrificial PVA pipe (C). Schematic image of a two-piece polycarbonate bioreactor containing a PDMS gasket between layers (D) and leakage test of polycarbonate bioreactor showing liquid-tight seal in machined device (E). Complete bioreactor setup inside a standard cell culture incubator (F).

4.4.2 Perfusable GelMA hydrogels containing Saos-2 cells

In order to create cell-laden GelMA hydrogels containing encapsulated cells and fully perfusable pipes, Saos-2 cells were added to GelMA prepolymer and cast into the constructs. After curing, constructs were placed in cell culture media for 24 hours prior to being placed in either well plates for static culture or the bioreactor for perfusion with osteogenic media (Fig. 4.2A). To determine

if the plug-and-flow bioreactor represented a viable cell culture platform, cells were encapsulated around the dissolvable pipes and cultured for 24 hours in order to determine process associated cell death. After one day of culture, minimal cell death was observed around the dissolved pipe (**red, Fig. 4.2B**). Constructs perfused with osteogenic media for two weeks showed high cell viability (**green, Fig. 4.2C**) and mineral deposition around the entirety of the pipe (**Fig. 4.2D**). MicroCT imaging showed mineral deposition surrounding the channel along the entire length of the construct (**Fig. 4.2E**).

Control experiments were run with cell-laden GelMA constructs without channels. Cells were encapsulated within ABS cages containing no dissolvable pipes and incubated for either 1 day or 14 days in osteogenic media (**Fig. 4.2F**). After 1 day of culture constructs were sectioned into 1mm slices and showed low cell viability in the center of the hydrogel (**red, Fig. 4.2G**). After 14 days of static culture high cell death, in addition to a decreased number of cells, was observed (**Fig. 4.2H**) and no mineral appeared to form in the center of the hydrogel (**Fig. 4.2I, J**).

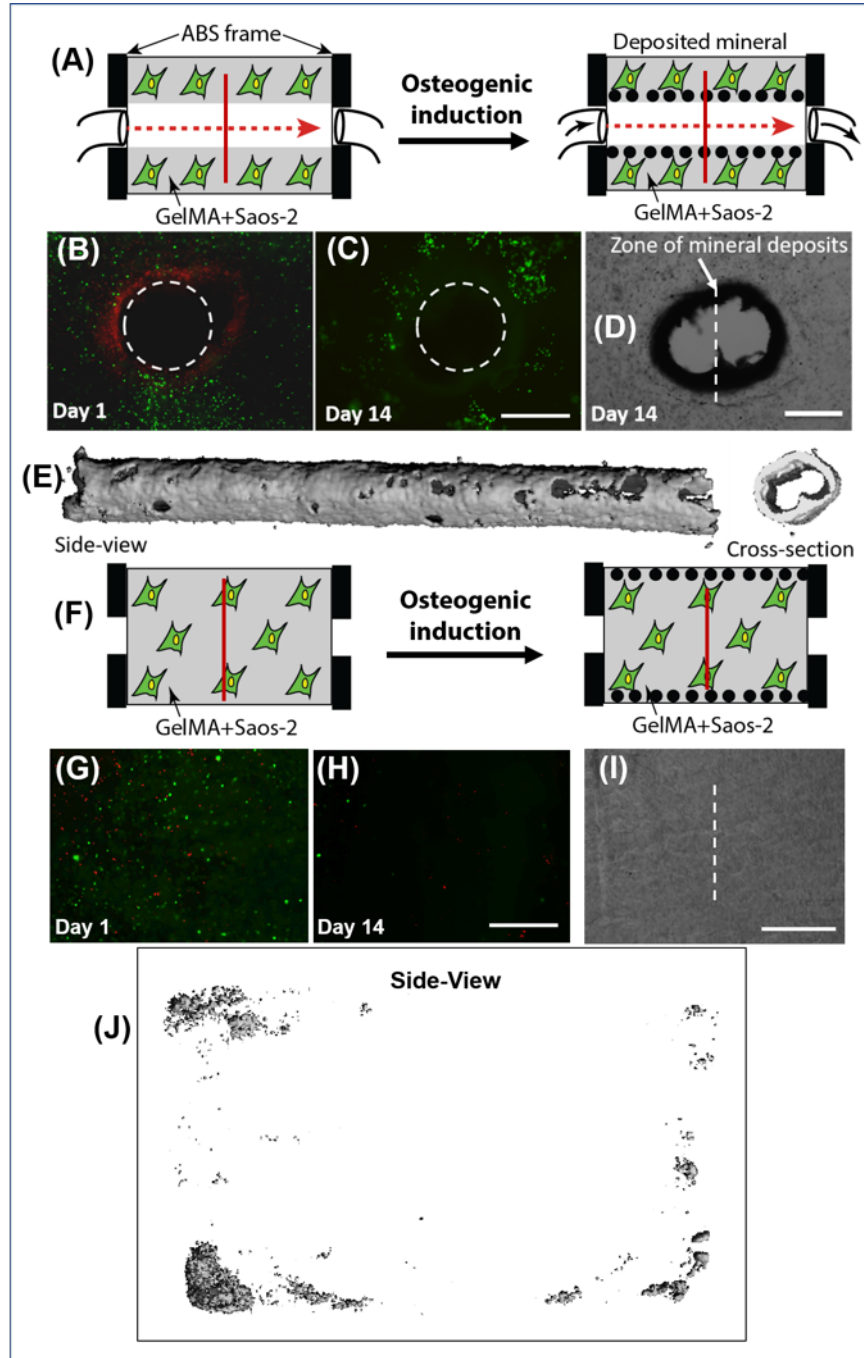


Figure 4.2: Perfusion can direct mineral deposition. Schematic representation of outcomes following osteogenic induction under (A) perfusion or (F) static culture conditions. Cell viability by fluorescent live (green)/dead (red) staining after perfusion (B, C) or static culture (G, H) conditions for either 1 (B, G) or 14 days (C, H) respectively. Brightfield microscopy showed an accumulation of an opaque matrix surrounding the perfused pipe (D) that was not evident in static

constructs lacking a pipe (**I**) (scale bar: 400 μ m). Micro-CT imaging demonstrated mineral deposits surrounding the perfused pipe (**E**), whereas mineral accumulated only at the periphery of constructs maintained in static conditions (**J**).

4.4.3 Channel mineralization and modeling

MicroCT was used to evaluate mineral formation around the construct channels under both static and dynamic conditions. Samples cultured within the bioreactor and perfused with osteogenic media for either 1 (P-W1), 2 (P-W2), or 4 (P-W4) weeks showed robust mineralization along the channel walls (**Fig. 4.3A, Right**). Solid samples containing no channels in static osteogenic culture showed mineral deposition around the construct periphery with no quantifiable activity within the center of the construct (**Fig. 4.2J**). Under the same conditions, constructs with channels were cultured in static osteogenic conditions for either 1 (S-W1), 2 (S-W2), or 4 (S-W4) weeks and showed increasing amounts of mineral deposition along the central pipe walls (**Fig. 4.3A, Left**). Additionally, in the static culture mineral was also deposited on the surface of the constructs, but appeared random and unordered. Furthermore, acellular control experiments showed no presence of mineral, indicating that the mineralization was completely mediated by encapsulated Saos-2 cells.

For mineral quantification, only the central channels of the constructs were digitally contoured in order to normalize comparisons between static and perfused samples (**Fig. S4.3**). Quantification of micro-CT data for the central channels of each construct showed that after one month of either static or perfusion culture, mineralization of the inner lumens increased significantly both volumetrically and in total mineral content for the 4 week samples as compared to their 1 and 2

week counterparts (**Fig. 4.3B, S4.4**). Additionally, perfused constructs did not have significantly more mineral around their inner lumens as compared to their static equivalents. Furthermore, despite the increase in mineral content, the density of mineral formed was consistent among all samples at all time points, regardless of culture type (**Fig. 4.3C**).

To further characterize the constructs perfused within the bioreactor, BoneJ was used to analyze the micro-CT data to determine the average thickness of the mineral ring formed around the central channels (**Fig. 4.6D, Table**). While an upward trend in thickness could be inferred based on the data available, there was no statistically significant change as a function of time. Additionally, although total mineral content did increase significantly over the course of 4 weeks for the perfused samples, the high variability in data, as well as the fact that the total mineral formed was not significantly greater in the perfused samples as compared to their static counterparts (**Fig. S4.4**), suggested that an increasing crust thickness could be inhibiting diffusion into the surrounding hydrogel matrix.

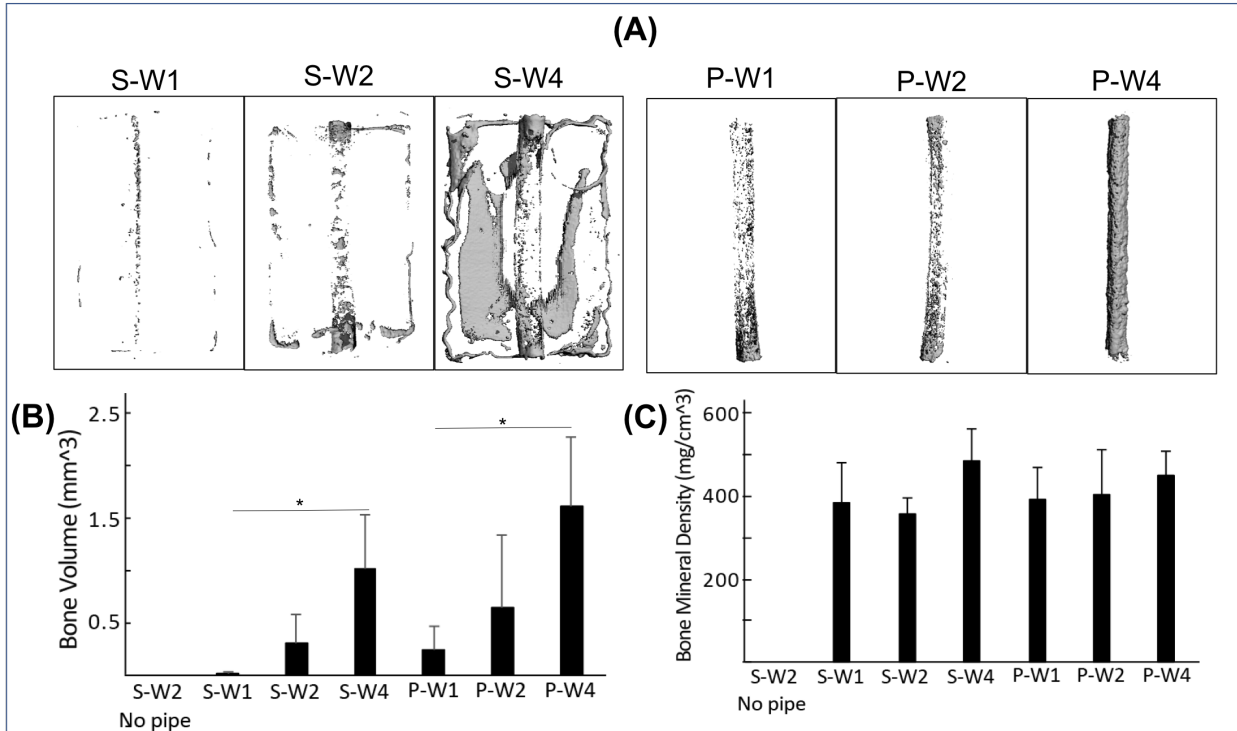


Figure 4.3: MicroCT analysis of mineral deposition. Representative microCT image of total mineral deposition after culture in osteogenic media under static (S) or perfused (P) conditions for 1, 2, or 4 weeks (A). For representative images, the entire frame was digitally contoured in order to visually show how mineralization occurs in static samples immersed in osteogenic media versus samples perfused directly with osteogenic media. Mineral volume deposited around pipes after 1, 2, or 4 weeks of both static osteogenic culture and osteogenic media perfusion showed significant increases in volume after 4 weeks (4wk static and 4wk flow n=7, 2wk flow n=8, rest n=6. * p<0.05 via one-way ANOVA) (B). Density of mineral deposited around pipe after 1, 2, or 4 weeks of both static osteogenic culture and osteogenic media perfusion remained constant at every time point (4wk static and 4wk flow n=7, 2wk flow n=8, rest n=6) (C).

4.4.4 Histological analysis and quantification

Alizarin red S staining was used to visualize whether the diffusion limitations affected mineralization away from the perfused pipes, as well as verify that the deposits observed by the micro-CT contained calcium. After one week of perfusion, a small amount of mineral was present away from the pipe (**Fig. 4.4 A, P-W1**). After two weeks of perfusion, an increase of mineral was observed away from the perfused lumen, but appeared to decrease to levels consistent with 1 week of flow as the distance increased towards the construct peripheries (**Fig. 4.4A, P-W2**). After 4 weeks of perfusion, however, while the amount of mineral observed closest to the pipe did not appear to increase significantly, more robust staining was observed (**Fig. 4.4A, P-W-4**). Additionally, a significant amount of mineral was detected further away from the pipe in the 4 week samples as compared to both the 1 and 2 week samples, indicating that hydrogel degradation may possibly have played a role in the ability of the Saos-2 cells to mineralize the matrix after 4 weeks of perfusion.

H&E staining was performed on the perfused samples to visualize differences in construct cellularity over time (**Fig. 4.4B**) and a histogram analysis was used to quantify what effect long term diffusion had on the distribution of cells away from the channel lumen (**Fig. 4.4C,D**). After one week of perfusion, a large number of cells were observed approximately 300 μ m away from the channel, a distance in accordance with diffusion limitation values as reported in the literature (**Fig. 4.4B,D**).^[37] However, as the mineral crust increased over the course of 2 weeks to 1 month, the quantity of cells dropped significantly 300 μ m away from the pipe.

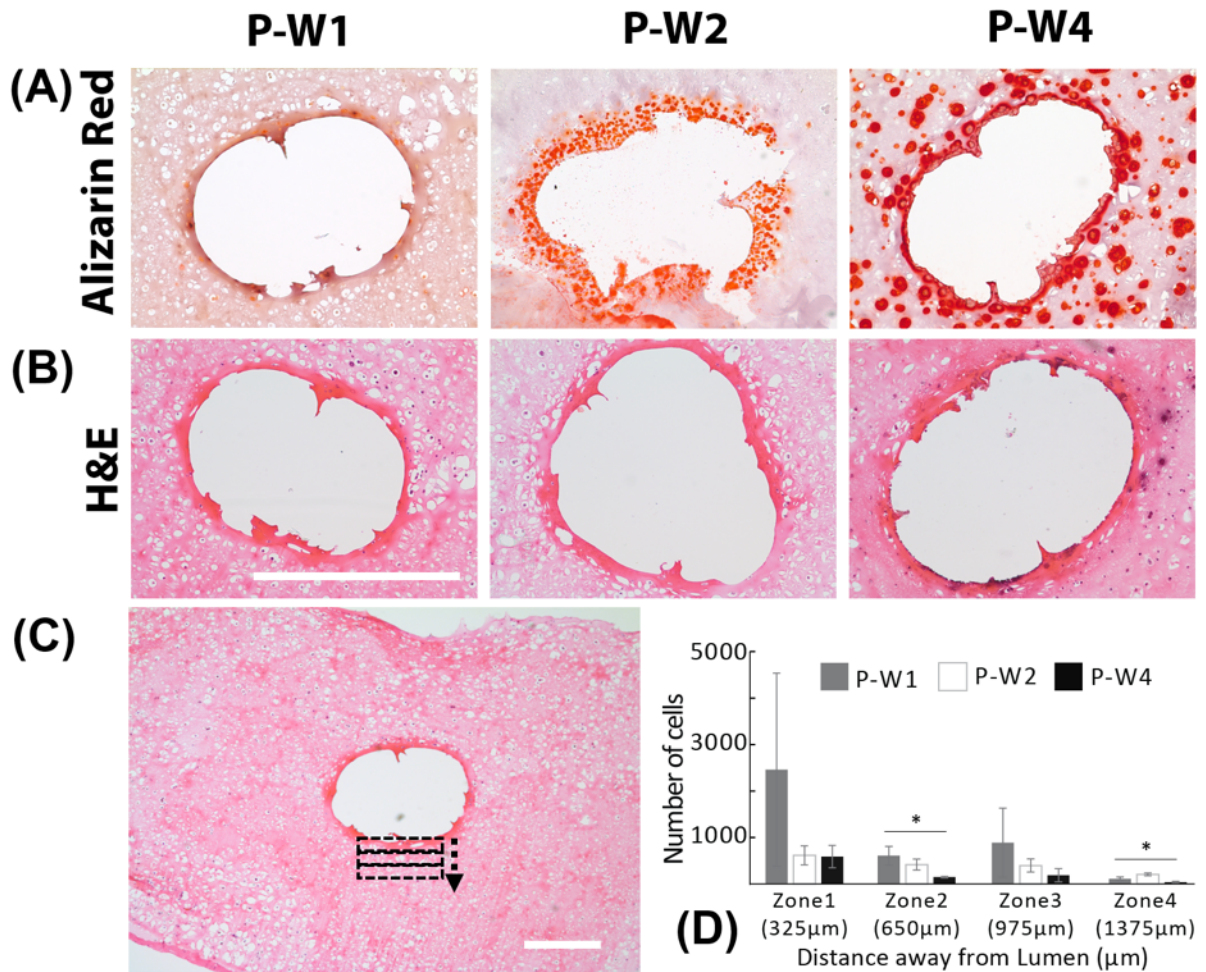


Figure 4.4: Histological analysis of perfused constructs. Cellular localization decreases, and matrix mineralization increases as function of distance from the perfused channels. Representative Alizarin Red (A) and H&E (B) histology stains of construct samples after either 1, 2, or 4 weeks of perfusion with osteogenic media (scale bar: 500μm). Box plot analysis of H&E samples was used to measure cell number in measured increments away from the central pipe (scale bar: 325μm) (C). Histogram quantification of the number of cells as a function of distance away from the lumen for 1, 2 and 4 week perfused samples shows that cell number decreases as the distance from the perfused channel increases (n=3, *p<0.05 via one-way ANOVA) (D).

4.4.5 Construct scalability

To test the scalability of this plug-and-flow approach, an array of 5 dissolvable PVA pipes within a larger ABS construct (11x8x6 mm outer dimension; 6x6x6 mm inner dimension) was 3D printed. The optimal pipe spacing in the larger construct was chosen based on COMSOL simulations of the radial consumption of oxygen around the channels within the cell-laden GelMA matrix (**Fig. 4.5A, B**). Specifically, COMSOL simulations showed that the addition of a second pipe spaced 1mm away would ensure that the lowest oxygen concentration anywhere between the pipes would be approximately 80%, as opposed to 50% and below with only one channel (**Fig. 4.5A-C**). Additionally, the design criteria were chosen to allow for the uncured cell-laden GelMA to conformably flow between the pipes, thereby ensuring there were no air pockets left between the pipes after UV exposure. Based on the analysis, it was determined that 400 μ m channels spaced approximately 1mm apart (edge-to-edge) would ensure that the entire hydrogel matrix between the channels would be adequately supplied with oxygen and other diffusible nutrients (**Fig. 4.5C, D**).

The pipes were placed in three layers spaced 1mm apart in any direction (**Fig. 4.5D**) and the larger construct contained two reservoirs to ensure that all 5 pipes could be perfused via one syringe pump (**Fig. 4.5E**). In order to flow media through the larger system, the original bioreactor design was increased only in the z-direction to highlight the ease of scaling (**Fig. 4.5F**). After 4 weeks of perfusion, micro-CT and alizarin red S staining showed robust mineral deposition along the length of each pipe, as well as between the pipes and along the edges of the bulk construct (**Fig. 4.5 G-D**).

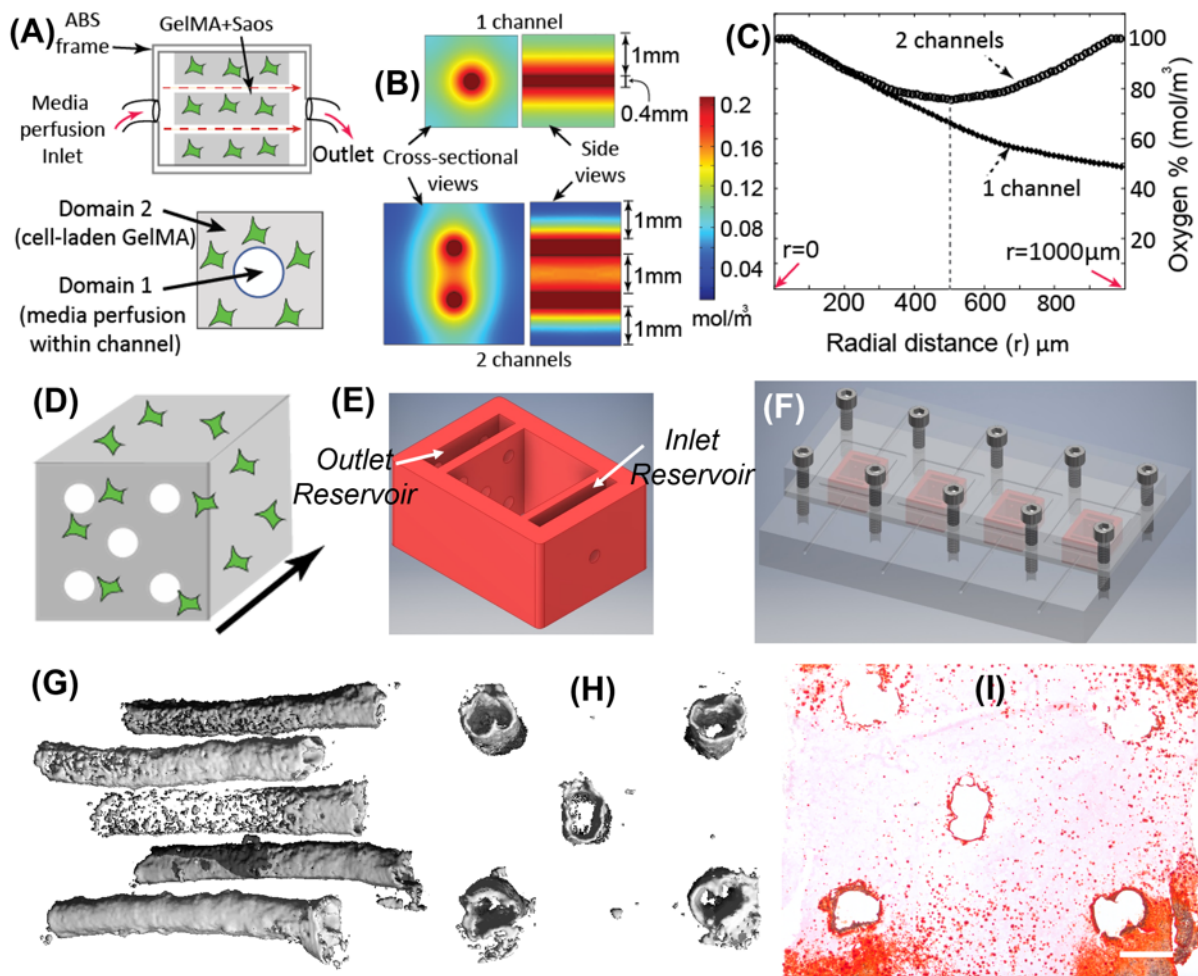


Figure 4.5: Schematic representing the scalability of perfusable constructs. Multiple channels spaced at optimal distances are capable of being perfused via one inlet (A). COMSOL modeling of oxygen diffusion between one channel (B Top) and two channels spaced 1mm apart (B Bottom), as well as COMSOL modeling of the oxygen consumption as a function of radius by cells around the channels within cell laden constructs spaced 1mm apart (C) was used to determine optimal pipe spacing in larger constructs. Schematic of a scaled cell-laden construct (D) and corresponding ABS cage (6x6x6 mm³) (E). CAD isometric view of a machined, two-piece polycarbonate bioreactor containing a PDMS gasket between layers (red) (F). Micro-CT imaging of mineral deposition surrounding pipes (G, side view; H, end view) after four weeks of perfusion

with osteogenic media showed that the model system could be easily scaled. Representative Alizarin Red histology of a large-scale construct after perfusion with osteogenic media for 4 weeks showed robust mineralization (**I**) (scale bar: 500 μ m).

4.4.6 Estimation of the influence of mineral formation on oxygen diffusion

Based on the microCT results, it was clear that the mineral deposited by the encapsulated cells around the channel was not uniform (**Fig. 4.6A**). The annular ring of mineralized crust (**Fig. 4.6B-C**) was porous with several void spaces that contained cell-laden GelMA. To gain insight into the spatial changes in oxygen diffusion due to the deposited mineralized “donut shell” around the channels, a new COMSOL Domain 3 (**Fig. 4.6C**) was introduced in the form of a “donut-shell” with thickness values obtained from Bone J data, and material porosity ($P_{donut-shell}$) values calculated as described in the Methods section (**Fig. 4.6D**). The results were plotted as percent decrease in oxygen concentration radially away from the channel/lumen edge (**Fig. 4.6E**). The results demonstrate that a higher drop in oxygen concentration is possibly due to the formation of mineral.

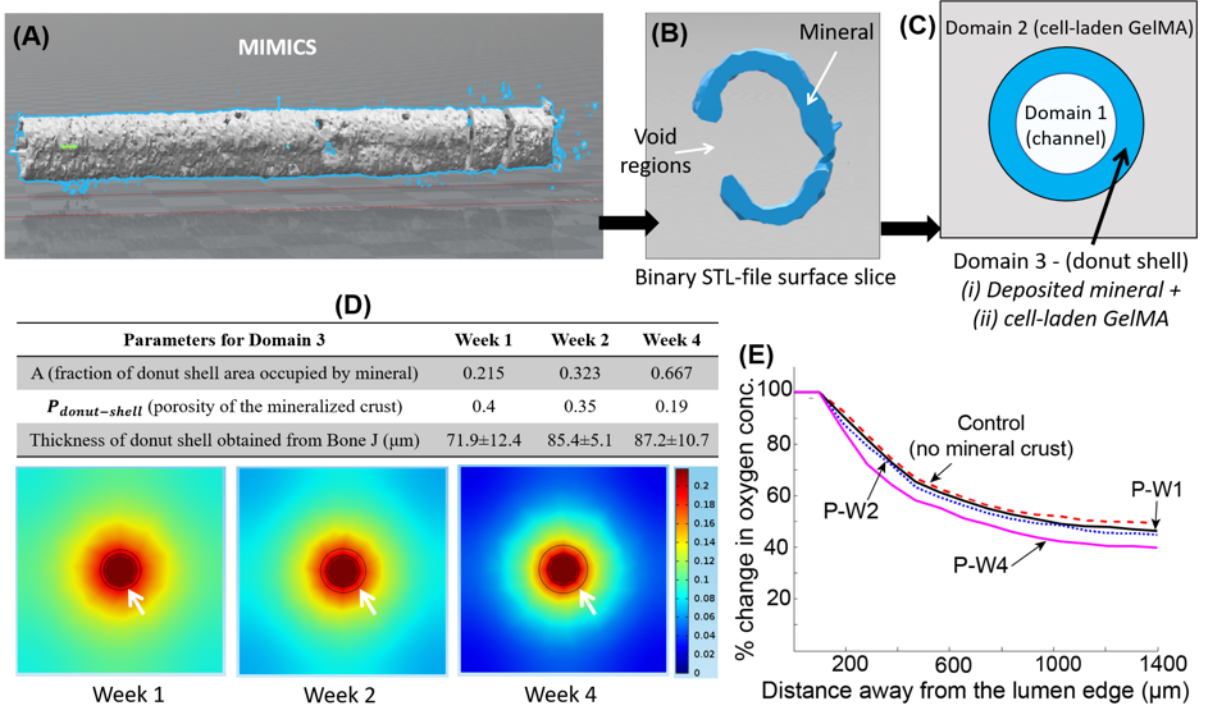


Figure 4.6: Effect of mineral formation on oxygen diffusion radially across the channel. Surface slices were obtained from 3D data sets in MIMICS, and mineral area was measured (A-B). A schematic model showing the three domains used for COMSOL modeling (C). Table shows the various parameters used to calculate Domain 3 (D, Top table). Simulation of oxygen diffusion for weeks 1, 2 and 4 (D, Bottom) (white arrows showing the donut shell thickness). Distribution of oxygen radially away from the channel surface for weeks 1, 2 and 4 along with control without any mineral deposits (E).

4.5 Discussion

Provision of adequate vascular perfusion is one of the most daunting challenges facing the implantation of any tissue engineered construct.[38, 39] Accordingly, over the past decade numerous groups have successfully combined various techniques and sacrificial materials such as pluronics, 3D printed carbohydrates, and 3D printed gels to create vascularized systems, but in

each case the process used was extremely specific to the application being studied.[21, 40, 41] In our plug-and-flow system, however, any component can be readily exchanged and scaled based on the desired application. For instance, the model cell could be replaced with any other osteogenic cell such as patient-derived multipotent marrow stromal cells or autologous osteoblasts. Alternatively, the printed hydrogel could be easily modified via the addition of side groups and growth factors, or could be substituted for a different hydrogel altogether. Furthermore, due to the recent advances in 3D printing technology, numerous different hard and soft materials could be printed simultaneously, allowing for multiple cell types and complex vasculature to be easily incorporated during a single print using only slight modifications to our approach.

For this work, GelMA was chosen as our model hydrogel to encapsulate cells as it is a collagen derivative which contain RGD motifs necessary for cell adhesion, contains readily tunable mechanical properties, and exhibits high structural integrity for experiments lasting over one month.[42, 43] Additionally, previous work has shown that GelMA properties such as diffusion, swelling, compressive moduli, and degree of crosslinking are highly consistent between batches, thereby reducing material variabilities which could affect experimental outcomes.[44-46] Furthermore, GelMA is capable of being UV crosslinked with minimal negative side effects to the encapsulated cells.[47, 48] PVA was chosen to be the sacrificial material and ABS was chosen to be the structural frame for our model system due to the fact that they both are commercially available thermoplastics capable of being printed at high fidelities using common 3D printers. The selection of PVA allows for the possibility of printing user-defined channel-patterns for more complex tissue structures. Additionally, post-processing removal of PVA from the system is also simplified as PVA is water soluble, thereby reducing the possibility for external contaminants to be introduced into the system via manual pipe removal. In this model a flow rate of 0.2 ml/hour

was used, a rate well below what would be needed in a larger construct containing primary cells.[49-51] The decision to use this lower rate was made, however, based on previous work that has shown how higher flow rates in *in vitro* bioreactor systems have led to significant increases in cell death and reduced cell proliferation.[52] However, as the flow in this system is driven by a programmable syringe pump, further studies would easily be able to address this issue.

It is known that mineralized matrix (in this case mineralized GelMA) is conducive to the diffusion of small solutes through interstitial spaces, albeit in the sub-nanometer range that cannot be observed with microCT. After 2 and 4 weeks of perfusion, large voids in the deposited mineral were observed (**Fig. 4.2E**) that would allow for the diffusion of oxygen and other nutrients even after the formation of the mineralized crust. From the Live/Dead results (**Fig. 4.2C**), live cells could be seen outside the mineralized crust, indicating that diffusion of essential nutrients took place even after mineral formation. However, the crust did appear to inhibit the oxygen concentration away from the perfused pipes to a degree, as was qualitatively explained via COMSOL modeling (**Fig. 4.6**).

This work represents a simple bioreactor system capable of inducing cell-mediated mineral deposition around perfusable channels. However, more work needs to be performed to create a completely mineralized thick bone construct as was indicated by the lack of mineralization between the pipes. The modularity of this model system allows for the incorporation of other cell types as well as the perfusion of growth factors with pulsatile perfusion conditions. One direction to enhance overall mineral formation is the co-encapsulation of vascular endothelial cells with bone cells in this system to facilitate the formation of perfusable microvasculature between printed channels. Increased perfusion rates as well as the incorporation of pulsatile flow and specific

growth factors can also be optimized within this model system. While long-term studies building upon the foundation of this model are necessary, this work provides early evidence that 3D printed, cell-laden hydrogels containing user defined channels can be used as a model system for bone tissue engineering applications.

4.6 Conclusions

Our study demonstrated that user-defined 3D printed channels could be used to promote mineral deposition within a diffusion-limited environment using commonly available 3D printers, sacrificial materials, and hydrogels. Based on these results, we anticipate that this technology could be easily scaled and reproduced in order to create thick, cell-laden constructs capable of serving as vascularized bone tissue substitutes, as well as be translated to other tissue engineering applications.

4.7 Non-Author Acknowledgements

We would like to thank Dr. Megan Oest with her help obtaining data from the microCT. Additionally, this work was supported by the CMMI 1547095, and (IGERT) DMR-DGE-1068780 at Syracuse University, funded by the National Science Foundation (NSF).

4.8 Disclosure statement

There are no competing financial interests pertaining to this work.

4.9 References

1. Sawyer, S.W., et al., *Perfusion directed 3D mineral formation within cell-laden hydrogels*. *Biofabrication*, 2018. **10**(3).
2. Bae, H., et al., *Building vascular networks*. *Science Translational Medicine*, 2012. **4**(160).
3. Kaully, T., et al., *Vascularization—the conduit to viable engineered tissues*. *Tissue Engineering Part B: Reviews*, 2009. **15**(2): p. 159-169.
4. Nichol, J.W. and A. Khademhosseini, *Modular tissue engineering: engineering biological tissues from the bottom up*. *Soft Matter*, 2009. **5**(7): p. 1312-1319.
5. Lovett, M., et al., *Vascularization strategies for tissue engineering*. *Tissue Engineering Part B: Reviews*, 2009. **15**(3): p. 353-370.
6. Volkmer, E., et al., *Hypoxia in static and dynamic 3D culture systems for tissue engineering of bone*. *Tissue Engineering Part A*, 2008. **14**(8): p. 1331-1340.
7. Yeatts, A.B. and J.P. Fisher, *Bone tissue engineering bioreactors: dynamic culture and the influence of shear stress*. *Bone*, 2011. **48**(2): p. 171-181.
8. Hutmacher, D.W., *Scaffolds in tissue engineering bone and cartilage*. *Biomaterials*, 2000. **21**(24): p. 2529-2543.
9. Mikos, A.G. and J.S. Temenoff, *Formation of highly porous biodegradable scaffolds for tissue engineering*. *Electronic Journal of Biotechnology*, 2000. **3**(2): p. 23-24.
10. Loh, Q.L. and C. Choong, *Three-dimensional scaffolds for tissue engineering applications: role of porosity and pore size*. *Tissue Engineering Part B: Reviews*, 2013. **19**(6): p. 485-502.

11. Smith, I., et al., *Nanostructured polymer scaffolds for tissue engineering and regenerative medicine*. Wiley Interdisciplinary Reviews: Nanomedicine and Nanobiotechnology, 2009. **1**(2): p. 226-236.
12. Hutmacher, D.W., M. Sittinger, and M.V. Risbud, *Scaffold-based tissue engineering: rationale for computer-aided design and solid free-form fabrication systems*. Trends in Biotechnology, 2004. **22**(7): p. 354-362.
13. Annabi, N., et al., *25th anniversary article: Rational design and applications of hydrogels in regenerative medicine*. Advanced Materials, 2014. **26**(1): p. 85-124.
14. Antoniac, I., et al., *Exploring the Future of Hydrogels in Rapid Prototyping: A Review on Current Trends and Limitations*, in *Biologically Responsive Biomaterials for Tissue Engineering*. 2013, Springer New York. p. 201-249.
15. Khademhosseini, A. and R. Langer, *Microengineered hydrogels for tissue engineering*. Biomaterials, 2007. **28**(34): p. 5087-5092.
16. Lee, K. and D. Mooney, *Hydrogels for tissue engineering*. Chem Rev, 2001. **101**(7): p. 1869-79.
17. Slaughter, B.V., et al., *Hydrogels in regenerative medicine*. Advanced Materials, 2009. **21**(32-33): p. 3307-3329.
18. Tibbitt, M.W. and K.S. Anseth, *Hydrogels as extracellular matrix mimics for 3D cell culture*. Biotechnology and Bioengineering, 2009. **103**(4): p. 655-663.
19. Kloxin, A.M., M.W. Tibbitt, and K.S. Anseth, *Synthesis of photodegradable hydrogels as dynamically tunable cell culture platforms*. Nature Protocols, 2010. **5**(12): p. 1867-1887.
20. Lewis, K.J. and K.S. Anseth, *Hydrogel scaffolds to study cell biology in four dimensions*. MRS Bulletin, 2013. **38**(03): p. 260-268.

21. Kolesky, D.B., et al., *Three-dimensional bioprinting of thick vascularized tissues*. Proceedings of the National Academy of Sciences, 2016. **113**(12): p. 3179-3184.
22. Zhang, Y., et al., *Characterization of printable cellular micro-fluidic channels for tissue engineering*. Biofabrication, 2013. **5**(2): p. 025004.
23. Wüst, S., R. Müller, and S. Hofmann, *3D Bioprinting of complex channels—Effects of material, orientation, geometry, and cell embedding*. Journal of Biomedical Materials Research Part A, 2015. **103**(8): p. 2558-2570.
24. Duan, B., *State-of-the-art review of 3D bioprinting for cardiovascular tissue engineering*. Annals of Biomedical Engineering, 2017. **45**(1): p. 195-209.
25. Elomaa, L. and Y.P. Yang, *Additive manufacturing of vascular grafts and vascularized tissue constructs*. Tissue Engineering Part B: Reviews, 2017.
26. Arcaute, K., B.K. Mann, and R.B. Wicker, *Stereolithography of three-dimensional bioactive poly (ethylene glycol) constructs with encapsulated cells*. Annals of Biomedical Engineering, 2006. **34**(9): p. 1429-1441.
27. Bajaj, P., et al., *3D biofabrication strategies for tissue engineering and regenerative medicine*. Annual Review of Biomedical Engineering, 2014. **16**: p. 247-276.
28. Raman, R. and R. Bashir, *Stereolithographic 3D bioprinting for biomedical applications*, in *Essentials of 3D Biofabrication and Translation*. 2015, Elsevier. p. 89-121.
29. Albrecht, L.D., S.W. Sawyer, and P. Soman, *Developing 3D scaffolds in the field of tissue engineering to treat complex bone defects*. 3D Printing and Additive Manufacturing, 2016. **3**(2): p. 106-112.
30. Rodan, S.B., et al., *Characterization of a human osteosarcoma cell line (Saos-2) with osteoblastic properties*. Cancer Research, 1987. **47**(18): p. 4961-4966.

31. Doube, M., et al., *BoneJ: free and extensible bone image analysis in ImageJ*. Bone, 2010. **47**(6): p. 1076-1079.
32. Athirasala, A., et al., *A Novel Strategy to Engineer Pre-Vascularized Full-Length Dental Pulp-like Tissue Constructs*. Scientific Reports, 2017. **7**(33): p. 23.
33. Kipnis, D.M. and C. Cori, *Studies of tissue permeability*. V. The penetration and phosphorylation of 2-deoxyglucose in the rat diaphragm. Journal of Biological Chemistry, 1959. **234**: p. 171-177.
34. Chapra, S.C., *Surface water-quality modeling*. 2008. Waveland press.
35. Heppenstall, R.B., G. Grislis, and T.K. Hunt, *Tissue gas tensions and oxygen consumption in healing bone defects*. Clinical Orthopaedics and Related Research, 1975. **106**: p. 357-365.
36. Renders, G., et al., *Porosity of human mandibular condylar bone*. Journal of Anatomy, 2007. **210**(3): p. 239-248.
37. Mercado-Pagán, Á.E., et al., *Vascularization in bone tissue engineering constructs*. Annals of Biomedical Engineering, 2015. **43**(3): p. 718-729.
38. Lee, J.B., et al., *Development of 3D microvascular networks within gelatin hydrogels using thermoresponsive sacrificial microfibers*. Advanced Healthcare Materials, 2016. **5**(7): p. 781-785.
39. Bertassoni, L.E., et al., *Hydrogel bioprinted microchannel networks for vascularization of tissue engineering constructs*. Lab on a Chip, 2014. **14**(13): p. 2202-2211.
40. Miller, J.S., et al., *Rapid casting of patterned vascular networks for perfusable engineered three-dimensional tissues*. Nature Materials, 2012. **11**(9): p. 768-774.
41. Byambaa, B., et al., *Bioprinted Osteogenic and Vasculogenic Patterns for Engineering 3D Bone Tissue*. Advanced Healthcare Materials, 2017. **6**: p. 1700015.

42. Chen, Y.X., et al., *A novel suspended hydrogel membrane platform for cell culture*. Journal of Nanotechnology in Engineering and Medicine, 2015. **6**(2): p. 021002.
43. Sawyer, S., et al., *Behavior of Encapsulated Saos-2 Cells within Gelatin Methacrylate Hydrogels*. J Tissue Sci Eng, 2016. **7**(173): p. 2.
44. Yue, K., et al., *Synthesis, properties, and biomedical applications of gelatin methacryloyl (GelMA) hydrogels*. Biomaterials, 2015. **73**: p. 254-271.
45. Chen, Y.X., B. Cain, and P. Soman, *Gelatin methacrylate-alginate hydrogel with tunable viscoelastic properties*. Aims Materials Science, 2017. **4**(2): p. 363-369.
46. Sawyer, S.W., et al., *Conductive gelatin methacrylate-poly (aniline) hydrogel for cell encapsulation*. Biomedical Physics & Engineering Express, 2017. **4**(1): p. 015005.
47. Kumar, D., et al., *Three-dimensional hypoxic culture of human mesenchymal stem cells encapsulated in a photocurable, biodegradable polymer hydrogel: a potential injectable cellular product for nucleus pulposus regeneration*. Acta Biomaterialia, 2014. **10**(8): p. 3463-3474.
48. Chung, C., et al., *Influence of gel properties on neocartilage formation by auricular chondrocytes photoencapsulated in hyaluronic acid networks*. Journal of Biomedical Materials Research Part A, 2006. **77**(3): p. 518-525.
49. Buckwalter, J., et al., *Bone biology*. J Bone Joint Surg Am, 1995. **77**(8): p. 1256-1275.
50. McCarthy, I., *The physiology of bone blood flow: a review*. The Journal of Bone & Joint Surgery, 2006. **88**(suppl 3): p. 4-9.
51. Laroche, M., *Intraosseous circulation from physiology to disease*. Joint Bone Spine, 2002. **69**(3): p. 262-269.
52. Cartmell, S.H., et al., *Effects of medium perfusion rate on cell-seeded three-dimensional bone constructs in vitro*. Tissue Engineering, 2003. **9**(6): p. 1197-1203.

4.10 Supplementary figures

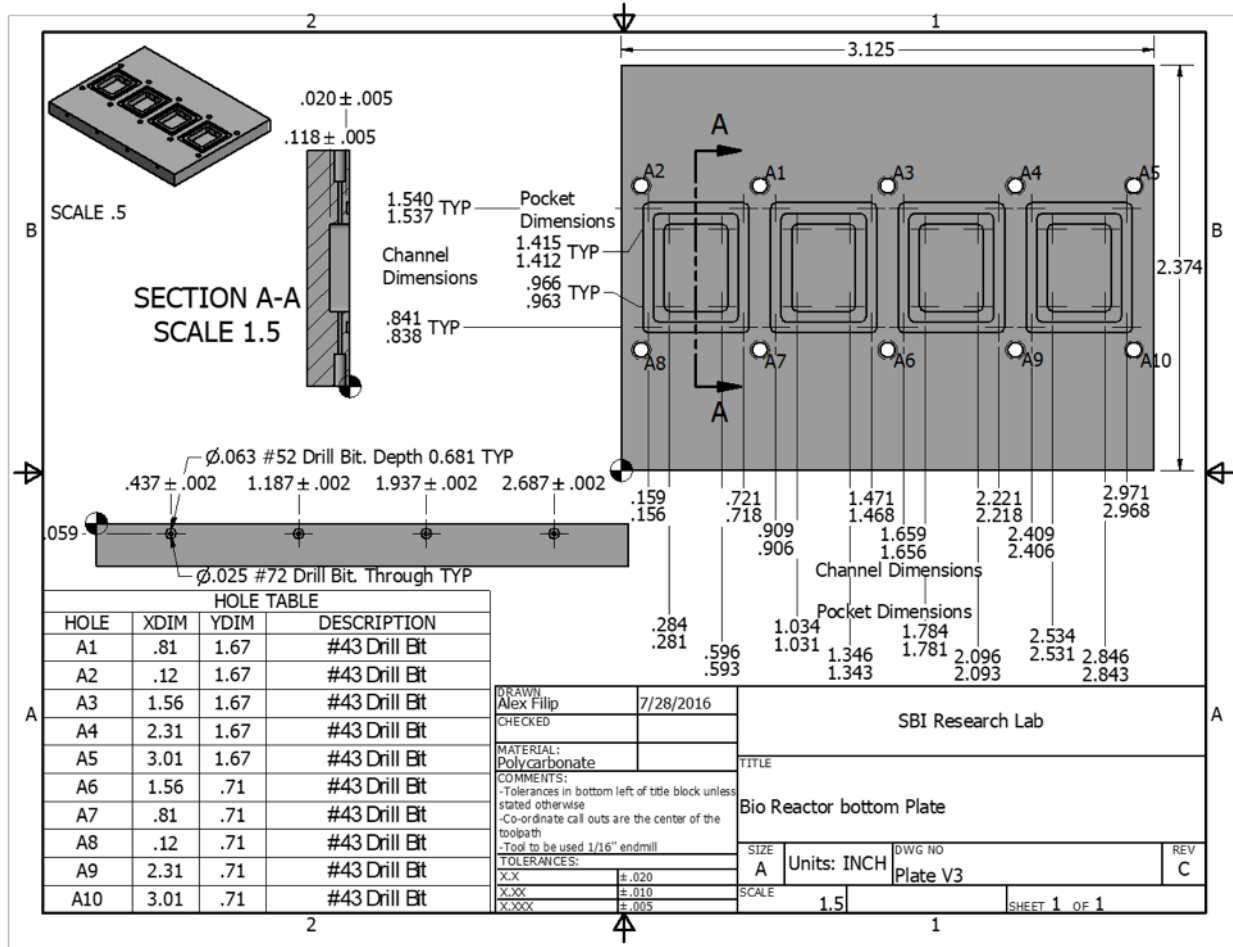


Figure S4.1: Polycarbonate base plate dimensions and scale.

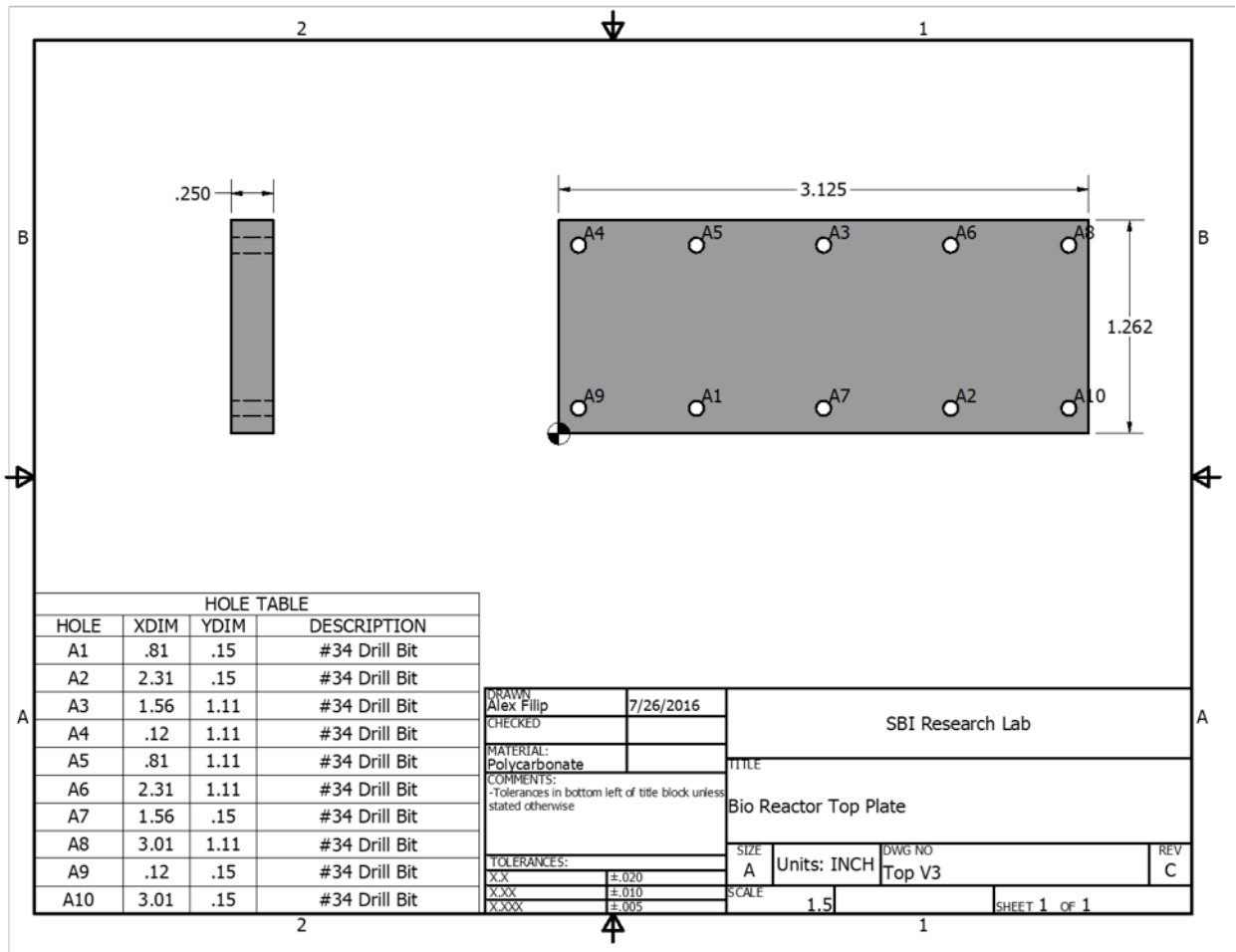


Figure S4.2: Polycarbonate top plate dimensions and scale.

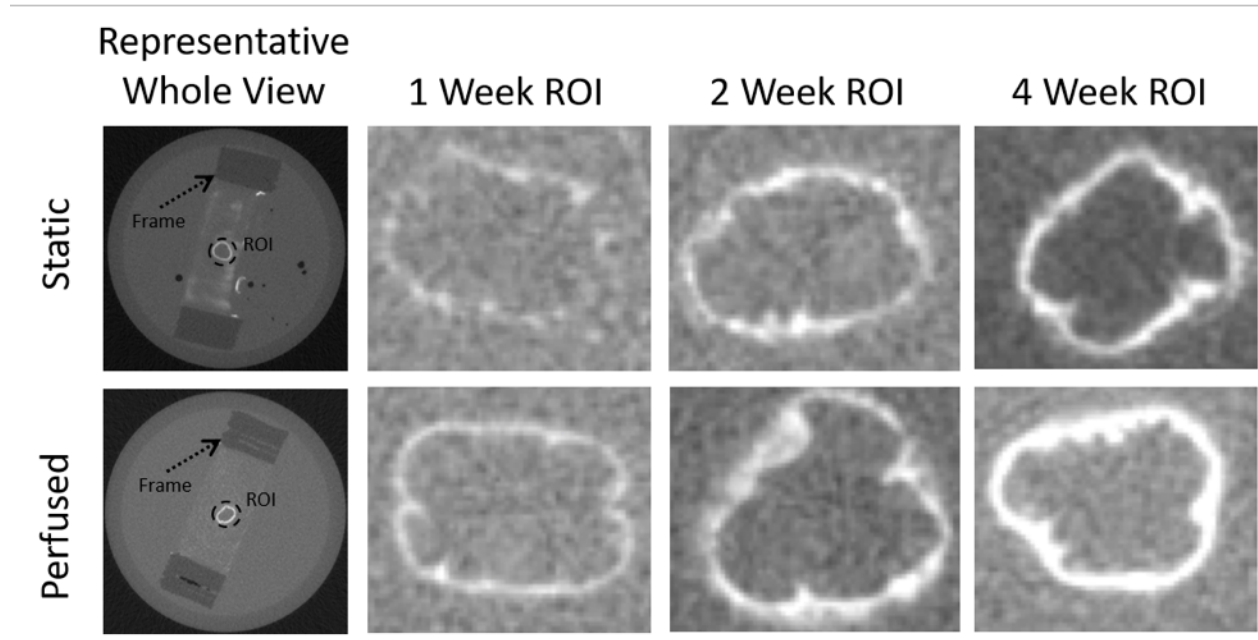


Figure S4.3: Representative series of static and perfused images showing contrast of deposited mineral from background and frames after microCT scanning. Representative whole views of in-tact constructs within 16mm diameter sample holders after scanning show contrast of deposited mineral (white) from background (grey) and sample frames (dark grey). To normalize data, only mineralized pipes were contoured for mineral (ROI).

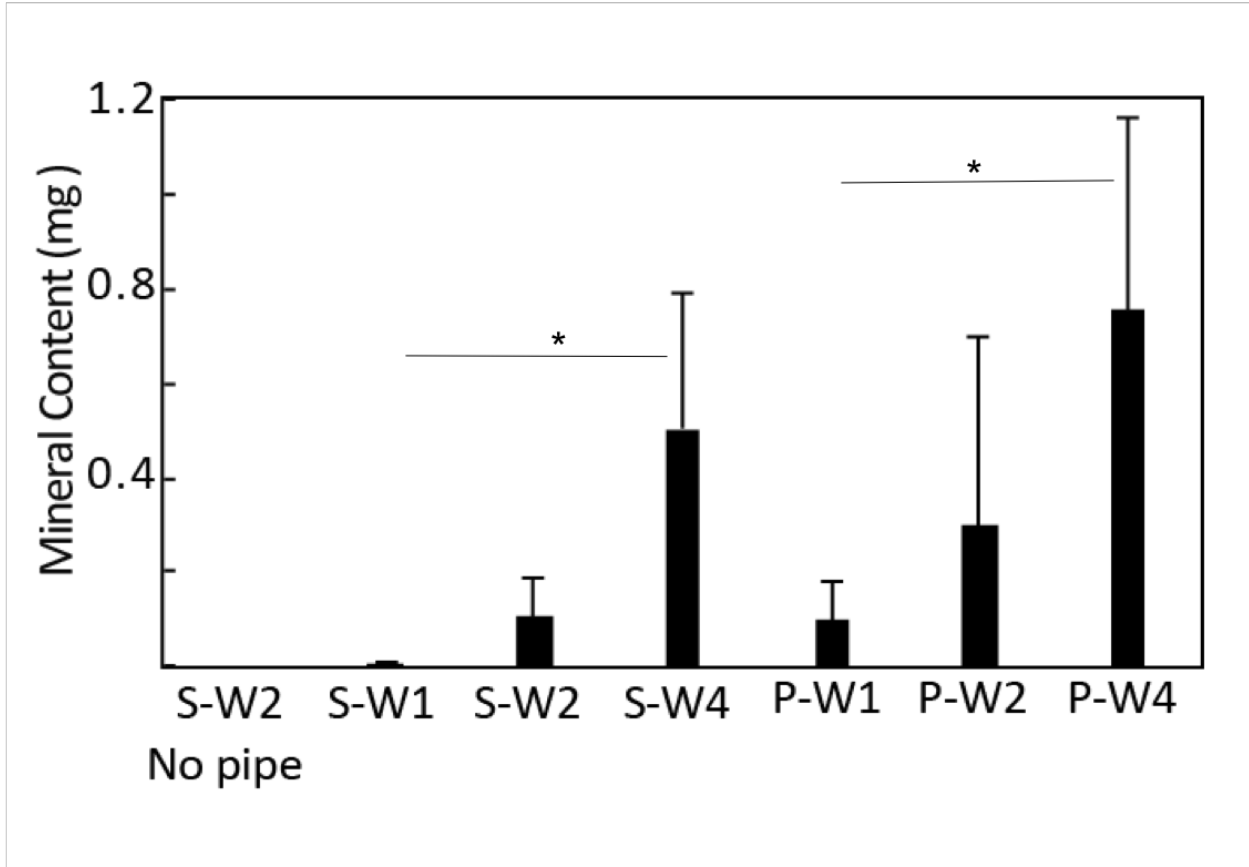


Figure S4.4: Total mineral quantification. Total mineral deposited around pipes after 1, 2, or 4 weeks of both static osteogenic culture and osteogenic media perfusion showed significant increases in deposition after 4 weeks (4wk static and 4wk flow n=7, 2wk flow n=8, rest n=6. * p<0.05 via one-way ANOVA).

CHAPTER 5: ONGOING WORK AND FUTURE RECOMMENDATIONS

5.1 Introduction

The overarching goal of this work was to create a model bone tissue engineering construct that would support the numerous cellular interactions required for bone growth, provide potential structural support, and allow for nutrients to be delivered in a controlled, precise fashion via a user-defined internal vasculature. To achieve this goal, it was first necessary to identify a suitable soft matrix for cellular encapsulation and sustainable viability. After identifying the soft matrix for cellular encapsulation, a way to combine the soft, cell-laden matrix with a hard, 3D printed structural support needed to be explored. Finally, after combining the soft and hard components, the incorporation of a user defined perfusable vasculature was studied.

In Chapter 2 of this work, osteoblast-like cells were encapsulated in GelMA hydrogels of varying density and chemically induced to produce mineral over the course of two weeks. Although cells in the less dense gels had a higher overall viability and formed larger cellular clusters within the GelMA matrix, cells encapsulated within the denser constructs appeared to form more uniform mineral at the hydrogel periphery. Moving forward, the dense gels were chosen to be more suitable as the base material for a model bone tissue engineering construct based on the mineralization results and literature suggesting that stiffer substrates promoted osteogenic differentiation and increased cell mediated mineralization.[1, 2] However, based on the results from Chapter 4 of this work, the lack of pericellular material deposition between perfusable pipes could have been mitigated if the less dense hydrogels were used as the base material.

In Chapter 3 of this work, three different types of structural cages were 3D printed to serve as potential structural supports for the soft, cell-laden GelMA. This chapter compared polycaprolactone (PCL) cages, polycaprolactone-hydroxyapatite (PCL-HA) composite cages, and polycaprolactone-poly lactic acid (PCL-PLA) composite cages and found that of the three, the PCL-PLA cages had the highest compressive strength. However, none of the cages surpassed the compressive strength of a pure PLA cage alone. Additionally, the print resolutions of the PLA cages were significantly higher than the PCL and PCL composites. As a result, pure thermoplastic cages were chosen to be the supporting material for the cell-laden hydrogels going forward. While PLA cages would have been optimal, purchasing issues required the use of acrylonitrile butadiene styrene (ABS) thermoplastic spools as a substitute for PLA.

At the end of Chapter 3 it was shown that the cell-laden GelMA studied in Chapter 2 could be incorporated within the 3D printed cages via dropwise pipetting. However, based on the live/dead imaging, it was hypothesized that the cellular density of living cells was not uniform throughout the entirety of the log-pile structure, most likely due to nutrient diffusion limitations in the center of the construct. Accordingly, in Chapter 4 of this work it was decided that in order to increase cellular distribution throughout the construct and mitigate the hypothesized diffusion limitations, the 3D printed cage would not be log-pile in form but instead consist of an outside frame containing dissolvable 3D printed polyvinyl alcohol (PVA) pipes. Upon casting the cell-laden GelMA into the 3D printed frame, the pipes were dissolved, leaving behind a fully perfusable, structurally supported cell-laden hydrogel. However, sacrificing the log-pile structure for a rectangular cage would need to be addressed in any future work should the printed structure be used as a load-bearing *in vivo* support.

While the structurally supported hydrogels from Chapter 4 could be perfused with osteogenic media for 1 month, the mineral deposition along the channel walls appeared to impede oxygen transfer into the surrounding GelMA matrix. Furthermore, although the constructs could be scaled up into larger, 5 pipe arrays, little to no mineralization occurred between the channels. As suggested previously, any future work would need to address the issue of mineralization between the perfusable pipes, most likely by changing the density of the hydrogel used to encapsulate the osteogenic cells.

5.2 The addition of endothelial cells to the perfusable system

Generally, monoculture systems for bone growth tend to be supplemented with growth factors like vascular endothelial growth factor (VEGF), basic fibroblast growth factor (bFGF), and bone morphogenetic protein (BMP). However, while these supplements have been shown to promote mineralization and the formation of vasculature, they are prohibitively expensive and unwanted side effects such as *in vitro* tumor growth are common.[3-6] Accordingly, as vascularization of the bone tissue constructs is desired, an alternative approach is to incorporate endothelial cells in the construct alongside osteogenic cells.[7-9]

It has been shown that co-cultures of endothelial and osteogenic cells within tissue engineered constructs promote increased mineral deposition and vasculature creation.[10-12] Autocrine and paracrine signaling between osteoblasts and endothelial cells is primarily modulated through the release of VEGF by osteoblasts and direct contact through gap junctions.[12-14] The release of VEGF has been shown to stimulate vasculature formation through the recruitment of endothelial cells, which in turn has a complementary effect on osteoblasts as endothelial cells release pro-

osteogenic cytokines such as BMP-2 and endothelin-1 that directly support osteoblast differentiation and mineralization.[15-19]

Lining premade channels with endothelial cells is a common approach when making a vascularized tissue engineered construct, and seeded cells have shown the capability of forming a confluent cellular sheet along the channel lumens which selectively allow nutrients to pass into the bulk material.[20, 21] Alternatively, encapsulated endothelial cells within hydrogels between premade vasculature channels have shown a high potential for vasculature creation in *in vitro* settings.[22] In one instance, encapsulated HUVECS within collagen gels rearranged into cords over the course of only 10 hours,[23] while HUVECS embedded within a fibrin gel containing supportive fibroblasts showed capillary formation between two larger, perfusable channels.[24]

To investigate the addition of HUVECS in the model system presented in Chapter 4 of this work, HUVECS were either lined within the perfusable channels and surrounded by Saos-2 cells in the bulk GelMA or were added with the Saos-2 cells in a 2:1 ratio in the bulk (**Fig. 5.1**). In order to line the channels with HUVECS, a cell suspension containing 25,000 HUVECS was pipetted dropwise into the channel, left to stand for 30 minutes, and repeated after flipping the construct. After two weeks of perfusion, channels lined with HUVECS had stunted mineral formation, while HUVECS added into the bulk significantly enhanced mineral deposition.

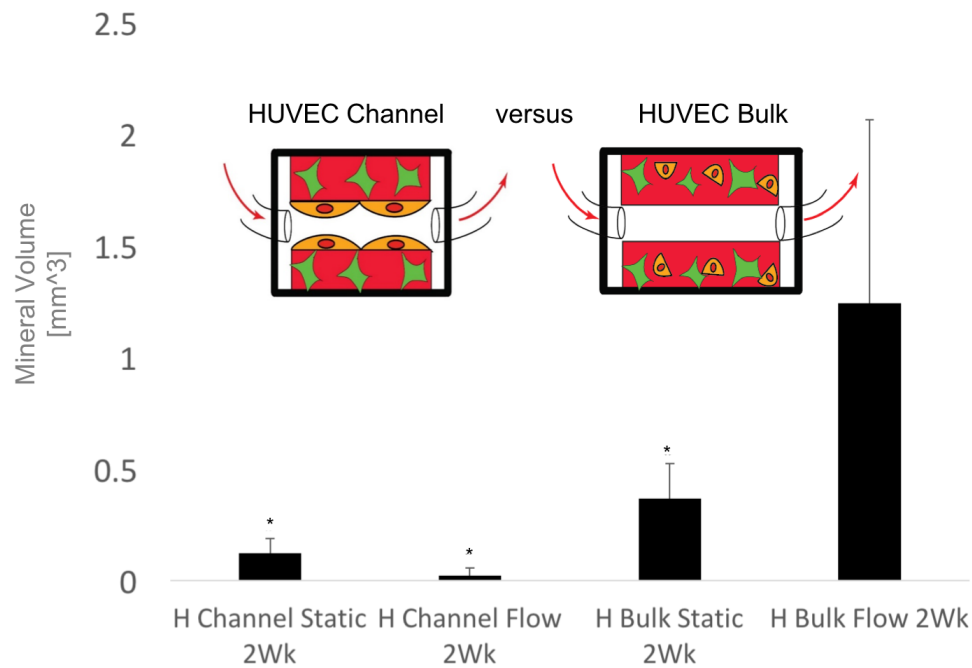


Figure 5.1: MicroCT analysis of mineral deposition within a co-culture single pipe system. HUVECS (H) were either seeding along the perfusable channels (Channel) or added in a 2:1 ratio with Saos-2 cells in the GelMA matrix (Bulk) and were either perfused with osteogenic media (Flow) or left in static control wells (Static). After two weeks of perfusion, HUVECS encapsulated in the bulk material significantly increased Saos-2 mineral deposition as compared to the constructs containing HUVEC lined channels and their static controls (* $p < 0.05$ as compared to H Bulk Flow 2Wk, $n=5$).

Due to the results presented in **Fig. 5.1**, the next step in expanding upon the model system described in this thesis is to encapsulate the osteoblast-like Saos-2 cells alongside HUVEC cells in a multi-pipe system in an attempt to enhance mineralization within the bulk GelMA between channels. To that end, preliminary work has been performed in an expanded two pipe perfusable system similar to the model presented in Chapter 4. Specifically, the one pipe system described

earlier has been extended to two pipes spaced 1mm apart in the x-y plane surrounded by a bulk GelMA matrix containing encapsulated Saos-2 cells and HUVECS (**Fig. 5.2**). In the preliminary work, either HUVECS, Saos-2 Cells, or HUVECS with Saos-2 cells were encapsulated within a GelMA matrix and perfused with osteogenic media for either 1 or 2 weeks. HUVECS and Saos-2 cells were encapsulated at a 2:1 ratio (1 million HUVECS : 500,000 Saos-2). After two weeks of perfusion, there was no significant increase in the mineral deposited in the Saos-2 only or Saos-2/HUVEC constructs, however both had significantly more mineral deposition as compared to the one-week samples. However, as the mineral recorded was the total mineral deposited in the entire construct, future work would include isolating only the mineral produced between the channels in order to quantify how HUVECS affect mineral formation between two nutrient supplies.

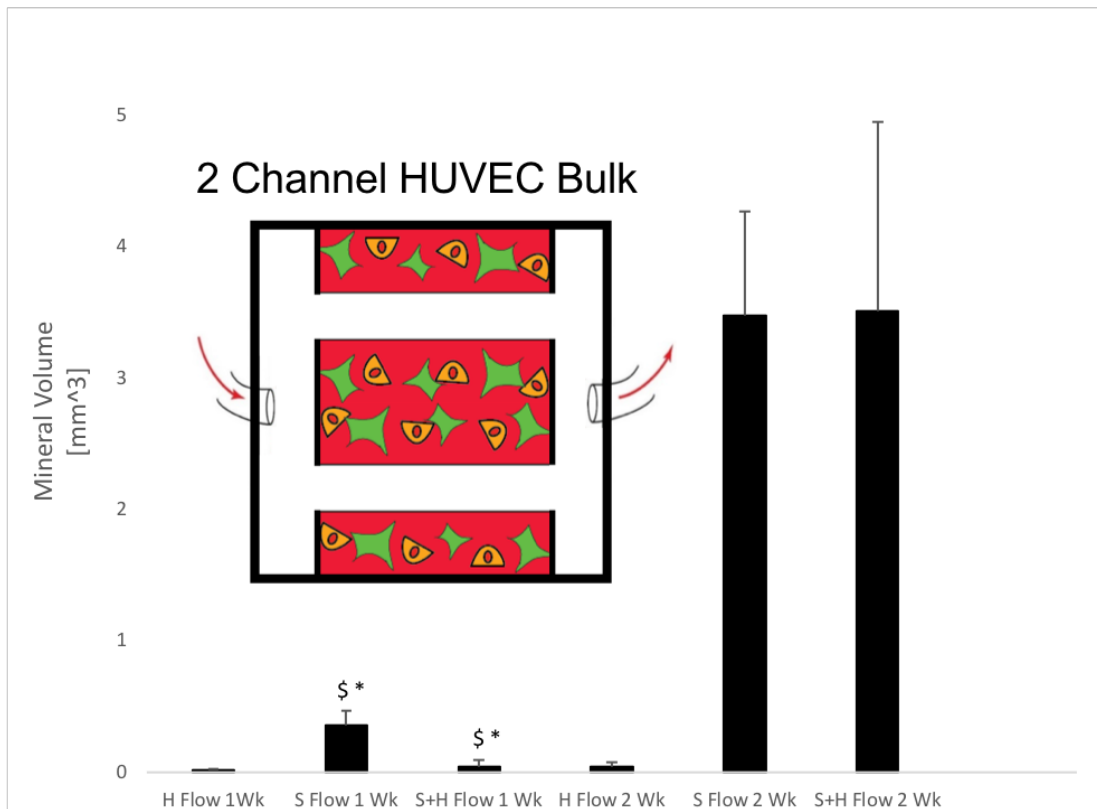


Figure 5.2: MicroCT analysis of mineral deposition within a co-culture double pipe system.

HUVECS (H) were added in a 2:1 ratio with Saos-2 cells (S) in the GelMA matrix and perfused with osteogenic media for either 1 or 2 weeks. After two weeks of perfusion, HUVEC+Saos-2

constructs did not show a significant increase in mineral deposition as compared to samples containing only Saos-2 cells. (*p<0.05 as compared to S+H Flow 2Wk; \$p<0.05 as compared to S Flow 2Wk; n=3 for HUVEC only samples, n=5 for rest).

5.3 In vivo extension of model system

The integration with host tissue remains a major obstacle facing any tissue engineered construct.[25-27] In general, for complete integration to occur in an *in vivo* setting, any engineered construct needs to be biocompatible and show minimum immunogenicity.[28] Furthermore, the challenge of either anastomosing or inosculating the construct with the host vasculature is a lengthy process that often results in implant failure, tissue necrosis, site inflammation, and local ischemia.[13, 29]

Most work on integrating an implant with the host has relied on letting the host's vasculature passively grow into the implant. Unfortunately, approaches such as these could take many days to occur and complete anastomosis with the host is highly dependent on the geometry of the implant's vasculature.[23, 30]

In order to assess the biocompatibility of the model system presented in this work, preliminary ectopic implantation experiments were undertaken using our perfused constructs. Specifically, 6x6x6mm³ ABS frames were printed to house GelMA hydrogels containing primary mouse bone marrow skeletal stem cells (BMSC) and primary mouse vasculature endothelial cells (VEC). The constructs were subsequently implanted subcutaneously in the dorsal pockets of C57BL/6J mice and retrieved after two weeks of implantation (**Fig. 5.3**). As was expected, the constructs did show

some host ingrowth and blood invasion, as well as no signs of tissue inflammation or infection. Unfortunately, the constructs were inadvertently destroyed during the fixation and subsequent paraffin embedding process for histology, making the types of host ingrowth and cellular invasion impossible to elucidate.

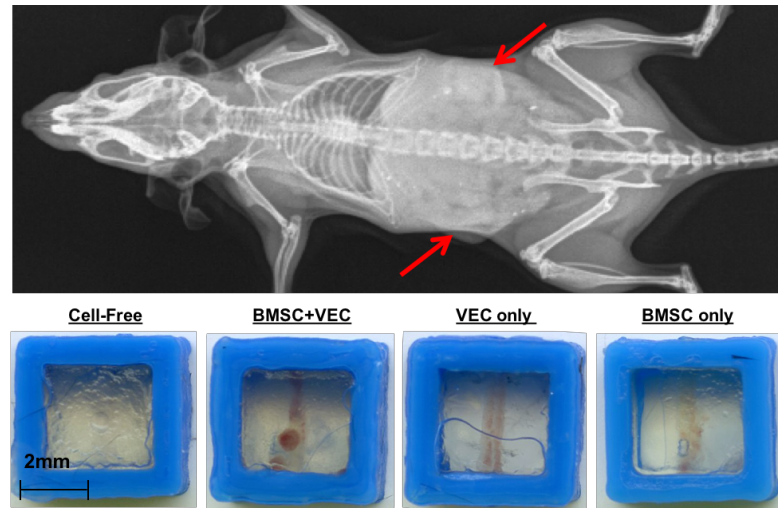


Figure 5.3: Ectopic implantation of thermoplastic ABS frames containing primary BMSC and VEC cells. $6 \times 6 \times 6 \text{mm}^3$ frames containing encapsulated BMSCs, VECs, or a combination of both were implanted subcutaneously in c57BL/6J mice (red arrows, top X-ray). After two weeks of implantation, the implants were retrieved and showed blood invasion and minimal host ingrowth in the cell-laden constructs (bottom).*

Based on the results of the preliminary ectopic implantation experiments, future work would be aimed at directly anastomosing the implant's vasculature with the hosts blood supply (**Fig. 5.4**). Direct anastomosis would ensure that the perfusion of nutrients occurs at the time of implantation, thereby reducing the chance for implant failure and increasing the potential for host integration and encapsulated cell osteogenesis.[28] However, as stated previously, the direct anastomosis

* All animal studies were performed at SUNY Upstate Medical University by Dr. Jason Horton under established and approved IACUC protocol.

process is highly risky and difficult, requiring extended practice and planning prior to implementation.

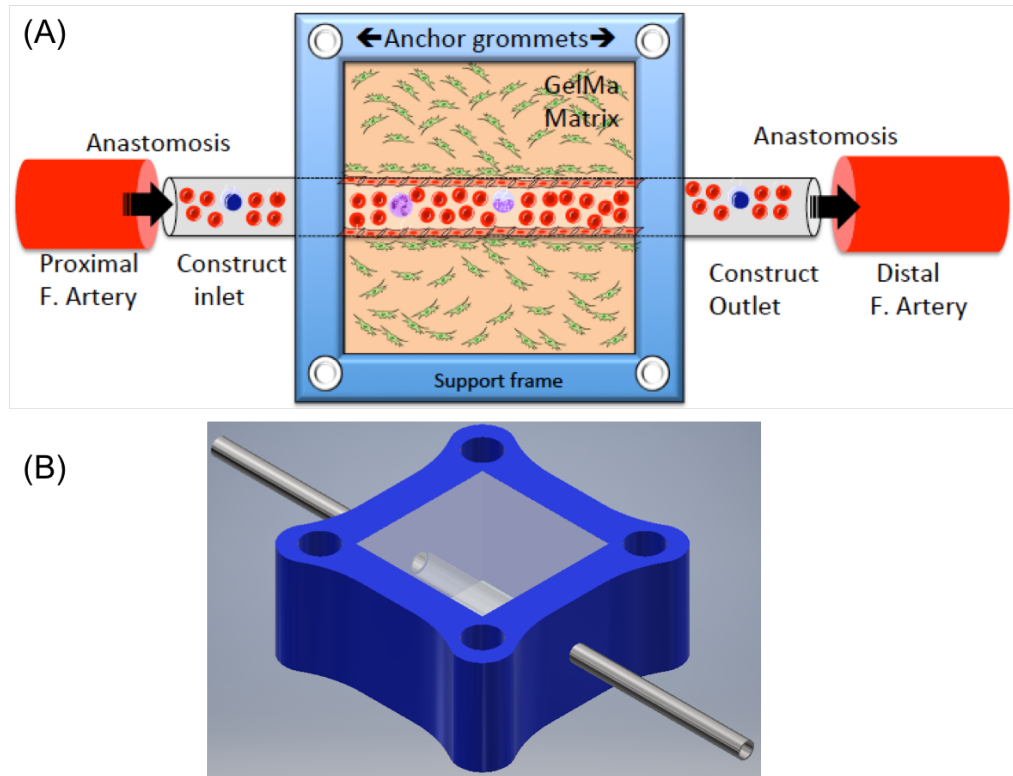


Figure 5.4: Cartoon depicting surgical anastomosis of perfusable structurally supported cell-laden constructs. (A) 3D printed constructs containing cell-laden GelMA and perfusable channels will be anastomosed directly into the host femoral artery and sewn in place via 3D printed anchor grommets. **(B)** 3D rendering of structural frame (blue) and stainless-steel catheter connections (grey).*

* Cartoon created by and used with permission from Dr. Jason Horton, SUNY Upstate Medical University.

5.4 Final Remarks

This work has focused on creating a bone tissue engineering construct which could eventually serve as an *in vivo* implant to aid in regenerating lost bone. While the model presented provides a promising avenue to explore, future work must be conducted to not only enhance nutrient transport and mineralization between the user defined macro-vasculature, but also to achieve implant integration with native tissue in an *in vivo* setting.

5.5 References

1. Keogh, M.B., F.J. O'Brien, and J.S. Daly, *Substrate stiffness and contractile behaviour modulate the functional maturation of osteoblasts on a collagen–GAG scaffold*. *Acta Biomaterialia*, 2010. **6**(11): p. 4305-4313.
2. Pandit, V., et al., *Evaluation of multifunctional polysaccharide hydrogels with varying stiffness for bone tissue engineering*. *Tissue Engineering Part A*, 2013. **19**(21-22): p. 2452-2463.
3. Murphy, W.L., et al., *Sustained release of vascular endothelial growth factor from mineralized poly (lactide-co-glycolide) scaffolds for tissue engineering*. *Biomaterials*, 2000. **21**(24): p. 2521-2527.
4. Lee, K.Y., et al., *Controlled growth factor release from synthetic extracellular matrices*. *Nature*, 2000. **408**(6815): p. 998.
5. Sheridan, M., et al., *Bioabsorbable polymer scaffolds for tissue engineering capable of sustained growth factor delivery*. *Journal of Controlled Release*, 2000. **64**(1-3): p. 91-102.

6. Peters, M.C., P.J. Polverini, and D.J. Mooney, *Engineering vascular networks in porous polymer matrices*. Journal of Biomedical Materials Research Part A, 2002. **60**(4): p. 668-678.
7. Borges, J., et al., *Engineered adipose tissue supplied by functional microvessels*. Tissue Engineering, 2003. **9**(6): p. 1263-1270.
8. Malda, J., T.J. Klein, and Z. Upton, *The roles of hypoxia in the in vitro engineering of tissues*. Tissue Engineering, 2007. **13**(9): p. 2153-2162.
9. Black, C.R., et al., *Bone tissue engineering*. Current Molecular Biology Reports, 2015. **1**(3): p. 132-140.
10. Wang, L., et al., *Osteogenesis and angiogenesis of tissue-engineered bone constructed by prevascularized β -tricalcium phosphate scaffold and mesenchymal stem cells*. Biomaterials, 2010. **31**(36): p. 9452-9461.
11. Yu, H., et al., *Promotion of osteogenesis in tissue-engineered bone by pre-seeding endothelial progenitor cells-derived endothelial cells*. Journal of Orthopaedic Research, 2008. **26**(8): p. 1147-1152.
12. Villars, F., et al., *Effect of human endothelial cells on human bone marrow stromal cell phenotype: role of VEGF?* Journal of Cellular Biochemistry, 2000. **79**(4): p. 672-685.
13. Santos, M.I. and R.L. Reis, *Vascularization in bone tissue engineering: physiology, current strategies, major hurdles and future challenges*. Macromolecular Bioscience, 2010. **10**(1): p. 12-27.
14. Villars, F., et al., *Effect of HUVEC on human osteoprogenitor cell differentiation needs heterotypic gap junction communication*. American Journal of Physiology-Cell Physiology, 2002. **282**(4): p. C775-C785.

15. Stegen, S., N. van Gastel, and G. Carmeliet, *Bringing new life to damaged bone: the importance of angiogenesis in bone repair and regeneration*. *Bone*, 2015. **70**: p. 19-27.
16. Ghanaati, S., et al., *Rapid vascularization of starch–poly (caprolactone) in vivo by outgrowth endothelial cells in co-culture with primary osteoblasts*. *Journal of Tissue Engineering and Regenerative Medicine*, 2011. **5**(6).
17. Guillotin, B., et al., *Interaction between human umbilical vein endothelial cells and human osteoprogenitors triggers pleiotropic effect that may support osteoblastic function*. *Bone*, 2008. **42**(6): p. 1080-1091.
18. Unger, R.E., et al., *Tissue-like self-assembly in cocultures of endothelial cells and osteoblasts and the formation of microcapillary-like structures on three-dimensional porous biomaterials*. *Biomaterials*, 2007. **28**(27): p. 3965-3976.
19. Ma, J., et al., *Coculture of osteoblasts and endothelial cells: optimization of culture medium and cell ratio*. *Tissue Engineering Part C: Methods*, 2010. **17**(3): p. 349-357.
20. Yang, L., et al., *An in vitro vascular chip using 3D printing-enabled hydrogel casting*. *Biofabrication*, 2016. **8**(3): p. 035015.
21. Tocchio, A., et al., *Versatile fabrication of vascularizable scaffolds for large tissue engineering in bioreactor*. *Biomaterials*, 2015. **45**: p. 124-131.
22. Shanjani, Y., et al., *Endothelial pattern formation in hybrid constructs of additive manufactured porous rigid scaffolds and cell-laden hydrogels for orthopedic applications*. *Journal of the Mechanical Behavior of Biomedical Materials*, 2017. **65**: p. 356-372.
23. Baranski, J.D., et al., *Geometric control of vascular networks to enhance engineered tissue integration and function*. *Proceedings of the National Academy of Sciences*, 2013. **110**(19): p. 7586-7591.

24. Lee, V.K., et al., *Generation of multi-scale vascular network system within 3D hydrogel using 3D bio-printing technology*. Cellular and Molecular Bioengineering, 2014. **7**(3): p. 460-472.
25. Laschke, M.W., et al., *Angiogenesis in tissue engineering: breathing life into constructed tissue substitutes*. Tissue Engineering, 2006. **12**(8): p. 2093-2104.
26. Lovett, M., et al., *Vascularization strategies for tissue engineering*. Tissue Engineering Part B: Reviews, 2009. **15**(3): p. 353-370.
27. Zhang, W., et al., *Vascularization of hollow channel-modified porous silk scaffolds with endothelial cells for tissue regeneration*. Biomaterials, 2015. **56**: p. 68-77.
28. Sooppan, R., et al., *In vivo anastomosis and perfusion of a three-dimensionally-printed construct containing microchannel networks*. Tissue Engineering Part C: Methods, 2015. **22**(1): p. 1-7.
29. Mercado-Pagán, Á.E., et al., *Vascularization in bone tissue engineering constructs*. Annals of Biomedical Engineering, 2015. **43**(3): p. 718-729.
30. Cheng, G., et al., *Engineered blood vessel networks connect to host vasculature via wrapping-and-tapping anastomosis*. Blood, 2011. **118**(17): p. 4740-4749.

STEPHEN WILLIAM SAWYER

WORK ADDRESS

HOME ADDRESS

U.S. Food and Drug Administration
Center for Biologics Evaluation and Research
10903 New Hampshire Ave
Silver Spring, MD 20993
stephen.sawyer@fda.hhs.gov

8621 Georgia Ave
Silver Spring, MD 20910
757.503.1749 (phone)

EDUCATION

Syracuse University

Ph.D.

Dec 2018

Bioengineering

GPA – 3.79

Syracuse Biomaterials Institute, Syracuse, NY

Thesis: Cell-Laden Biomimetic Scaffolds for Bone Tissue Regeneration (Advisor Dr. Pranav Soman)

University of South Carolina

M.B.A.

Aug 2009

Master of Business Administration

GPA – 3.6

Moore School of Business, Columbia, SC

Virginia Military Institute**B.S.****May 2005**

Bachelor of Science in Physics with Minor in Mathematics

GPA – 3.8

Virginia Military Institute, Lexington, VA

PROFESSIONAL EXPERIENCE

Center for Biologics Evaluation and Research**U.S. Food and Drug Administration**

ORISE Postdoctoral Fellow (2018 – Present)

Silver Spring, MD

Department of Biomedical and Chemical Engineering**Syracuse University**

Graduate Research Assistant (2013 – 2018)

Syracuse, NY

Department of Biology**Hampton University**

Graduate Student (2011 – 2013)

Hampton, VA

ISE Division**M.C. Dean Incorporated**

Project Manager (2009 – 2011)

Stuttgart, Germany

Naval Weapons Station**United States Navy**

Assistant Administrative Officer (2008 – 2009)

Charleston, SC

Naval Nuclear Power Training Command**United States Navy**

Naval Nuclear Power Instructor (2005 – 2008)

Goose Creek, SC

SELECTED PUBLICATIONS

1. Sawyer SW, Shridhar SV, Zhang K, Albrecht LD, Filip AB, Horton JA, Soman P. (2018) Perfusion directed 3D mineral formation within cell-laden hydrogels. *Biofabrication* 10(3):035013.
2. Suvarnapathaki S, Ramos R, Sawyer SW, McLoughlin ST, Ramos AS, Venn SA, Soman P. (2018) Generation of cell-laden hydrogel microspheres using 3D printing-enabled microfluidics. *Journal of Materials Research* 33(14):2012-2018.
3. Sawyer SW, Dong P, Venn SA, Ramos AS, Quinn D, Horton JA, Soman P. (2017) Conductive gelatin methacrylate-poly (aniline) hydrogel for cell encapsulation. *Biomedical Physics & Engineering Express* 4(1):015005.
4. Sawyer SW, Oest ME, Margulies BS, Soman P. (2016) Behavior of encapsulated saos-2 cells within gelatin methacrylate hydrogels. *Journal of Tissue Science & Engineering* 7(2):173.
5. Albrecht LD, Sawyer SW, Soman P. (2016) Developing 3D scaffolds in the field of tissue engineering to treat complex bone defects. *3D Printing and Additive Manufacturing* 3(2):106-12.

6. Wu Y, Chen YX, Yan J, Quinn D, Dong P, Sawyer SW, Soman P. (2016) Fabrication of conductive gelatin methacrylate-polyaniline hydrogels. *Acta Biomaterialia* 33:122-30.

PEER-REVIEWED ABSTRACTS AND CONFERENCE PROCEEDINGS

1. Sawyer SW, Shridhar SV, Zhang K, Albrecht LD, Horton JA, Soman P. Perfusion driven 3D bone mineral formation. *SFB 2018 Annual Meeting*. April 2018. Atlanta, GA. **Oral Presentation.**
2. Sawyer SW, Shridhar SV, Zhang K, Albrecht LD, Filip AB, Horton JA, Soman P. Bone tissue engineering using 3D printing. *ORS 2018 Annual Meeting*. March 2018. New Orleans, LA.
3. Zhang K, Sawyer SW*, Albrecht LD, Ramos AS, Filip AB, Horton JA, Soman P. Perfusion directed 3D bone mineral formation. *Biomedical Engineering Society (BMES) Annual Meeting*. October 2017. Phoenix, AZ. **Oral Presentation. *1st Author.**
4. Filip AB, Albrecht LD, Sawyer SW, Soman P. Multi-material hydrogel printing using an open-source 3D printer. *Biomedical Engineering Society (BMES) Annual Meeting*. October 2017. Phoenix, AZ.
5. McLoughlin S, Suvarnapathaki S, Ramos R, Sawyer SW, Soman P. Cell-laden hydrogel microspheres using 3D printed microfluidics. *Biomedical Engineering Society (BMES) Annual Meeting*. October 2017. Phoenix, AZ.

6. Sawyer SW, Zhang K, Albrecht LD, Ramos AS, Filip AB, Horton JA, Soman P. Perfusion directed 3D bone mineral formation. *SFB 2017 Annual Meeting*. April 2017. Minneapolis, MN.
7. Sawyer SW, Dong P, Venn SA, Ramos AS, Quinn DE, Horton JA, Soman P. Conductive gelatin methacrylate-polyaniline hydrogels for bone tissue engineering. *ORS 2017 Annual Meeting*. March 2017. San Diego, CA.
8. Sawyer SW, Albrecht LD, Oest ME, Margulies BS, Soman P. Cell-laden gelatin methacrylate hydrogels for bone tissue engineering. *Active and Smart Matter: a New frontier in Science and Engineering*. June 2016. Syracuse, NY.
9. Soman P, Sawyer SW, Albrecht LD, Oest ME, Margulies BS. Engineering scaffolds for bone tissue engineering using cell-laden gelatin methacrylate hydrogels. *10th World Biomaterials Congress*. May 2016. Montréal, Canada.

LOCAL PRESENTATIONS

1. Sawyer SW, Shridhar SV, Zhang K, Albrecht LD, Filip AB, Horton JA, Soman P. Perfusion driven 3D bone mineral formation. 2018 Stevenson Biomaterials Lecture and Research Poster Session. March 2018. Syracuse, NY.
2. Sawyer SW, Shridhar SV, Zhang K, Albrecht LD, Filip AB, Horton JA, Soman P. Perfusion directed 3D bone mineral formation. *BMCE Seminar Series*. December 2017. Syracuse NY. *Invited Talk*.
3. Sawyer SW, Zhang K, Albrecht LD, Ramos AS, Filip AB, Horton JA, Soman P. Perfusion directed 3D bone mineral formation. *ORS Upstate New York and Northeast Regional Symposium*. July 2017. Rochester, NY.
4. Zhang K, Sawyer SW, Albrecht LD, Ramos AS, Filip AB, Horton JA, Soman P. Perfusion directed 3D bone mineral formation. *2017 Stevenson Biomaterials Lecture and Research Poster Session*. March 2017. Syracuse, NY.
5. Venn SA, Sawyer SW, Dong P, Ramos AR, Quinn D, Horton J, Soman P. Encapsulation of saos-2 cells in conductive gelatin methacrylate hydrogels. *Syracuse Summer 2016 Undergraduate Research Poster Session*. August 2016. Syracuse, NY.
6. Morton MK, Albrecht LD, Sawyer SW, Soman P. Fabrication of hydrogel scaffolds with integrated microfluidic channels. *Syracuse Summer 2016 Undergraduate Research Poster Session*. August 2016. Syracuse, NY.

7. Sawyer SW, Albrecht LD, Ramos AR, Oest ME, Margulies BS, Soman P. Engineering scaffolds for bone tissue engineering using cell-laden gelatin methacrylate hydrogels. *2016 Stevenson Biomaterials Lecture and Research Poster Session*. March 2016. Syracuse, NY.
8. Sawyer SW, Aslan C, Chen YX, Margulies BS, Ogden KM, Henderson JH, Soman P. Bone regeneration using structurally reinforced stem cell-laden hydrogels. *2014 IGERT Retreat*. April 2014. Syracuse, NY.

TEACHING ACTIVITIES

Naval Nuclear Power Instructor

(August 2005 – August 2008)

Instructed and provided mentorship to over 400 junior enlisted sailors, instructed Mathematics and Reactor Principles, and managed a division of officer and enlisted personnel.

PROFESSIONAL ACTIVITY

Membership

Society for Biomaterials (2016 – present)

HONORS AND AWARDS

ORISE Postdoctoral Fellowship	2018
SBI Distinguished Ph.D. Student Research Award	2018
Integrative Graduate Education and Research Traineeship Program Fellowship	2017 – 2018

Syracuse Biomaterials Institute Graduate Fellowship	2016
Integrative Graduate Education and Research Traineeship Program Fellowship	2013 – 2015
Navy and Marine Corps Achievement Medal	2007
Navy Master Training Specialist	2007
VMI Institute Scholarship	2001 – 2005